DEVELOPMENT AND APPLICATION OF FLEXIBLE DUAL-SIDED MICROELECTRODE ARRAYS(MEAS) FOR ADVANCED BIOELECTRONIC SENSING AND NEURAL INTERFACING

By

Xiang Liu

A DISSERTATION

Submitted to
Michigan State University
in partial fulfillment of the requirements
for the degree of

Neuroscience – Doctor of Philosophy

2025

ABSTRACT

A noteworthy in the dynamic field of neuroscience is the study of extracellular neural responses in live insect neurons, triggered by volatile organic compounds (VOCs). Biological olfaction has shown remarkable sensitivity in detecting low concentrations of VOCs, ranging from parts per billion (ppb) to parts per trillion (ppt) range, and minute changes in the compositions of gas mixtures. This scenario has inspired a novel concept for early lung cancer diagnosis, wherein odors exhaled by humans are channeled to insect sensory organs, like locust antennae. To effectively implement this scheme, efficient neural activity recording tools and robust analysis methods are essential. Microelectrode arrays (MEAs) present a more promising alternative. Yet, in the specific context of insect brain neurology, there is a growing need for flexible, multi-channel, or even high-density MEAs(HDMEAs). Flexible MEAs, particularly those with high-density configurations, offer significant advantages over traditional rigid systems, including reduced tissue damage, better long-term stability, and higher resolution in both electrophysiological recording and biosensing applications.

This dissertation presents the development and validation of advanced biosensing platforms for neurophysiological recording, emphasizing the integration of high density flexible dual-sided MEAs with locust olfactory systems to detect lung cancer biomarkers from VOCs. Through a multidisciplinary approach combining materials science, electronic engineering, and neurobiology, we explore the capabilities of HDMEAs to enhance the spatial and temporal resolution of neural recordings in both experimental and clinical settings.

Chapter 1 begins with a foundational understanding of physiological signals and the techniques used to record them, followed by an in-depth discussion of MEAs, their principles, and their historical development. Special attention is given to the importance of flexibility and

high channel density, which have transformed the design and performance of MEAs. Through an analysis of current flexible high-density MEAs, their fabrication, and the challenges they face, the chapter highlights the innovations that have propelled these tools into cutting-edge bioelectronic applications. Finally, strategies and future directions for next-generation flexible HDMEAs are outlined, setting the stage for their continued role in advanced sensing and neural interfacing technologies. Chapter 2 explores the development of dual-sided MEAs designed to enhance the recording capabilities and mechanical reliability necessary for *in vivo* insects' applications. The innovative folding-annealing technique used in this research allows for a substantial increase in the density of recording sites without expanding the MEAs' physical footprint. Chapter 3 expands on the application of these technologies, detailing the development of a flexible, dual-sided microelectrode array optimized for capturing the complex neural dynamics of the locust olfactory system. This novel biosensing platform leverages the locust's acute sensory detection capabilities to identify cancer-related VOCs, offering a promising alternative to traditional diagnostic methods like gas chromatography-mass spectrometry (GC-MS). Chapter 4 provides a comprehensive outlook and delineates ongoing work and conclusions from this research.

Overall, this dissertation demonstrates the potential of merging biological systems with electronic sensing technologies to create sensitive and non-invasive diagnostic tools for human lung cancer. This work not only contributes to the field of biomedical engineering but also opens avenues for future research into bioelectronic interfaces and their applications in medical diagnostics.

To Yiyi and my entire family, for their unwavering support and faith in my dreams. To all the curious minds who dare to envision a better future through science.

ACKNOWLEDGEMENTS

First and foremost, I extend my deepest gratitude to my supervisor, Prof. Wen Li. Her invaluable guidance, unwavering support, and insightful feedback have been vital throughout my PhD journey. Her foresight, patience, and critical thinking not only enabled me to successfully carry out my research but also greatly contributed to my growth as a researcher. Her rigorous professional standards in science will remain a lifelong source of inspiration.

I am profoundly grateful to my committee members: Prof. Erin Purcell, Prof. Debajit Saha, and Prof. Zhen Qiu. Their constructive suggestions and unwavering support played a crucial role in shaping my research. I am also thankful for their valuable insights and collaboration throughout my studies. My gratitude also extends to their graduate students and postdocs, Simon Sanchez, Yifan Liu, Bhavna Gupta, and Dr. Bo Li, for their contributions.

My sincere thanks go to our collaborators: Prof. Arthur Weber, Prof. Yaoyao Jia, Prof. Christopher Contag, Prof. Qihua Fan, Prof. Chunqi Qian, and Prof. Galit Pelled, for their cooperation and technical expertise. I am equally grateful to Dr. Roksana Riddle, Dr. Linran Zhao and Dr. Young Kim for their collaborative efforts on various projects.

I would like to express my appreciation to my colleagues at the Microtechnology Lab: Dr. Yan Gong, Dr. Weiyang Yang, Zebin Jiang, Trevor Stevens, Banna Hasan, Andrew Creech, and Mohammad Kafi Kangi. I am also thankful for the assistance and support provided by Dr. Baokang Bi at the Keck Cleanroom, Mr. Brian Wright at the ECE shop, and Mr. Karl Dersch at the ERC Cleanroom.

Additionally, I extend my heartfelt thanks to the Neuroscience Program community, which has been a warm and supportive family to me. Director A.J. Robinson, Ms. Eleri Thomas,

and all the faculty and students offered invaluable encouragement and assistance throughout my journey.

Finally, I wish to express my deepest appreciation to my family for their unwavering and selfless support. Their encouragement has been a constant source of strength, and this achievement would not have been possible without the collective support of everyone mentioned, as well as many others who have contributed in countless ways.

TABLE OF CONTENTS

LIST OF ABBREVIATIONS

MEA	Microelectrode Array
HDMEA	High-Density Microelectrode Array
AP	Action Potential
ECG	Electrocardiogram
EEG	Electroencephalogram
ECoG	Electrocorticography
LFP	Local Field Potential
BMI	Brain-Machine Interface
FP	Field Potential
EPSP	Excitatory Postsynaptic Potential
RC	Resistive-Capacitive (Circuit Model)
CMOS	Complementary Metal-Oxide-Semiconductor
PEDOT	Poly(3,4-ethylenedioxythiophene)
SNR	Signal-to-Noise Ratio
PCB	Printed Circuit Board
ACF	Anisotropic Conductive Film
FFC	Flat Flexible Cable
ZIF	Zero Insertion Force
CNT	Carbon Nanotube
PDMS	Polydimethylsiloxane
FET	Field-Effect Transistor
MOSFET	Metal-Oxide-Semiconductor Field-Effect Transistor

ASIC	Application-Specific Integrated Circuit
3D-MEA	Three-Dimensional Microelectrode Array
BDNF	Brain-Derived Neurotrophic Factor
NMDAR	N-Methyl-D-Aspartate Receptor
VLSI	Very Large Scale Integration
MEMS	Micro-Electro-Mechanical Systems
DBS	Deep Brain Stimulation
LED	Light Emitting Diode
fMRI	Functional Magnetic Resonance Imaging
PET	Positron Emission Tomography
IrOx	Iridium Oxide
SFAP	Single Fiber Action Potential
MUAP	Motor Unit Action Potential
MU	Motor Unit
CV	Cyclic Voltammetry
SEM	Scanning Electron Microscopy
EIS	Electrochemical Impedance Spectroscopy
APS-CMOS	Active Pixel Sensor Complementary Metal-Oxide Semiconductor
DI water	Deionized Water
Ag/AgCl	Silver/Silver Chloride
RE	Reference Electrode
CE	Counter Electrode
WE	Working Electrode

RIE	Reactive Ion Etching
RMS	Root Mean Square
VOCs	Volatile Organic Compounds
Au etchant	Gold etchant
SF6	Sulfur Hexafluoride
EDOT	3,4-Ethylenedioxythiophene
PSS	Poly(styrene sulfonate)
LCDT	Low Dose Computed Tomography
GC-MS	Gas Chromatography-Mass Spectrometry
SIFT-MS	Selected Ion Flow Tube Mass Spectrometry
PTR-MS	Proton Transfer Reaction Mass Spectrometry
GC-IMS	Gas Chromatography-Ion Mobility Spectrometry
ORNs	Olfactory Receptor Neurons
AL	Antennal Lobe
PNs	Projection Neurons
LNs	Local Neurons
sccm	Standard Cubic Centimeters per Minute
PBS	Phosphate Buffered Saline
PCA	Principal Component Analysis
LDA	Linear Discriminant Analysis
LOTO	Leave-One-Trial-Out

CHAPTER 1: FLEXIBLE MICROELECTRODE ARRAYS IN ELECTROPHYSIOLOGY AND SENSING

1. INTRODUCTION

MEAs have revolutionized the field of electrophysiology by enabling the simultaneous recording and stimulation of electrical activity from multiple neurons or other excitable cells. These devices have found widespread application in neurophysiology, brain-machine interfaces (BMIs), and biosensing technologies, providing researchers and clinicians with invaluable tools to monitor and manipulate complex biological systems. As the demand for more sophisticated and biocompatible neural interfaces has grown, the development of flexible MEAs has emerged as a critical innovation. Flexible MEAs, particularly those with high-density configurations, offer significant advantages over traditional rigid systems, including reduced tissue damage, better long-term stability, and higher resolution in both electrophysiological recording and biosensing applications[1, 2]. Figure 1.1 illustrates the ideal properties desired for MEAs, such as high recording quality, biosafety, and long-term stability, alongside the challenges—mechanical, electrical, chemical, and biological—that currently hinder their realization. To overcome these challenges, strategic approaches, including material selection, MEA design optimization, advanced fabrication techniques, and engineering innovations, are essential for developing next-generation flexible high-density MEAs capable of meeting these ideal criteria.

In this chapter, we will explore the advancements and applications of flexible MEAs in the fields of electrophysiology and sensing. As essential tools for recording electrical activity from various physiological sources such as the heart, neurons, and neuromuscular systems, MEAs have evolved significantly over time. This chapter begins with a foundational understanding of physiological signals and the techniques used to record them, followed by an in-depth discussion

of MEAs, their principles, and their historical development. Special attention is given to the importance of flexibility and high channel density, which have transformed the design and performance of MEAs. Through an analysis of current flexible high-density MEAs (HDMEAs), their fabrication, and the challenges they face, the chapter highlights the innovations that have propelled these tools into cutting-edge bioelectronic applications. Finally, strategies and future directions for next-generation flexible HDMEAs are outlined, setting the stage for their continued role in advanced sensing and neural interfacing technologies.

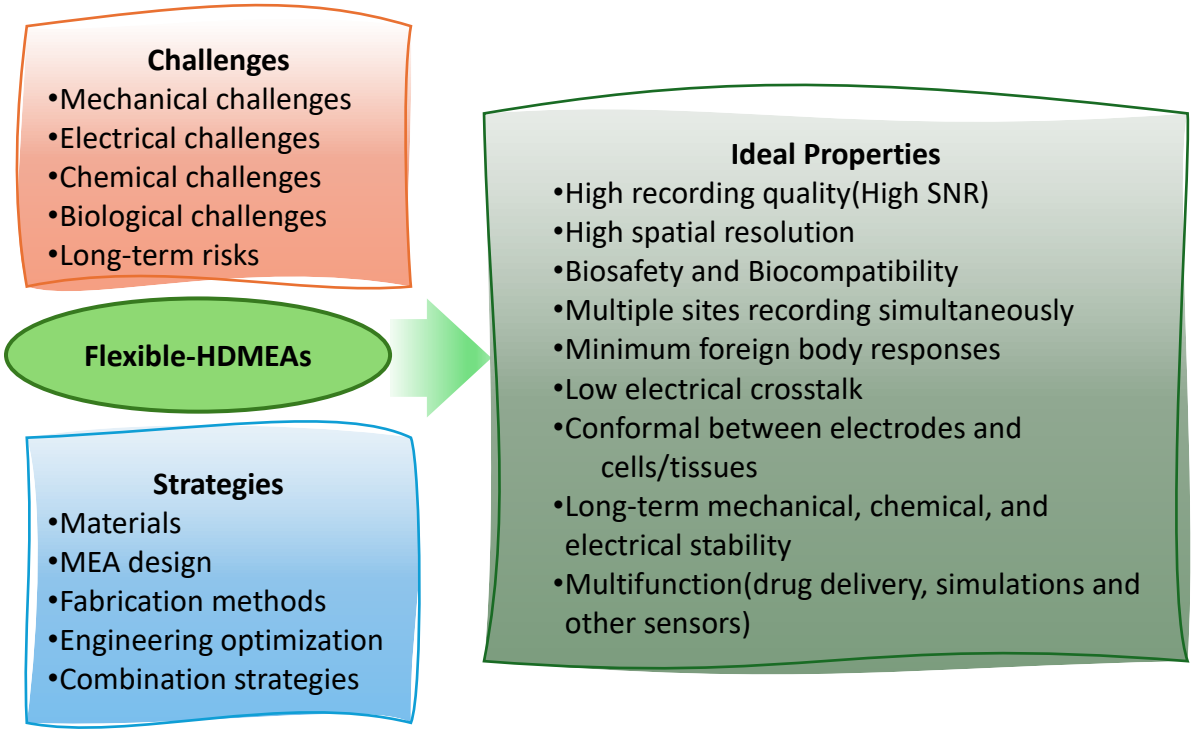

Figure 1.1. Ideal properties, challenges, and development strategies associated with HDMEAs.

2. PHYSIOLOGICAL SIGNALS AND SENSING TECHNIQUES

The underlying mechanism of electrophysiological signals is related to variations of ionic concentrations between the inner side and outer side of the membrane that is modulated by cell biomolecules[3]. The electrical activities of the excitable cells include resting potential, action potential, and subthreshold postsynaptic potential. The cellular membrane, a phospholipid bilayer

embedded with hundreds of different types of integral and peripheral mobile proteins, has a high electrical resistivity, defining the cell and separating the cytoplasm from the outside space. The selective permeation of the membrane to ions results in an asymmetry of ion concentrations and charges between the two sides of the membrane, creating a difference in electrical potential called the resting potential. This could be explained by the Hodgkin and Huxley model[4].

An action potential(AP) occurs when specific electrical stimulation (natural or external sources) triggers the opening of specific channels, causing the membrane potential of a particular cell rapidly rises(depolarization) and fall (repolarization)[4]. Action potential signals can be transmitted to cells nearby within milliseconds, forming communications between cells and enabling tissue and organ function, such as cognitive brain function, muscle contraction, heartbeats, and responses in sensory organs. The subthreshold postsynaptic potential is a change in the membrane potential at the postsynaptic end of a chemical synapse caused by the release of neurotransmitters from vesicles by presynaptic neurons into the synaptic cleft[5].

Electrophysiology nowadays deals with different techniques of analyzing electrical signals (current and potential changes) generated at cell membranes or with techniques where electrical stimuli are guided to the membrane to investigate their influence on membrane transport and cell function[6]. Through comprehensive analysis of these electrophysiological signals recorded by electrodes, important information related to the cells, tissues, and organs could be revealed, enabling an accurate method of monitoring the activities of the cells under physiological and pathological conditions, which further benefits scientific research and clinical practice.

The intracellular recording techniques, such as voltage or current clamp, and patch-clamp recording, enable the measurements of single cell potential or current change precisely in given conditions, facilitating the understanding of cellular molecular and genetic mechanisms

underlying the electrical signals changes. However, these intracellular recording techniques have some disadvantages, such as damage to the cells being recorded, inability to record multiple cells at the same time, which limits them in the use of recording the cells recording multiple cells with higher temporal and spatial levels and recordings in a living body. Extracellular recording, by contrast, collects the electrophysiological extracellular signals from a single cell or multiple cells. Notably, MEAs, especially HDMEAs, have higher spatial resolution and can provide more accurate information[1, 2, 7].

3. INTRODUCTION TO MICROELECTRODE ARRAYS

MEAs have become foundational tools in the development of brain-machine interfaces (BMIs) and numerous other electrophysiological applications. These arrays have proven to be powerful components in systems, such as BMIS, for understanding the brain [8], diagnosing neurological disorders[9], restoring lost function in individuals with [10, 11] and enhancing brain functions[12]. MEA-based systems systems are widely utilized in neurorehabilitation [13-15], prosthetics control [16], treatment of severe neurological disorders [17], and adaptive deep brain stimulation [18-20], among other fields.

MEAs are essential in electrophysiology, allowing for the simultaneous recording and stimulation of electrical activity in neurons, muscles, and other excitable tissues. Composed of electrodes embedded on a substrate, MEAs interface directly with biological systems, capturing the electrical signals generated by excitable cells. A MEA consists of a grid of tightly spaced microelectrodes that can be used to detect electrophysiological signals from neurons or to deliver electrical pulses to stimulate neural activity [21].

MEAs with high spatial and temporal resolution of MEAs are promising in both basic research and clinical applications, including BMIs, cardiac monitoring, and biosensing.

Conventional MEAs with single channel or multiple channels separated with far distance(>200 μm) have historically played a vital role in the development and applications of BMIs [22]. However, the high-density microelectrode arrays (HDMEAs), with significantly enhanced density and channel count arranged on a limited area [23], offer several advantages compared to conventional MEAs. In closed-loop BMIs, typically, neural signals (e.g., electrical activity of neurons) are initially recorded using a neural interface device, such as a microelectrode array (MEA). These signals are then decoded and processed to derive user intentions, which are translated into commands for controlling an external device. Subsequently, feedback from the device, often in the form of electrical stimulation, is delivered back to the brain, closing the loop [24]. This contrasts with open-loop systems, which might only read brain signals or stimulate the brain without any real-time feedback [25].

This section will now explore the general principles of MEAs, their historical development, the necessities and the advancements towards flexible, high-channel-density MEAs.

3.1 General Principles of MEAs

A typical MEA system contains an MEA, filter, amplifier, and hardware and software system for data collection, sampling, and analysis. The electrophysiological signals go through the following processes within the MEA system during recording:

(1) generated by excitable cells and spread around; (2) conducted to the surrounding cells and extracellular space, and then transmitted to the exposed electrodes through the cell/tissue-microelectrode array interface. (3) transmitted from exposed electrodes, through embedded electrode circuits to the contact pads, which are connected to external devices. (4) go external devices, such as filters, and amplifiers, and then transfer to data information. When the electrophysiological signal spreads into the extracellular space or electrolyte solution where the

electrode is located, the interface double electric layer will be formed between the cell and the electrode, resulting in the change of ion concentration and then the change of charge distribution. This causes polarization on the electrode surface, leading to voltage changes, which could be detected and recorded by the external parts connected to the electrodes.

A passive MEA simply provides the connection from the conductive material to the equipment for capturing, processing, and amplifying the signal, while the active electrodes have an active circuit element, such as a transistor, that amplifies signals before additional noise is added to the system. A typical passive MEA consists of three parts (microelectrodes, conduct lines, and the contact pads), and usually has three layers substrates on the bottom, conductive microelectrode array in the middle, and insulation layer over the top. A microelectrode and a contact pad are located at each end of the line so that each electrode is individually addressable through the contact pad. Microelectrodes are laid out with regular spacing to form an array[26]. The substrate provides mechanical support to the microelectrode interface and is electrically insulative; conduct lines provide electrical connections between the microelectrode tips and the larger contact pads; insulators provide a non-conductive barrier between the conductors and cells, with openings for microelectrodes and contact pads[27].

The electrophysiological signals generated by excitable cells can be transmitted to cells nearby within milliseconds of time to the extracellular conductor space, resulting in changing electric fields around the area. These weak electrical signals can be collected by electrodes from cells, tissues, organs, and the surface of the body. Through signal amplification, filtering, signal processing, and further analysis, characteristic information could be obtained from the original recording data. Thereby, the electrical signals collected under different states of the cells, tissues, or organs will show other characteristics, such as differentiation of waveform, frequency, peak,

etc., which are used for scientific research, clinical monitoring, diagnosis, and treatment Propagating APs or synaptic potentials produce complex extracellular current flow between activated compartments and other parts of the neuron, part of which flow between the non-junctional and the junctional membranes. The cleft between the neuron and the electrode generates a resistance that is referred to as the seal resistance (Rseal). The voltage formed over Rseal directly modulates the gate voltage of a field-effect transistor (FET), or the charge dispersal across a passive metal electrode [28].

3.2 Historical Development of MEAs

Given the limitations of existing techniques such as patch clamp, scientists hope to have simple and convenient ways to record neuronal activities from a large number of spots over a long period, so that they obtain information to understand the development and plasticity of neurons and other cells.

In 1970, Wise and colleagues[29] at the University of Michigan multichannel developed shank-based probes using integrated-circuit fabrication techniques, commonly identified as Michigan-style probes. Thomas, Gross, and Pine et al. recorded electrophysiological signals via MEAs from isolated chicken embryonic cardiomyocytes, isolated snail ganglia, and rat upper cervical ganglia, respectively. In 1972, Thomas et al.[30] used microelectrode array technology to detect the extracellular signal of isolated chicken embryonic cardiomyocytes, thus introducing microelectrode array into electrophysiological research for the first time. In 1977, Gross et al.[31] developed a 36-channel MEA to measure extracellular action potentials in snail cranial ganglia. In 1980, Pine et al. [32]completed the recording of dissociated neurons of the rat superior cervical ganglion by using 32-channel MEAs.

During the 80s, MEAs gradually became an essential method in the field of neuroscience because of the extension of use in cultured cells and tissue slices (Jobling et al., 1981; Wheeler and Novak, 1986) and the emergence of customized multielectrode models[33].

The advancement of semiconductor etching technology promoted the development of MEAs from the 90s. In 1991, scientists from the University of Utah developed 100 conductive three-dimensional microneedle arrays on a single silicon wafer for signals recording *in vivo* [34]. This type of microneedle array is referred to as the Utah array. By assembling the multiple Michigan MEA probes, three-dimensional signal reading can be achieved. In the years that followed, many scientists worked to improve or customize the MEAs for higher recording quality and more complex application scenarios. For example, 3-dimensional platinum MEAs are designed to enhance electrode-to-cell contact and capture signals in a 3-dimensional environment[35].

Since 2000, research and development of these passive electrode systems have focused on optimizing electrode and recording performance, including using new materials to improve biocompatibility and recording quality[36]. Compared to passive MEAs, the active electrodes have a pre-amplification module that amplifies the signal before additional noise is added to the system. The rise of microelectronics, especially the introduction of the complementary metal–oxide–semiconductor (CMOS) commonly used in digital cameras, has greatly facilitated the development of active, high-resolution, high-density MEAs. The first *in vitro* study of an MEA using high-density APS-CMOS simultaneously provided records from 4096 electrodes[37].

In recent years, MEAs have been developing toward a higher microelectrode density. New materials and methods have considerably significantly changed the quality of the electrical recording in small-size electrodes, making it possible to place more electrodes in a limited space. Innovative HDMEAs have also greatly expanded the application scenarios, such as 3D-MEA

designed specifically for organoids, MEAs designed to target different deep brain sites, spherical stretchable flexible MEA designed for retina, and customized MEAs for specific animal models, such as zebrafish hearts, insect muscles, etc.

3.3. TOWARDS FLEXIBLE AND HIGH CHANNEL DENSITY MEAs

3.3.1. Importance of Flexibility and Density in MEAs

Conventional MEAs with single channel or multiple channels separated with far distance(>200 μm) have historically played a vital role in the development and applications of BMIs [22]. However, the high-density microelectrode arrays (HDMEAs), with significantly enhanced density and channel count arranged on a limited area [23], offer several advantages compared to conventional MEAs. First, HDMEAs can detect and stimulate neural activity with higher spatial resolution and greater precision, enabling more detailed mapping of neural networks and a better understanding of complex brain functions. Second, the high density of electrodes provides a more comprehensive dataset. This richness of data is essential for advanced neural decoding algorithms, which can translate neural activity into more accurate and nuanced commands for BMIs. Third, in lower-density arrays, signals from multiple neurons are often averaged over larger electrode areas, potentially losing critical information. HDMEAs can reduce this spatial averaging, capturing more discrete signals from individual or small groups of neurons. Finally, with more electrodes interacting with neurons, HDMEAs can potentially facilitate more complex and nuanced interactions between the BMI and the brain, leading to more sophisticated applications and therapies.

HDMEAs can be categorized into rigid and flexible types, depending on the material of the substrate used for fabricating the microelectrodes[38]. At present, the most advanced HDMEAs are rigid leveraging the state-of-the-art silicon manufacturing technology. For example,

Neuropixels 2.0, a miniaturized high-density silicone-based probe, has total of 1280 channels on one shank with a profile of 10 mm x 70 μm x 24 μm [39]. However, rigid HDMEAs often encounter limitations [11, 40, 41], including inflammatory response, tissue damage, limited long-term stability, and biocompatibility issues.

Flexible MEAs, often fabricated from soft materials like polyimide or parylene, can adeptly mold to the neural tissue and provide less mismatch between interfaces and brain tissue, reducing the risk of tissue damage and ensuring a more stable, intimate interaction with neurons [42]. Furthermore, the adaptability of flexible MEAs allows them to accommodate physiological changes and movements within the brain, maintaining consistent interfacing and thereby supporting the longevity and robustness of the BMI system [43, 44]. Consequently, flexibility in MEAs is not merely a beneficial attribute but a quintessential one, ensuring the viability, reliability, and efficacy of BMIs in both research and clinical applications. Further merging the benefits of both, flexible HDMEAs bring the adaptability of flexible substrates to high-resolution electrode arrays, proving invaluable for discerning intricate neuronal dynamics, especially in dynamic or soft tissue environments where precision and conformability are paramount [45]. Flexible HDMEAs integrated with different stimulation modules, such as electrical[46], chemical[47], optical [48]), stimulation techniques.

Apart from flexibility and high density, the ideal profile of flexible HDMEAs for BMIs comprises several crucial attributes. These include biocompatibility [49], high-quality performance [26], and long-term stability [50, 51], etc. However, the development of flexible HDMEAs with these ideal properties entails confronting both the general challenges inherent to HDMEAs and specific challenges unique to their flexible design, encompassing mechanical [52], electrical [53, 54], biological [51], chemical [49], and interconnection issues [55]. In response,

researchers employ strategies spanning material exploration [56], flexible HDMEA design innovation[57], advanced fabrication strategies[19, 58, 59], engineering optimization[46, 60, 61], and holistic combination strategies [62, 63], aiming to enhance performance and minimize risks in flexible neural interfacing devices.

3.3.2. Definition of High Density

For a long time, we lacked a clear definition of HDMEAs. Among the published studies, MEAs that labeled high density have electrode densities ranging from less than one channel per square millimeter to thousands of channels per square millimeter. The variability in HDMEA definitions can be attributed to application-specific density requirements—high for brain neural spaces under 100 μm and lower for muscular targets over several thousand square microns[64, 65]—and the diversity in materials and technologies, which results in differing channel densities, ranging from a few to thousands of channels per square millimeter. In a recent paper, the high density was defined as the spacing among electrode sites being no more than 100 μm[66].

3.3.3 Design and Fabrication Principles of Flexible HDMEAs

The fabrication of flexible HDMEAs requires a comprehensive strategy that seamlessly integrates device geometries, material selection, fabrication techniques and approaches, surface modification and packaging methods, etc. Key considerations in fabrication of flexible HDMEAs are discussed below.

(1) Device geometries of a HDMEA encompass the spatial and physical configurations, including the arrangement, shape, size, and spacing of the electrodes, along with the overall structure of the device. This involves the meticulous layout of electrodes, which can vary in shape and size, and are strategically spaced to capture localized neural activity effectively. The shape and spatial configuration of HDMEAs are crucial for neural interfacing, with designs ranging

from flat, planar structures[67] to complex, curved[68], or three-dimensional (3D) forms[57, 69, 70] tailored to specific anatomical contexts, such as the cortical surface or deep brain regions. The overall shape impacts the HDMEA's ability to establish a stable interface with neural tissues, its mechanical stability, and its long-term biocompatibility, while the arrangement of electrodes—potentially organized in grids[71], linear arrays[72, 73], fiber shape[74] or intricate patterns[61, 75] and their individual shapes and sizes are meticulously crafted to enhance signal acquisition and stimulation capabilities.

(2) The selection of electrode materials, encompassing not only the substrate but also the conductive elements, insulating materials, and materials utilized in other components, holds critical importance in the development of flexible HDMEAs. For substrates in neural interfaces, the most commonly used materials encompass polymers, such as polyimide [76, 77], polydimethylsiloxane (PDMS) [78, 79], parylene C [80, 81], as well as other materials such as silk [82], medical adhesive tape [83], hydrogels [84], predominantly chosen for their biocompatibility, flexibility, and electrical insulation, ensuring safe and stable interfacing with neural tissues. An ideal electrode material needs to meet at least the following requirements: (1) compatible with cell/tissue without causing any changes in physiology and viability, (2) have good conductivity and low impedance to ensure a high signal-to-noise ratio (SNR), (3) have stable mechanical, physical and chemical properties in the physiological environment[85]. The selection of substrate materials is usually based on the properties such as electrical insulation, biocompatibility, durability, transmittance, etc. The most widely used electrode materials are inert metals, such as gold (Au), platinum (Pt), platinum black, iridium (Ir) and iridium oxide (IrOx), renowned for their high conductivity and biocompatibility, but many promising new materials have been developed for various needs in recent years.

(3) The development of flexible HDMEAs also necessitates careful consideration of fabrication methods, surface modification techniques, and packaging strategies to ensure optimal performance and durability in neural interfacing applications. Fabrication methods for Flexible HDMEAs intertwine various techniques to construct devices tailored to specific neural interfacing applications, with conventional MEAs often leveraging photolithography, etching, and physical vapor deposition to meticulously pattern and construct electrodes on typically rigid substrates like silicon. Surface modification of flexible HDMEA includes changes in surface chemicals and morphology, which can not only affect the surface area and change the impedance to improve SNR[53, 86], but also facilitate cellular adhesion of neurons to the surface of flexible HDMEAs[69]. Besides, packaging strategies are crucial to the reliability and lifetime of flexible HDMEA [87-89]. Suitable packaging should ensure the hermeticity for HDMEAs, to protect the inner parts of the HDMEAs from the physical environment, and to protect the host from any injury caused by chemical leakage or electrical leakage[87, 90].

3.3.4. Examples of State-of-The-Art Flexible HDMEAs

Neuralink introduced a scalable high-bandwidth BMI system. This system includes arrays of 96 flexible polymer threads, each with 32 electrodes, yielding a total of 3072 electrodes [72]. The electrodes are made of gold and treated with surface modifications by using the electrically conductive polymer poly-ethylenedioxythiophene doped with polystyrene sulfonate (PEDOT: PSS) and IrOx, in order to lower the impedance for electrophysiology and increase the effective charge-carrying capacity of the interface. The electrode array is packaged with polyimide into a compact implantable device with custom chips for low-power amplification and digitization. The entire package for 3072 channels is less than 23×18.5×2 mm^3. The thin-film HDMEAs provide superior brain tissue compatibility and precise, robot-assisted placement for targeted brain

mapping. Their compact design integrates a high-channel-count application specific integrated circuit (ASIC), optimizing size and power efficiency.

Uguz and Shepard [75] presented a high-density, mechanically flexible subdural surface microelectrode array for spatially controlled, bipolar, cortical stimulation. The electrodes are made of gold, coated with PEDOT: PSS, and packaged by an ultrathin film (4 μm) parylene. These electrodes have a diameter of 15 μm and pitch of 40 μm. with high-capacitance (>1 nF) and single neuronal resolution, the electrodes can be programmed to shape the charge injection front selectively at depths approaching 300 μm with a lateral resolution better than 100 μm. To combine surface stimulation with electrical depth recording, the flexible HDMEA incorporates an implantable shank on the same substrate. The shank extension has 10 electrodes reaching down to 500 μm below the pial surface.

Zhou *et al.* [45] developed a neuro-probe system, mimicking mosquito mouthparts, with four shanks, each housing 32-channel electrodes, totaling 128 channels(shown in **Fig. 1.2A**). Polyimide was used as its insulation layer, and metal stack of 5 nm chromium/150 nm nickel/50 nm gold was used as conductive layer. The flexible HDMEAs are 2.5 μm thick and 105 μm wide. The electrodes measure 25×15 μm^2 in size and are spaced 70 μm apart. These arrays were mounted on a sharpen tungsten wire to facilitate the insertion process. Each of the shanks could be inserted into the brain independently to target different regions. The system also has sensitive sensors to monitor insertion pressure without visual aid. It offers early warning detection for delicate intracranial tissues like vessels, minimizing the risk of damage during implantation. The system demonstrates outstanding postoperative performance, with a unit yield of up to 57% recorded 12h after surgery, and 77% of unit activities being tracked from 4 to 12 weeks.

This recent advances highlight the applications of flexible HDMEAs in closed loop BMIs. The summary of the most recent flexible HDMEAs integrated in closed-loop BMIs over the past five years is shown in Table 1.1.

4. CHALLENGES AND STRATEGIES IN DEVELOPING IDEAL FLEXIBLE HDMEAS

4.1. Challenges in Developing and Applying Ideal Flexible HDMEAs

Although the aforementioned state-of-the-art flexible HDMEAs have advanced the field in various aspects, the development of an ideal flexible HDMEA still requires further improvements. For instance, in terms of density, Neuralink has increased the electrode count to 3092 through multiple threads [72], yet the density per thread still significantly lags behind the most advanced rigid-based HDMEAs. Moreover, the insertion of flexible electrodes remains a significant challenge. Although robots [72] and specially designed insertion tools like mosquito mimic needles [45] can enhance insertion precision and reduce damage, these auxiliary methods, despite their improvements, cannot completely eliminate the direct brain tissue damage caused by the insertion assistants. Additionally, implants designed for human brain applications are expected to be reliable over long periods, potentially spanning years, but research into their long-term stability is not yet exhaustive. In essence, the development of flexible HDMEAs encounters several common challenges, and the creation of an ideal flexible HDMEA involves addressing both the general challenges inherent to HDMEAs and specific challenges unique to their flexible design. These challenges encompass mechanical, electrical, biological, chemical, and interconnection issues, among others, which will be thoroughly discussed in the following text.

4.1.1. Mechanical Challenges

Except the general mechanical failures for MEAs, flexible HDMEAs present unique mechanical challenges rooted in their respective material and structural properties. The main

failures of flexible HDMEAs in mechanical aspect could be classified into three types: (1) intrinsic failure of stable function, (2) insertion failure, and (3) failure to long time use in physiological environments.

Table 1.1 Summary of the most recent flexible HDMEAs integrated in closed loop BMIs

References	Electrodes Numbers	Electrode size	Center to center distance	electrode materials	packaging materials	lifetime being tested
(Fan et al. 2023)	16	Dia = 20 μm, 25 μm, 30 μm	150 μm	Cr, Au	Parylene	28 days
(Vajrala et al. 2023)	4	Dia = 40 μm, 100 μm	100 μm*	Ti, Au	Parylene	8 weeks
(Kauth et al. 2023)	30	1910 μm2	50.9 μm	Ti, Au	Polyimide	24 hours
(Zhou et al. 2023)	128	N/A	N/A	Au	Polyimide	16 weeks
(Chik et al. 2022)	8	20 × 40 μm	50 μm	Au	Parylene	5 weeks
(Eickenscheidt et al. 2022)	60	Dia = 10 μm, 22 μm, 50 μm, 150 μm, 582 μm, 1000 μm	200 μm	Indium tin oxide	Polyimide	N/A
(Wang et al. 2022)	8	Dia =25 μm	70 μm	Cr, Au	Polyimide	N/A
(Sperry et al. 2021)	60	100 μm2	40 μm	Platinum	Polyimide	6 weeks
(Ling et al. 2020)	16	Dia = 30 μm*	100 μm*	Au	Polyimide	2 weeks
(Silveira et al. 2020)	24	25 μm × 50/70 μm	50/70 μm	Ti	Parylene	N/A
(Guo et al. 2021)	8	Dia = 25 μm	70 μm	Cr/Au	Polyimide	N/A
(Yu et al. 2021)	32	30 μm x 30 μm	200 μm*	Cu	Polyimide	N/A
(Wang et al. 2022)	8	Dia = 25 μm	70 μm	Cr/Au	Polyimide	N/A
(Uguz and Shepard 2022b)	8	Dia = 15 μm	40 μm	PEDOT:PSS	Parylene	20 days
(Seo, Kim, and Kim 2020)	20	Dia=150 μm	350 μm	Ti, Au	PDMS, Parylene-C	N/A
(Esteban-Linares et al. 2023)	16	30 × 30 and 40 × 40 μm^2 for graphene, and 60 × 60 and 80 × 80 μm^2 for Au	200 μm	graphene or Ti/Au	Polyimide, PDMS	N/A
(Yang, Paulk, et al. 2021)	128	Dia = 30 μm	50 μm	PEDOT:PSS	Parylene C	N/A

*The value comes from an estimate of the pictures provided in the original articles.

The intrinsic failure of stability function emerges from the very nature of the flexible HDMEA, regardless of its operational environment. Typical problems include physical fracture or cracking of the electrodes, damage to the metal layer via corrosion, delamination due to poor adhesion between layers, the failure of the insulation layer led by pinholes or water penetration [52], thereby preventing the development of flexible HDMEAs.

The insertion of flexible HDMEAs into biological tissues introduces a substantial challenge[19]; maintaining vital flexibility, and/or minimizing cross-sectional dimensions might undermine stiffness, potentially jeopardizing the requisite rigidity for accurate insertion and inadvertently causing microelectrode buckling, tissue damage, or electrode misplacement [43]. The challenge arises if the stiffness of flexible devices is insufficient for neural tissue penetration, which often resulting in a more complex and less preferable insertion procedure [44, 91].

The harsh biological setting where electrodes are placed can compromise their mechanical stability, especially long-term post-implantation [41, 92]. This environment can induce electrode fracture, corrosion, delamination, swelling, dissolution, and mechanical stress, notably in the presence of continuous electrical stimulation [41].

4.1.2. Electrical Challenges

Developing HDMEAs suffers from high initial impedance because of the small-feature geometry, so that smaller electrodes are inherently noisier, exhibit worse recording quality, and are less functional because of decreased maximum possible stimulating current[53]. The rational impedance magnitude of electrodes at 1 kHz will be needed for quality recording. At least 40–150 kΩ is necessary in order to achieve the selective detection of the action potential from a single unit, but electrode's impedance greater than 5 MΩ recording of neural signals is overpowered[93, 94].

Even though the electrodes implanted into tissues for recording performed well in the acute phase, the performance was inconsistent and even lost the recording ability over a longer period [95]. Impedance will increase as diffusional barrier is formed in the body[95, 96]. Encapsulation failure and electrode breakage are another issue that might happen over time. A long-term *in vivo* study indicated that failure of the insulation material is the most significant factor in the reduction of both signal quality and impedance of implanted electrodes [97].

Crosstalk is another limitation of high-density recording devices, which may occur between electrodes if the space is too close, resulting in low SNR, signal transmission error, or signal loss [98, 99]. For neural applications, the crosstalk level has to be below 1% of the recorded signal level to make it negligible compared with the background noise [100].The electrode spacing should also be well designed, in which HDMEAs work in an excellent spatial solution with minimum crosstalk between electrodes [101].

In neural stimulation, the perfect electrode requires a robust storage capacity to seamlessly transmit current pulses, simultaneously curbing potential variations at the electrode/tissue nexus, thereby mitigating electrode polarization and thermal accumulation [102], which is a task that's notably arduous for flexible HDMEAs.

4.1.3. High-density Interconnection Challenges

Apart from the neural interface device itself, there's an inconspicuous yet critically important technical challenge: the integration of flexible sensor and backend stage [55]. This unique challenge restricts system integration and directly affects the stability and performance of HDMEAs[103]. SNR and low latency can potentially be improved through advancements in algorithms and backend technologies [104-106], but the wiring issue is the true critical problem that deeply troubles HDMEA designers. Traditional silicon-based probes, benefiting from the

development of modern electronics, have various mature and stable connection methods. However, the flexibility of the HDMEAs itself becomes a challenge for stable connections with subsequent systems [107, 108]. Setting stability aside, the hundreds or even thousands of connection points on HDMEAs make manual connections extremely difficult without specific tools or methods. This also restricts the possibility of expanding more electrodes on flexible HDMEAs [109]. The reliability issue of the soft-hard interface presents an additional challenge for making high density interconnection between flexible HDMEAs and backend electronics. The instability caused by inconsistent stress/strain concentration at the interface of two mechanically dissimilar materials can lead to delamination failure.

4.1.4. Chemical Challenge

In the existing literature, comprehensive reviews [41, 110, 111] discussed major chemical challenges of developing and applying MEAs in biological circumstances. Here we provide a concise overview. The challenges posed by the chemical environment to flexible HDMEAs are multifaceted, which include (1) the effects of the physical chemicals on electrodes, (2) the effects of the chemicals from the HDMEAs to the host tissues, and (3) stability for the long-term use. The physical intricate mix of organic and inorganic chemicals can impact the performance and longevity of the flexible HDMEAs. Despite the diverse materials and methods used in the fabrication of MEAs, many are not adequately prepared to handle the demanding physiological conditions. The physical chemical environment can threaten the stability of MEAs over both short and long durations, owing to a range of organic and inorganic reactions.

Additionally, the electrode's inherent chemical instability can be potentially harmful to the organism. Pt, for instance, has long been regarded as highly biocompatible and non-toxic. However, a recent study by Shepherd *et al.* [49] revealed that prolonged stimulation (lasting 6

months with a charge density of 267 μC/cm^2/phase) of Pt electrode arrays led to a notable production of Pt particulates. This, in turn, resulted in an escalated fibrous tissue response and weakened the quality of long-term records.

4.1.5 Biological Challenge

Biocompatibility is a crucial criterion for materials utilized in biosensors, ensuring they integrate harmoniously within biological environments. Yet, even when employing these biocompatible materials, inherent biological challenges continue to arise and need addressing[112]. Risks that can cause damage to the tissue and induce an acute inflammatory reaction include direct damage during surgery, mismatches between the electrode and tissue, micromovements of the electrodes, toxic damage by released chemical from the electrodes, etc. The body's responses to implanted HDMEAs include acute [40, 113, 114] and chronic [51] immune responses and damage repair processes, involving several distinct cell populations, such as erythrocytes, glial cells, neurons, etc. The processes include:

- Direct damage of the target tissue caused by the implantation of electrodes. The implantation of electrodes can mechanically cut or tear the target tissue, resulting in direct damage to local cells and blood vessels. This can lead to the entry of blood components (normally blocked by the blood-brain barrier) into brain tissue. Serum proteins, such as fibrinogen and albumin, adhere onto the surface of the electrode [40]. If the electrode materials of the HDMEAs are not biocompatible, they can cause local cell poisoning, irritation, and edema or even death. This, in turn, will further increase hydrostatic pressure around the electrode and harm more neurons, affecting the HDMEAs from collecting effective neuronal electrophysiological signals.

- Acute inflammatory reaction. The earliest inflammatory response can be caused by the erythrocytes, clotting, activated platelets, and blood vessels releasing factors due to vascular damage [113, 114]. Serum proteins promote the activation of microglia and macrophages, which then cause inflammation near the electrode surface [40]. Microglia cells, one of the major glial cell types involved in wound healing response in brain, are activated after implantation and release a large number of chemicals, including neurotoxic factors such as chemokines, cytokines, reactive oxygen species, and neurotransmitters. Neurons near the electrode (about 100 μm around the electrode, affected by the implantation process) suffer from direct damage and injury from these cytokines or exogenous chemicals, thereby resulting in a decrease in neurons around the electrodes[113]. As such malfunction of the electrode can happen among the surviving neurons.

- Chronic body response. Chronic body response to HDMEAs is mediated by active astrocytes and activated microglia. After the early wound healing, activated microglia around the electrodes releases enzymes and reactive oxygen species to destroy external substances, which are eventually phagocytosed by microglia. Microglia also regulates the production of extracellular matrix (ECM) proteins which contribute to the formation of glial scars. Some external substances that cannot be cleared by microglia, such as implanted electrodes, will lead to further immune activation and glial cell proliferation. Ultimately, astrocytes proliferate and lead to the formation of glial scars around the electrode, preventing further damage. The presence of the probe in the tissue can trigger a continued foreign body response [50], especially when a mismatch exists between the electrode and tissue and micromovements happened [115, 116]. Neurons lose their

electrical activity after surviving from acute reaction [96], resulting in reduced signal sources. The formation of glial scar can isolate the electrode from the surrounding neurons, reducing signal transmission by increasing the impedance of the tissue-electrode interface [51] and the distance between the electrode and target neurons [117].

4.2. Strategies and Advances in Developing Next-Generation Flexible HDMEAs

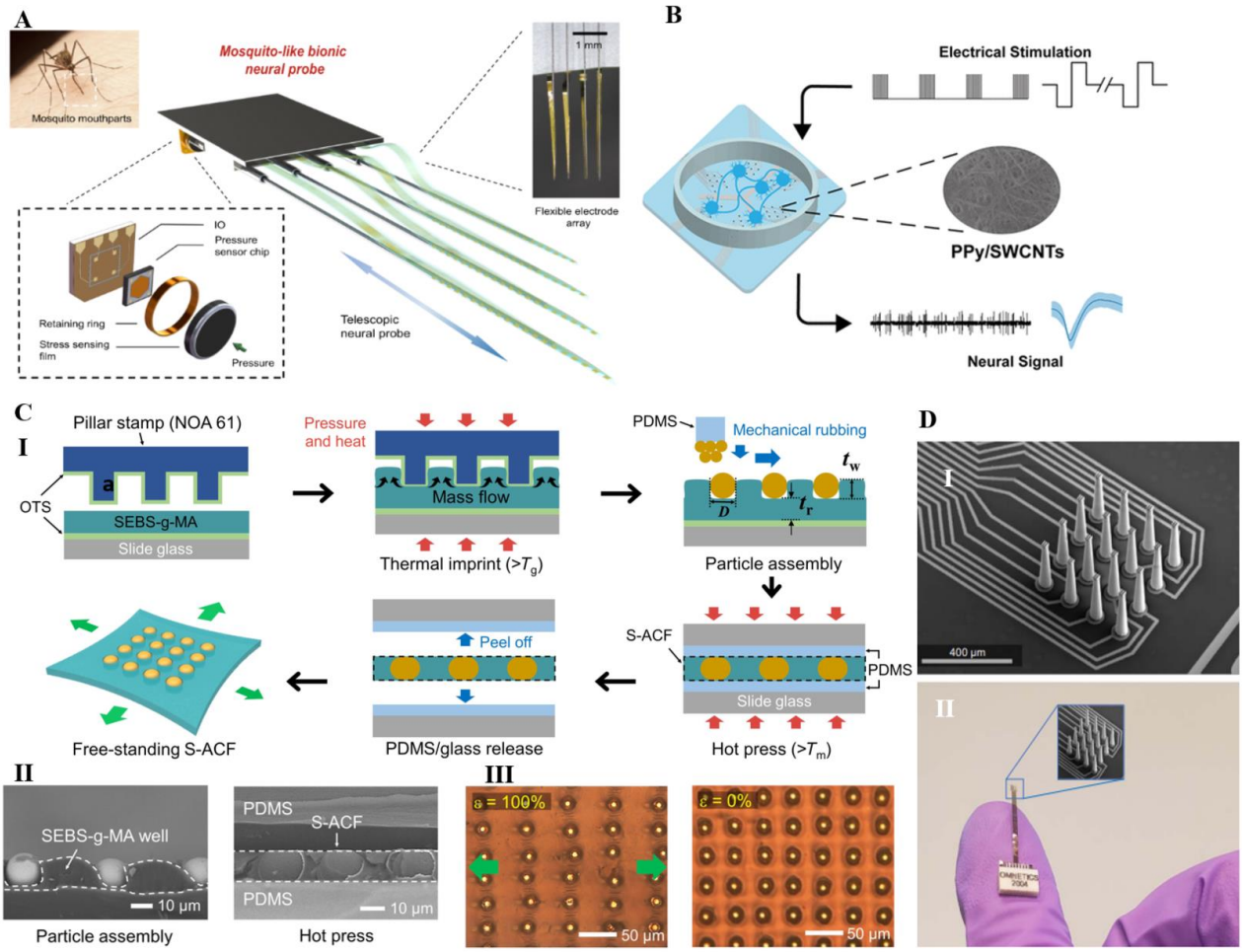

Figure 1.2. Reported strategies for advanced flexible HDMEAs. *(**A**) Multifunctional biomimetic neural probe system, with multichannel flexible electrode array and high sensitivity sensor array. Adapted with permission from [45] Copyright 2023 The Authors. (**B**) PPy/SWCNTs-modification on microelectrodes for electrical stimulation and detection. Adapted with permission from[118]. Copyright 2023 The Authors. (**C**) A periodic arrangement of stretchable ACF (S-ACF) incorporated within a thermoplastic block copolymer film. I) Scheme for the fabrication of the S-ACF. II) Left: Cross-sectional SEM image taken after the particle assembly in the template. Right: Cross-sectional SEM image of the S-ACF after the hot pressing. III) Optical images of the S-ACF when stretched (ε = 100%) and strain released (ε = 0%). Adapted with permission from [119] Copyright 2021 The Authors. (**D**) 3D-printed arrays for neural recording. Adapted with permission from [69] Copyright 2023 The Authors.*

4.2.1 Materials Advancement

Recent advancements in HDMEAs involve utilizing new materials for substrate and/or electroactive components or innovating with traditional materials to endow them with flexible properties. Compared to traditional materials, the newly developed materials possess unique properties specifically designed to address the demands of creating flexible HDMEAs. These properties include enhanced stretchability, better mechanical control, greater flexibility, and superior conductivity, among other advantageous characteristics. As a result, they are better equipped to tackle challenges in the mechanical, electrical, chemical, or biological domains. Some reviews by Gablech and Glowacki [120] and Tringides and Mooney[121] have been discussed about the material advances in MEAs development, thus we will just give an overview in this part.

To enhance biocompatibility, flexibility, and overall performance in neural interfaces, the advancement of substrate materials for flexible HDMEAs has incorporated innovative options such as hydrogels, silk, and polymers. Hydrogels, networks of hydrophilic, cross-linked polymer chains, have emerged as promising candidates for the next generation of bioelectronic interfaces due to their mechanical property similarity to biological tissue and versatility across electrical, mechanical, and bioengineering fields [74, 122]. Nevertheless, hydrogels also present challenges as substrate materials for flexible HDMEAs. Hydrogels' low Young's modulus can cause mechanical instability and deformation, their susceptibility to swelling and dehydration may alter interface stability, and their fabrication complexity restricts shaping for varied applications. By using the natural silk as an optical waveguide material, Zhou *et al.* [73] presented and flexible opto-electro neural probe, in which electrode arrays of 128 recording channels were integrated on a single probe. Silk has high transparency, excellent biocompatibility, and mechanical

controllability. The Silk-Optrode probe, upon hydration of the silk optical fiber, autonomously adapts to its post-implantation environment, minimizing its mechanical stiffness to facilitate high-fidelity brain insertion while preserving mechanical compliance with adjacent tissue.

To improve the flexibility of the conductive parts, graphene [123], carbon nanotubes (CNTs) [124, 125], and conducting polymers (CPs), such as PEDOT:PSS [126] have been developed for neural interfaces. Graphene, renowned for its notable flexibility and electrical conductivity, has become a pivotal material in neuronal interface studies and has been utilized to fabricate a range of flexible and stretchable electronic devices [127]. Still, it is vital to concurrently acknowledge and investigate its potential drawbacks, including long-term in vivo toxicity. Pure PEDOT: PSS hydrogels is brittle yet presents a high conductivity on the level of ≈ 40 S/cm. However, Li *et al.* [128] created a highly conductive and stretchable double-network (DN) conducting polymer hydrogel from PEDOT:PSS and poly(vinyl alcohol)(PVA) and achieved through in situ aggregation and densification, offering promising characteristics like high PEDOT:PSS content, electrochemical properties, and biocompatibility for potential use in bioelectronic applications. Hong *et al.* (Hong et al. 2022) developed flexible and transparent ultrathin (<10 nm) gold MEAs by using a biocompatible polyelectrolyte multilayer (PEM) metallic film nucleation-inducing seed layer. With the polymer seed layer, the ultra-thin gold film created through thermal evaporation exhibits effective conductivity, along with high optical transparency and superior mechanical flexibility. Furthermore, liquid metals (notably eutectic gallium–indium, EGaIn) have garnered significant interest in the realm of stretchable biodevices [129], due to their exceptional mechanical attributes, electrical conductivity, and biocompatibility.

4.2.2 Design in Geometries and Shapes

The utilization of dual-side design has emerged as a vital strategy to increase the electrode density in flexible neural interface applications across several research papers. By employing a dual-side design, it is possible to enhance electrode density without enlarging the probe's dimensions or reducing electrode size, thereby circumventing associated electrical challenges. Scholten *et al.* [19] introduced a novel polymer-based microelectrode array with an impressive 512 platinum recording electrodes, optimized for chronic recordings in the brains of behaving rats, and showcase advancements in polymer microfabrication and back-side electrode patterning. In the work of Kim *et al.* [130], a dual-side fabricated multimodal polymer neural probe was developed, featuring gold and platinum microelectrodes. Although a strategy of using multilayer with a sacrificial layer on the bottom could fabricate dual-sided flexible HDMEAs, it introduces challenges, such as misalignment during the multiple lithography processes[1]. A more straightforward and efficient method is still needed. Soft and stretchable electronics have been developed to create HDMEAs that can better conform to the brain's surface and accommodate its natural movements. With some ingenious designs, these devices not only exhibit greater flexibility and stretchability but also reduce mechanical issues common in traditional designs. Moreover, due to improved contact between the electrode and tissue, they can ensure enhanced electrical performance. The stretchable opto-electric integrated neural interface (SOENI) is designed to align with the mouse brain's somatomotor and somatosensory cortices [68]. It features a 3x3 microelectrode grid, 2x2 micro-LEDs, and a large reference electrode. Embedded within two silicone elastomer layers, the SOENI combines photostimulation and recording electrodes, with microscale light emitting diodes (LEDs) connected using a flip-on-chip method, aligning their illuminated surfaces with the microelectrode sites. Serpentine-shaped metal interconnecting

wires were designed to improve the stretchability. Similar serpentine structures were also used in some other latest microsystems [131, 132].

Mesh-like electrode designs have also been explored in order to improve the conformability of HDMEAs to the brain's surface and minimize mechanical stress on cell or tissue. For example, Le Floch *et al.* [57] reported "tissue-like" stretchable mesh nanoelectronics designed to align with brain organoids' mechanical properties, which can be folded into 3D structures by progenitor or stem cells, facilitating three months electrophysiological measurements. Inspired by implantable mesh electronics and organoid polymer scaffold growth, McDonald *et al.* [70] developed suspended mesh microelectrode arrays for neural organoids, incorporating four wells, each containing a mesh and 61 microelectrodes, which are adept for low-noise recordings and electrical stimulation with their sub-100 kΩ impedance at 1 kHz. These HDMEAs emphasized their ability to improve conformability to the brain's surface and minimize mechanical stress. These designs represent a significant shift towards structures that are more adaptable and less invasive than traditional electrodes.

4.2.3 Surface Modification Strategies

Surface modification strategies not only address the challenges of electrical, mechanical, and biological compatibility but also significantly enhance the overall performance of HDMEAs. A common method of surface modification is adding a layer of special materials on the electrode surface to change the electrode's properties. These materials include metals [133], conductive polymers [134], nanostructures [135, 136], and bioactive substances [137, 138]. PEDOT and its derivative are used to improve the electrical properties [1, 133] and modify the physical properties, such as transmittance [139]. The application of CNTs significantly increases the surface area, thereby increasing the charge storage capacity and the injection limit, with other

benefits such as good adhesion, non-toxicity, and stable properties [135, 136]. Yang *et al.*[118] used polypyrrole/carboxylated single-walled carbon nanotubes (PPy/SWCNTs) nanocomposites for electrode modification(shown in **Fig. 1.2B**). The nanocomposites not only improved the performance of microelectrodes with low impedance (60.3 +/- 28.8 kappa O) and small phase delay (-32.8 +/- 4.5.4 degrees), but also presented stability for in vivo stimulation and recording for 21 days. Neuroadhesive protein coating improves the chronic performance of neuroelectronics in the mouse brain [137].

Innovations in surface topology, with or without additional coating, have demonstrated improved recording quality compared to traditional planar electrodes. Mushroom-shaped microelectrodes improved the recording quality compared to planar MEA [140]. The enhanced microscale wrinkles on microelectrodes were obtained by oil extraction from the elastic substrate and electroplating modified materials PEDOT: PSS and platinum black (Pt-black) on the wrinkled microelectrode sites improve the total device performance in electrocorticography (ECoG) signal recording without causing any cracks, delamination, or exfoliation [141].

4.2.4 Connection Strategies for Flexible HDMEAs

Anisotropic conductive film (ACF) bonding process has become a feasible approach to address the high-density interconnection challenges of flexible devices [103, 142] , yet, the high-temperature, high-pressure bonding process limits the use of some flexible materials. However, Hwang *et al.*[119] introduced a stretchable anisotropic conductive film (S-ACF) capable of connecting high-resolution stretchable circuit lines to various electrodes, addressing the challenge of high-resolution stretchable interfacing at low temperatures through conductive microparticles in a thermoplastic film(shown in **Fig. 1.2C**).

Diverging from ACF, manufacturing a standard flat flexible cable (FFC) directly on the sensor to accommodate different connectors is also a viable approach. The zero insertion force (ZIF) connector can address the connection issue to some extent [143, 144], especially with its mechanical connection features, allowing sensors to be easily disconnected. This provides many conveniences for wearable, disposable HDMEAs. The easy-to-replace feature also makes it convenient for researchers to replace damaged sensors, which is especially valuable in some destructive experiments. However, this method seems a bit cumbersome when facing thousands of connection points. Especially the weight, size, and cost of the ZIF connector further restrict its application scenarios. The simplest method is to directly flip the sensor and affix the designed FFC directly onto a printed circuit board (PCB) or flexible PCB with conductive adhesive [55]. This method is straightforward, low-cost, and very suitable for HDMEAs with a smaller number of electrodes or in the prototype stage.

The instability of soft-hard interface can be addressed by either enhancing the adhesion between the materials or avoiding sudden changes from soft to hard, that is, by adding an intermediate layer/buffer layer to mitigate the transition. Ideally speaking, making the entire backend into flexible devices to form a fully flexible system would be best. By eliminating the differences between materials, this problem can be completely addressed. Zhang *et al.* report a capacitive pressure sensor [145]. Impressively, this sensor used CNT-doped PDMS, achieving both electrode and insulating materials using CNT-doped PDMS through tuning different doping concentrations. To some extent, this realized part of the full-flexibility goal. Such partial implementation alone resulted in surprisingly stable performance; the device remained stable even after 100,000 deformation cycles. This further confirms that aiming for a fully flexible design is undoubtedly a solution to the soft-hard interface issue.

4.2.5 Advances in Fabrication Techniques and Strategies

Various recent fabricating strategies, including multi-layer strategies[146] and dual-sided micropatterning[147-149] , have been proposed to attain high-density probe capabilities without enlarging the poflymer neural probes' dimensions. Meanwhile, the advances in fabrication techniques also facilitate the development of flexible HDMEAs. Traditional fabrication techniques, such as photolithography, have significantly advanced the development of flexible HDMEAs, yet they come with limitations, including intricate processes, challenges in fabricating 3D structures, and precision constraints. Recently, emerging technologies, such as precise laser ablation and laser lithography, have introduced more streamlined, direct, and even more accurate methods for making complex electrode structures.

3D printing techniques, such as laser ablation, laser patterning inkjet printing and direct laser writing, facilitate the streamlined fabrication of planar and 3D microelectrodes (**Fig. 1.2D**) without the need for photolithography and etching by eschewing multi-step procedures for a more straightforward implementation[38, 69, 150-152]. For example, soft and flexible gold microelectrodes with widths down to 3 μm were fabricated on a pliable PDMS substrate through a combination of supersonic cluster beam deposition and femtosecond laser processing[150]. Inkjet printing, garnering popularity for creating MEAs by directly depositing microelectrodes onto the substrate through single-step fabrication, facilitates the use of softer substrates compared to photolithography and permits the use of alternative conductive inks like PEDOT:PSS for printing conductive lines on soft substrate. However, it does come with the drawback of being notably expensive.

To effectively reduce crosstalk between interconnects, it is necessary to increase the distance or add a shield layer [98, 153]. Spacing them too far apart will inevitably increase the cable width

and enlarge the overall system size. The core contradiction lies between the excessive number of wires and limited space. Some designs compensate for width by adjusting thickness, that is, by using multiple layers to reduce the number of wires that each single layer needs to accommodate [154, 155]. Passive matrix and active matrix have become the mainstream architectures to address the signal readout of the array [103, 156]. The passive matrix design is relatively simple, consisting of intersecting rows and columns, with sensors set at the intersections[143, 157]. However, the crosstalk between sensors limits the quality of the signal. The active matrix addresses the crosstalk issue by adding switching units, such as diodes, to the electrodes [158, 159]. With the ideal performance comes complex circuit design requirements and internal structural issues. Nowadays, the flexible active matrix has become a mature technology used in the commercial display industry, which is worthy of designers' study.

5. APPLICATIONS OF MEAS IN NEUROSCIENCE

The advent of MEAs has significantly advanced the field of neuroscience, providing profound insights into neural dynamics at an unprecedented resolution[2]. MEAs have been playing across various neuroscience disciplines, ranging from cultured neural cells[160], neural organoids[161-164], and animal neural models(such as insects[1, 165], rodents[166-168], and Nonhuman Primate Brain[169, 170]) to complex clinical applications [171-173]. MEAs have been instrumental in mapping neural circuitry and decoding brain activity, facilitating the development of brain-computer interfaces (BCIs) that promise to restore motor function and communication in individuals with severe neurological disorders[2].

Beyond human neural applications, MEAs have been adapted for use in various animal neural models, providing a bridge between cellular studies and human clinical applications. This has enhanced our understanding of disease models, as well as providing innovative diagnosis and

therapeutic strategies. The study of extracellular neural responses in the antennal lobe neurons of live locusts, triggered by volatile organic compounds (VOCs), is particularly remarkable[165]. Biological olfaction is highly sensitive, capable of detecting VOC concentrations ranging from parts per billion (ppb) to parts per trillion (ppt), and can discern subtle changes in gas mixtures[174-180]. The locust olfactory system serves as an excellent model for detecting lung cancer VOCs. In this system, VOCs are initially perceived by olfactory receptor neurons (ORNs) in the antennae, which convert chemical signals into electrical impulses. These impulses are then relayed to the antennal lobe (AL), where they are further processed by a complex network of excitatory projection neurons (PNs) and inhibitory local neurons (LNs)[181, 182]. The precision and sensitivity of MEAs make them highly effective for such bioelectronic applications as VOC detection. Utilizing principles of neural activity monitoring, MEAs can detect biochemical signals, thereby broadening the scope of biomedical diagnostics. Integrating MEAs with biochemical sensing technologies enables researchers to identify specific VOC patterns associated with various diseases, including cancer. This could revolutionize early diagnosis and monitoring with non-invasive methods, highlighting the versatility of MEAs and their potential to innovate diagnostic tools in medical science.

6. SUMMARY

This chapter outlines the challenges and advancements in microfabrication techniques that enable the creation of such high-density, flexible neural interfaces. It also previews the applications of these MEAs in the context of neuroscientific research and biomedical diagnostics. MEAs have transformed neuroscience by offering unprecedented resolution in studying neural dynamics and finding applications across various fields, including cultured neural cells[160, 183], organoids, animal models, and clinical use [168-178]. They are pivotal in mapping neural circuits,

decoding brain activity, and driving innovations in brain-computer interfaces (BCIs) to restore motor and communication abilities for individuals with severe neurological disorders [168].

The utilization of dual-side design is one of the vital strategies to increase the electrode density in flexible neural interface applications [1, 2]. This approach enables higher electrode density without increasing the probe's size or reducing individual electrode dimensions, effectively avoiding the electrical challenges that often accompany such adjustments. We therefore will introduce unique and innovative fabrication strategies on developing flexible dual-sided MEAs in this dissertation. Chapter 2 will focus on the detailed methodologies and materials used in the construction of dual-sided MEAs. These flexible micro-probes developed initially adapted for the small brain structures of insects also provide a precise tool for neural recording in the intricate structures of more complex brains as well. This unique microfabrication method offers a groundbreaking approach to fabricating scalable, high-density electrode devices, holding significant promise for neuroscience and neurology. Chapter 3 will explore the application of flexible dual-sided MEAs by recording and decoding VOC evoked neural signals for early phase human lung cancer detection. By recording and decoding neural responses to volatile organic compounds, which are indicative of early-stage lung cancer, these flexible micro-probes offer a promising non-invasive tool for early cancer detection, potentially transforming approaches to diagnosis and monitoring in clinical settings.

CHAPTER 2: DEVELOPMENT OF FLEXIBLE DUAL-SIDED MICROELECTRODE ARRAYS

1. INTRODUCTION

In the dynamic field of neuroscience, the need of electrophysiological recordings from insect brain neurons has become essential, not only for understanding complex neuronal functions but also for classifying neural responses to external stimuli, especially in the context of biodetection [181, 182]. Particularly noteworthy is the study of extracellular neural responses in live insect (locust) antennal lobe neurons, triggered by VOCs[165]. To enhance the recording and analysis of neurophysiological signals in insects and to broaden the scope of potential applications of insect neural models, it is essential to develop special recording electrodes that can record from large number of neurons, simultaneously, in a tight space, and responds reliably over time. Tetrodes are commonly used in insect neural recordings [184, 185], but are limited by their design with only four widely spaced electrodes, rendering them relatively inefficient for detailed neural signals. MEAs present a more promising alternative [39, 166, 186-188]. Yet, in insect brain neurology, there is a growing need for flexible, multi-channel, or even high-density MEAs (HDMEAs). However, current research in this area still faces several gaps. First, the majority of existing HDMEAs are tailored for humans, rodents, or large animals, with only a few designed with the unique requirements of insects in mind. However, the brain of a locust is much smaller than a rat's hippocampus, with its antennal lobe having an effective area of about 500 μm in diameter. Even the most advanced HDMEAs available today, such as silicon-based Neuropixel 2.0 [186, 188] that have a distance of 175 μm from electrode to tip, are too large for effective use in such small brain regions. Second, high spatial resolution MEAs are necessary due to the inefficiency of using conventional MEAs with electrode sizes larger than 20 μm and/or distances exceeding 100 μm,

given the small size of the locust brain and its limited dimensions. The high-resolution multichannel MEAs provides benefits in neural voltage recordings with high spatial and temporal detail, offering a holistic perspective on the neural dynamics. Finally, there is a necessity for flexible MEAs in the realm of insect biosensing. Although rigid MEAs offer precise measurements and reliable data acquisition [42, 173, 189, 190], flexible MEAs offer a more intimate and sustained interface with tissues, thereby enhancing signal quality and providing precise spatiotemporal scale of neuronal activity [1, 113, 166, 191-195].

Current techniques to craft these flexible electrodes are as varied as they are ingenious, including multi-layer metal process[148], electron beam lithography[196, 197], and two sides [147-149]. Among current techniques to craft flexible HDMEAs, the double-sided configuration is a promising solution, not only doubling the channel count without increasing the size of the probe but also enabling signal recording from both sides[187]. Various methods exist for implementing dual-sided MEAs [147-149, 198-200], each with its own pros and cons. For example, Stieglitz [198] used plasma dry etching to directly expose electrodes on both sides of polyimide probes using polyimide and a two-step RIE process. Specifically, the author used polyimide as the substrate and insulation material and integrated several metallization layers into the structure. The first RIE was applied to open electrodes and contact pads on the top side, and then the polyimide foil was peeled off from the wafer and turned upside-down in the RIE reactor. After a second RIE etching step, the polyimide sacrificial layer was removed, and the back-side electrodes were opened. This method offers a promising approach for fabricating double-sided MEAs (so called flexible nerve plates), with a with a diameter of 226 μm and resulting in a geometrical electrode area of 40115 μm^2. However, this method required removal and re-attachment of the polyimide films for dual-sided processing. Its primary challenge lies in the need to peel off and invert the polyimide foil before

proceeding with subsequent microfabrication steps, including metal layer deposition, mask alignment, photolithography, patterning, and RIE. Any irregularities or deformations in the polyimide foil during this process could jeopardize the entire fabrication strategy. To address this issue, Tooker et al. [149] utilized SF_6 plasm-etched silicon posts to create recessed electrodes from the bottom polyimide surface. Nevertheless, this method may become extremely challenging in fabricating high-density electrodes due to the complexity of silicon etching. Additionally, Kim et al. [147] and Scholten et al. [148] combined multi-layer designs with sacrificial metal layers to fabricate dual-sided probes. However, one of the challenges of this method lies in the complexity of achieving a solid attachment between the sacrificial metal layer and the carrier wafer, as well as establishing a robust adhesion between the electrode metal layer and the isolation layer. The isolation layer needs to firmly connect to the sacrificial layer yet easy to etch for releasing the devices, all while ensuring that the bond between the electrode metal and the isolation layer is strong enough to endure the entirety of the neural probe fabrication process (especially in the releasing period, for more than 7 days in Al etchant, and 2.5 days in Cu etchant) and prolonged usage. While a combination of multi-layer designs with sacrificial metal layers offers the potential for complex electrode configurations, challenges remain in achieving robust attachment between the sacrificial metal layer and the carrier wafer, as well as ensuring strong adhesion between the electrode metal layer and the isolation layer. Alternative methods involved the use of tapes[199] or adhesive glue [200] that are limited in scalability.

PEDOT:PSS is extensively utilized as a surface coating material in bioelectronics [1, 2, 201-205]due to its exceptional combination of electrical, mechanical, and biocompatible properties. It facilitates efficient signal transduction between biological tissues and electronic components, which is crucial for applications such as neurophysiological recordings[203]. Moreover, PEDOT:PSS

exhibits excellent biocompatibility, minimizing adverse reactions when interfacing with biological systems—a vital attribute for biosensors and neuroprosthetics[204]. The material's mechanical flexibility allows it to conform closely to the soft nature of biological tissues, reducing the risk of damage during operation and ensuring long-term functionality[202]. Additionally, PEDOT:PSS forms stable films with strong adhesion to various substrates, enhancing the durability of coatings under physiological conditions[205]. Its properties can be tailored through chemical modifications or additives, allowing customization for specific applications[201]. Compared to traditional conductive materials like metals, which lack flexibility and may pose biocompatibility challenges, or carbon-based materials that are difficult to process, PEDOT:PSS offers a more adaptable and effective solution for creating seamless interfaces between electronic devices and biological systems. However, the current reported coating methods lack sufficient in providing information about using low coating voltage and coating quality. This voltage range was chosen to ensure that the deposition process occurred within a safe electrochemical window, preventing damage to the gold substrate.

In this context, our research represents a significant leap forward. We first conducted serial study on low voltage window (to prevent damage to the gold) and coating cycles with CV technique, to find optimized PEDOT: PSS coating strategy for gold electrodes. We then introduced an innovative yet effective method for fabricating dual-sided MEAs based on flexible Parylene substrate, employing folding and annealing techniques. This method effectively doubles the channel count and density within the same spatial footprint compared to their single-sided counterparts. Our primary focus with these advanced MEAs is to explore their potential in the multichannel recordings from the locust brain, particularly for the detection of odor-evoked neural responses from the antennal lobe neurons. This application is not only intriguing but also of

substantial practical significance. This approach of enhanced and robust detection of multiple neural activities simultaneously from the insect brain has several applications including understating the roles of functional neural computations in learning and memory as well as possible applications in detection of volatile chemicals which are important for medical diagnostics (e.g., breath analysis), homeland security (e.g., explosive detection), and environmental (air pollutants) applications.

2. METHODS

2.1. Design of the Flexible Dual-Sided MEAs

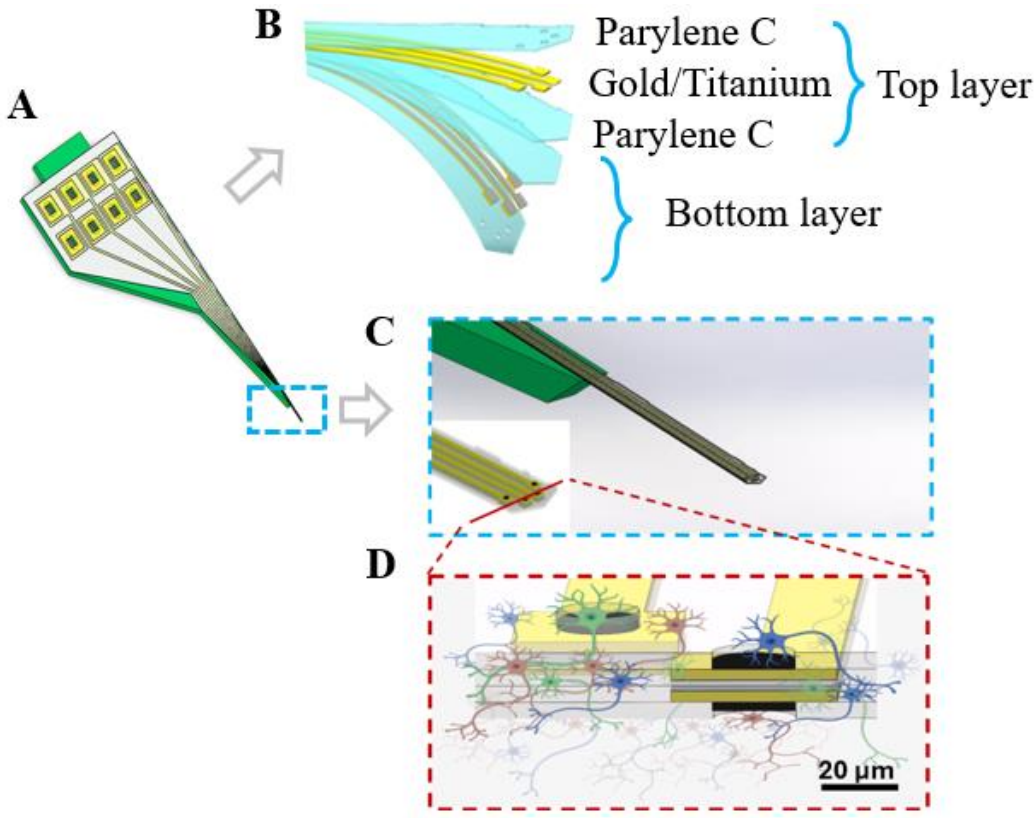

Figure 2.1. The schematic of the flexible dual-sided MEAs. (***A)*** *Dual-sided polymer-based MEA assembled on customized PCB.* (***B)*** *stacking layers of the MEA.* (***C)*** *Tips of the MEAs, and* (***D)*** *Cross-section of the MEA tip.*

The designs of these MEAs are specifically tailored for the locust antenna lobe, the central hub for odor processing in insects. As shown in Fig. 2.1, the flexible dual-sided MEA features a

multilayer structure of parylene C layer (acting as substrate and encapsulation) and metallization layer (acting as electrodes, traces, and contact pads). In Fig. 2.1A, the dual-sided polymer-based MEA is shown assembled on a customized printed circuit board (PCB), which allows for stable electrical connections and easy integration with external recording systems. Fig. 2.1B illustrates the layers of the MEAs, highlighting the Parylene C encapsulation and the gold metallization layer. This multilayer structure is vital for achieving mechanical flexibility while protecting the electrodes and electrical traces. In Fig. 2.1C, the tip of the MEA is displayed, showing the arrangement of the electrodes at the tip. Fig. 2.1D provides a cross-sectional view of the MEA tip, showing how the multilayer structure is organized to enable dual-sided recording capability. The MEAs in 4, 6, or 8 electrode configurations were designed with an electrode diameter of 20 μm and a minimal center-to-center distance between electrodes of 50 μm. The tip width was 120, 180 and 230 μm for 4-channel, 6-channel, and 8-channel devices, respectively. With a 20 μm electrode diameter and similar trace width and spacing, a density of 327-348 channels/mm² can be achieved across various channel configurations.

2.2. Folding-Annealing Strategy for Microfabrication of Flexible Dual-Sided MEAs

The microfabrication process for the flexible dual-sided MEAs employs a novel folding-annealing strategy, which significantly increases the channel density without expanding the physical footprint of the device. The microfabrication flow is shown in **Fig.** 2.2 and the schematic of the fabrication processes is shown in **Fig.** 2.3.

To start with, single-sided planar MEAs were constructed using conventional semiconductor microfabrication techniques including chemical vapor deposition of parylene C, thermal evaporation of metal, and photolithographic patterning (Fig. 2.2). A 5-μm-thick layer of parylene C was deposited on a 4-inch-diameter silicon wafer using room temperature chemical vapor

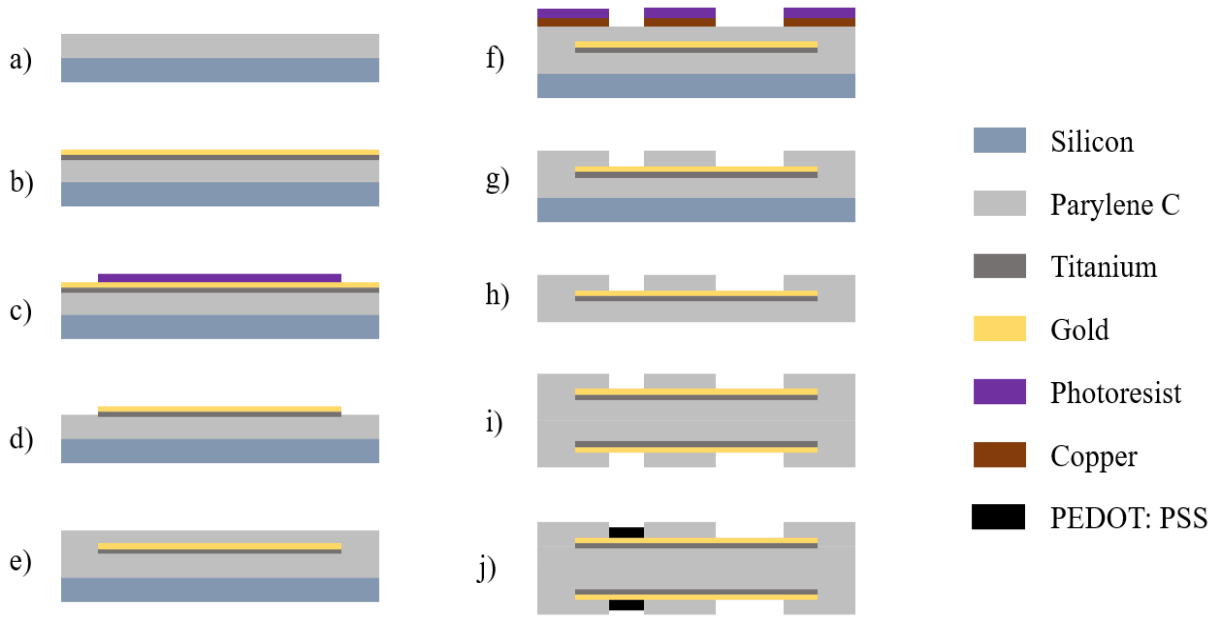

Figure 2.2. Fabrication process flow of the MEAs: *(**1**) Deposit Parylene-C on a wafer; (**2**) Deposit Ti/Au; (**3**) Pattern Ti/Au; (**4**) Wet etching of metal; (**5**) Deposit Parylene-C; (**6**) Deposit and pattern a copper mask. (**7**) Plasma dry etching of Parylene-C, (**8**) Releasing device. (**9**) Folding, annealing, and bonding the MEAs. (**10**) PEDOT:PSS coating.*

deposition (SCS Labcoter® 3, Specialty Coating Systems, Indianapolis, IN, USA). Then, a metal stack of Ti (10 nm) and Au (200 nm) was sequentially deposited using a thermal evaporator (Edward Auto306, Edwards, UK). The electrode sites, traces, and contact pads of the MEAs were defined by ultraviolet (UV) photolithography of a positive photoresist (PR, S1813, Shipley, Marlborough, MA, USA), and patterned by wet etching in gold etchant (Millipore Sigma, St. Louis, MO, USA). After that, photoresist was removed with acetone, followed by rising with ethanol and deionized (DI) water. Next, a second 5-µm-thick layer of parylene was deposited as the top encapsulation, followed by thermal evaporation of a 200-µm-thick layer of copper. The outline of the planar MEA, the folding slot, and open windows of electrode sites were defined by UV photolithography of photoresist. Subsequently, copper was patterned by wet etching in copper etchant (Millipore Sigma, St. Louis, MO, USA) to form as a hard mask. Oxygen plasma etching was performed in a reactive ion etching system (RIE-1701 plasma system, Nordson March, Inc,

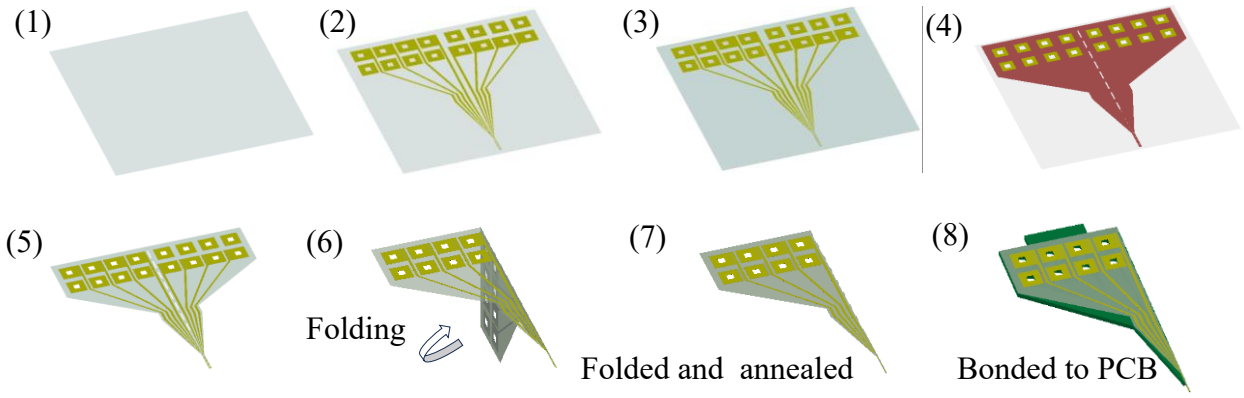

Figure 2.3. Schematic that shows the microfabrication*, including* ***(1)*** *5um PA deposited on silicon wafer,* ***(2)*** *A metal stack of 200nm Au and 20nm Ti were thermal deposited and patterned on PA substrate,* ***(3)*** *Another layer of 5um PA was deposited,* ***(4)*** *Pattern and Reactive Ion Etching the shape of MEAs and the openings of electrodes and contact pads,* ***(5)****releasing,* ***(6)****folding,* ***(7)****annealing,* ***(8)*** *assembling.*

Westlake, OH, USA) to remove unwanted parylene C, to expose the electrodes sites and contact pads as well as to form the shape of the planar MEAs.

Subsequently, the planar MEAs were released from the wafer and then folded along the middle line, after which they were thermally bonded with an annealing process to form the dual-sided structure. After being released from the wafer, the planar devices were folded along the middle line, thermally bonded at 75°C in an oven for 3 hours and left for cooling down over night.

To facilitate interconnects to external recording instruments, the resulting dual-sided MEAs were assembled and bonded onto a customized printed circuit board (PCB) using conductive silver paste(8331-14G, MG Chemicals, Canada). Contact pads with central holes were uniquely designed to ensure robust electrical contact between silver paste and PCB pads from both sides of the array. The assembled device had a flexible tip on the MEA region, while the PCB-enforced backbone provides ease of device handling during insertion and recording experiments.

Finally, cyclic voltammetry (CV), with voltage from -0.7 to 0.9 V and scan rate at 10 mV/sec, was employed to electrodeposit poly(3,4-ethylene-dioxythiophene) polystyrene sulfonate

(PEDOT:PSS) onto gold electrodes, enhancing their electrical properties.

2.3. Electrode Surface Modification Through Low Voltage Cyclic Voltammetry for Enhanced Performance

To assess the effects of PEDOT: PSS coatings on the electrochemical performance of gold electrodes of different sizes and determine an optimal electrode size for further investigation, we fabricated single-channel gold electrodes with openings measuring 10 μm, 20 μm, 50 μm, and 100 μm. We employed cyclic voltammetry (CV) to electro polymerization of PEDOT: PSS onto gold single-channel electrodes, using a three-electrode system. The voltage was from -0.7mV to 0.9mV, scan rate was 10 mV/sec.

Electropolymerization of PEDOT: PSS on gold electrodes were achieved using a CV technique with a three-electrode setup, in which the MEAs act as the working electrode (WE), a platinum wire as the counter electrode (CE), and a standard Ag/AgCl electrode as the reference electrode (RE). This process was conducted in a monomer solution of 10 mM 3,4-Ethylenedioxythiophene (EDOT, Millipore Sigma, St. Louis, MO, USA) and 0.7 wt.% Poly (sodium 4-styrenesulfonate) (PSS, Millipore Sigma, St. Louis, MO, USA) in DI water. The solution was stored in 4°C refrigerator and deoxygenated by purging with nitrogen gas and then vacuuming for 20 mins before use. CV was performed using a potentiostat (6149E, CH Instruments, Austin, TX, USA), with voltage ranging from -0.7 V to 0.9 V vs. the Ag/AgCl RE and a scan rate of 10 mV/s.

2.4 Approaches to Evaluating the MEAs

2.4.1 Optical Microscopy and Scanning Electron Microscopy (SEM)

Optical microscopy was utilized to inspect the structural morphology and integrity of the MEAs during various processing steps, including releasing from the wafer, folding, annealing, and

PEDOT:PSS coating. Furthermore, scanning electron microscopy (SEM) was used to evaluate the electrodes before and after PEDOT:PSS coating.

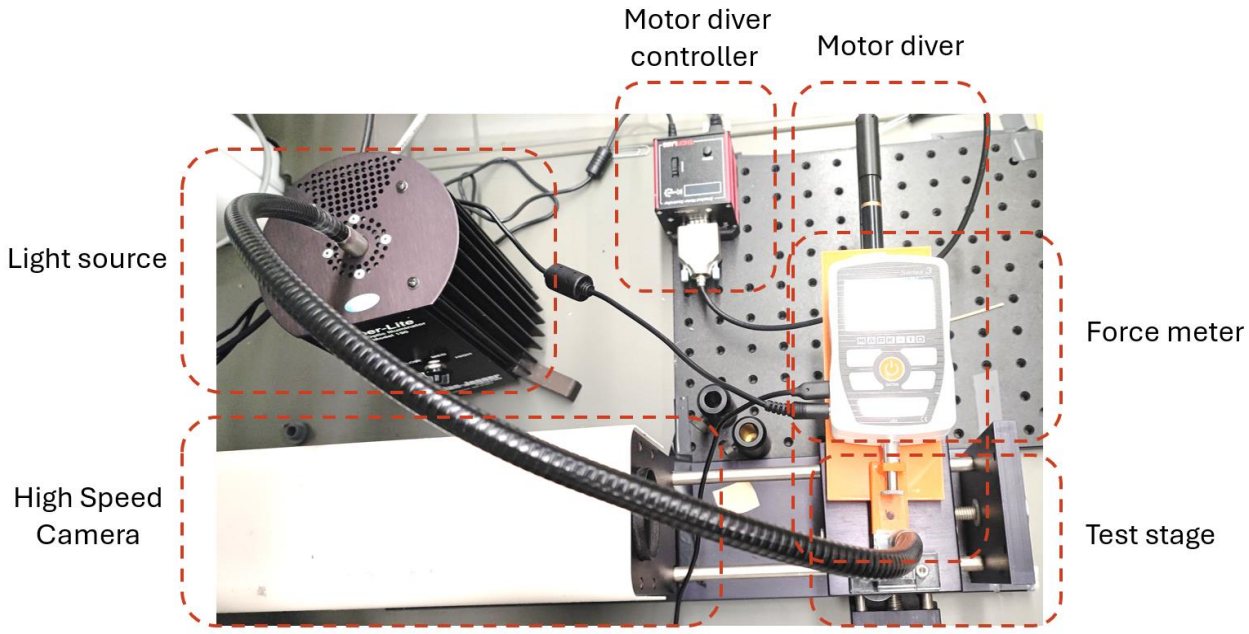

Figure 2.4. Bench-top Setup for Insertion Tests. *This figure displays a comprehensive setup used to measure the mechanical properties of microelectrode insertion. The setup includes a force meter to quantify the insertion force, a high-speed camera paired with a light source to capture detailed visual documentation of the insertion process, motor drivers controlled by precision controllers to regulate the movement and speed of the microelectrode, and a stable test stage where the microelectrode is inserted into simulated neural tissue. This configuration allows for precise assessments of the microelectrode's mechanical behavior during insertion, crucial for minimizing tissue damage in clinical applications.*

2.4.2 Electrochemical Impedance Spectroscopy (EIS)

EIS was conducted using a potentiostat (6149E, CH Instruments, Austin, TX, USA) in a phosphate buffered saline (PBS) solution in a three-electrode setup with the MEA WE, a Pt CE and an Ag/AgCl RE. The A.C. impedance of the electrodes was measured in a wide frequency range of 1 Hz to 100 kHz and acquired using commercial CHI software.

2.4.3 Surface Morphology and Effective Surface Area

Scanning electron microscopy (SEM, Hitachi S-4700, Hitachi High Technologies America, Inc., USA) was utilized to analyze the surface morphology of the electrodes with and without the

PEDOT:PSS coating. Surface roughness were measured with an optical profilometer (WYKO nt2000, Bruker, MA).

2.4.4 Effective Areas Measurement

In this experiment, the CV responses of the electrode were electrochemically measured in 0.5 mM $K_3[Fe(CN)_6]$ at varying scan rates of 0.02 V/s, 0.05 V/s, 0.1 V/s, 0.2 V/s, and 0.5 V/s. The effective areas of electrodes were calculated using an Randles-Sevcik equation [206, 207]:

$$i_p = 2.69x10^5 n^{\frac{3}{2}} A D^{\frac{1}{2}} C v^{\frac{1}{2}} \quad (1)$$

where i_p is the cathodic peak current, n is the number of transported electrons, A (cm^2) is the effective electrochemical surface, D ($cm^2 \cdot s^{-1}$) is the diffusion coefficient, C ($mol \cdot cm^{-3}$) is the concentration of redox species, and v (V s^{-1}) is the potential scan rate. The dependency of the anodic peak potentials on the natural logarithm of the potential scan rate was investigated and linear regression lines were generated using the cathodic peak current and the square root of the potential scan rate as variables.

2.4.5 Mechanical Properties for Bending

To assess the mechanical stability of the electrodes under bending stress, we performed tests where the electrodes were bent at the 90° angle. Electrochemical impedance spectroscopy (EIS) measurements were taken before and after bending to evaluate any potential changes in their electrochemical properties. The results showed no significant differences in EIS values before and after bending, indicating that the electrodes maintain their stability and functionality even when subjected to bending 90° angle.

2.4.6 Mechanical Properties for Insertion

The mechanical property testing setup for insertion is illustrated in **Fig. 2.4**. A Brushed motor controller (KDC101, Thor Lab, USA) was utilized to perform the insertion of the dual-sided MEAs

into a brain phantom (0.6 wt.% agarose gel), with a penetration depth of about 500 µm inside the gel. The electrochemical impedance of the electrode was measured before and after 10 repeated insertions. Likewise, the insertion capability of the MEAs was verified *in vivo* using isolated insect brains, and the device's EIS was tested before insertion and after 15 times *in vivo* insertion.

2.4.5 Bench-Top Recording Performance

To evaluate the bench-top recording performance of the flexible dual-sided MEAs, we conducted controlled recordings using a saline bath setup. This setup, as shown in **Fig.** 2.5, allowed us to simulate neural environments and test the ability of the MEAs to capture extracellular signals with high fidelity. The MEAs were connected to a preamplifier and recording system, and a series of known electrical signals were applied to assess the device's sensitivity and SNR.

For the recording tests, a function generator was used to introduce simulated physiological pulses into the PBS solution, replicating neural signals. Neuronal-like signals were generated using

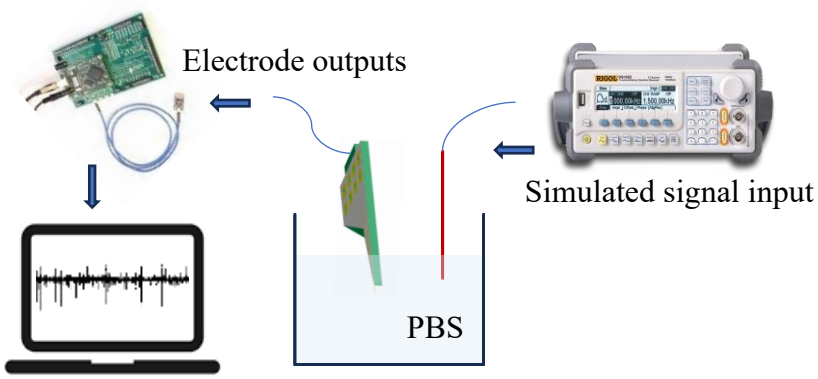

Figure 2.5. Schematic of setup for bench-top recording performance tests.

a neuronal signal simulator (NSS, BlackRock, USA) and transferred into the 1× PBS solution via resistances and wires, creating pulses with peak voltages of 100 µV and 200 µV. The recording tip of the MEAs was submerged in the solution to capture these simulated neuronal spikes.

Baseline noise was recorded, and the noise level was quantified as the root mean square (RMS) value over a period without any spike activity. The SNR was calculated by comparing the amplitude of the signal to the baseline noise levels. The SNR was calculated using the formula: SNR = (sigma squared for Signal) / (sigma squared for Noise), where Signal represents sorted spikes, Noise represents data between all spikes. The Signal StdDev represents the standard deviation of the spike waveforms, which are the signal of interest. The Noise StdDev represents the standard deviation of the intervals between spikes, which is considered noise.

2.4.6 Soaking Tests

To evaluate the stability and durability of the electrodes over time, a soaking test was performed. The electrodes were immersed in a phosphate-buffered saline (PBS) solution at room temperature. The electrochemical impedance spectroscopy (EIS) of the electrodes was measured to assess the

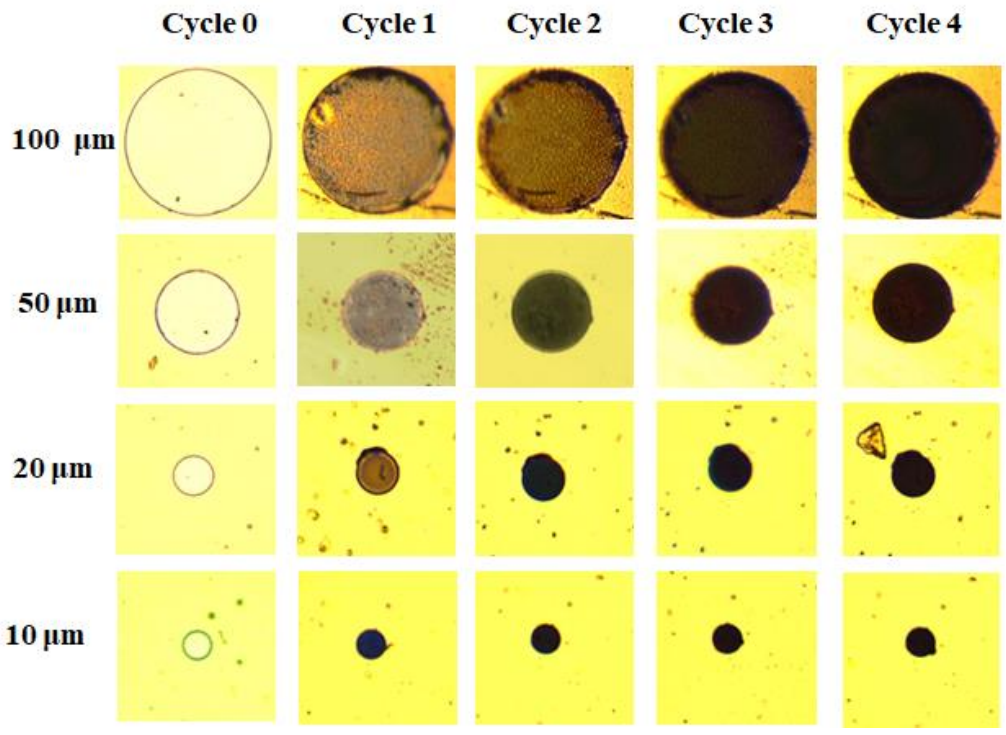

Figure 2.6. Microscopy images of the electrodes in varying sizes under different coating.

impedance changes over a period of seven days. The impedance measurements were recorded on Day 0, Day 1, Day 3, Day 5, and Day 7. Two different coating conditions were compared: electrodes coated with PEDOT: PSS after 2 CV cycles and those coated after 4 CV cycles. This approach allowed us to assess the electrochemical stability of the PEDOT: PSS coatings under prolonged exposure to a fluid environment over time.

3. RESULTS

3.1. Explore the optimize surface modification strategy of PEDOT: PSS deposition on gold electrodes in different sizes

To assess the effects of PEDOT: PSS coatings on the electrochemical performance of gold electrodes of different sizes and determine an optimal electrode size for further investigation, we fabricated single-channel gold electrodes with openings measuring 10 μm, 20 μm, 50 μm, and 100 μm. We employed cyclic voltammetry (CV) to electro polymerization of PEDOT: PSS onto gold single-channel electrodes, using a three-electrode system. The voltage was from -0.7mV to 0.9mV, scan rate was 10 mV/sec. This voltage range was chosen to ensure that the deposition process occurred within a safe electrochemical window, preventing damage to the gold substrate. The number of CV cycles was varied to investigate the influence of multiple coating layers on the electrode's performance.

3.1.1. Microscopy and SEM Analysis of the Effects of Low Peak CV and Coating Cycles

As shown in **Fig.** 2.6, the optical microscopy images confirmed the successful polymerization of PEDOT: PSS on electrodes in various sizes (10 μm, 20 μm, 50 μm, and 100 μm) through multiple CV cycles. The SEM images revealed a consistent increase in the thickness of the PEDOT:PSS layer with each additional cycle of CV deposition, as the optical version color became darker with the more coating cycles. Across all electrode sizes (10 μm, 20 μm, 50 μm,

and 100 μm), the deposition was uniform and smooth when more CV cycles were applied with the low peak voltage range that we used.

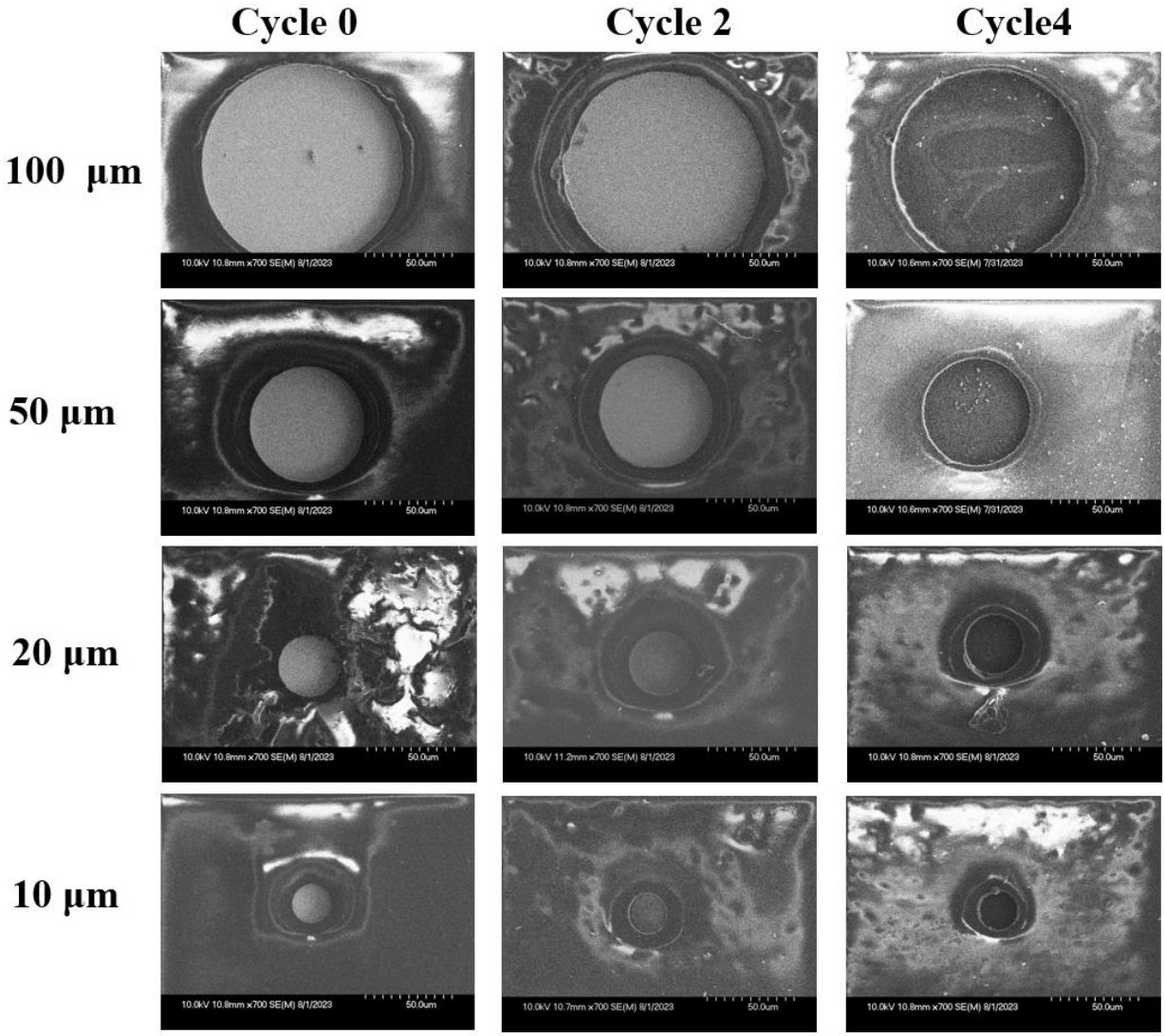

Figure 2.7. SEM images of the electrodes in varying sizes under different coating cycles.

The SEM images, as shown in **Fig.** 2.7, further illustrated the structural integrity and surface morphology of the PEDOT: PSS coatings on the electrodes across different sizes (10 μm, 20 μm, 50 μm, and 100 μm). As shown in **Fig.** 2.7, the coating appeared continuous and uniform, with no visible cracks or irregularities. The thickness of the PEDOT: PSS layer increased proportionally with each additional CV cycle, leading to smoother surfaces on the gold electrodes. Notably, the

low-voltage range applied during deposition helped to maintain the smoothness of the surface, preventing the formation of rough textures or defects that could otherwise impair electrochemical performance. These results confirm that the deposition process effectively enhanced the surface area and stability of the electrodes, crucial for optimizing the electrochemical properties in subsequent neural recordings.

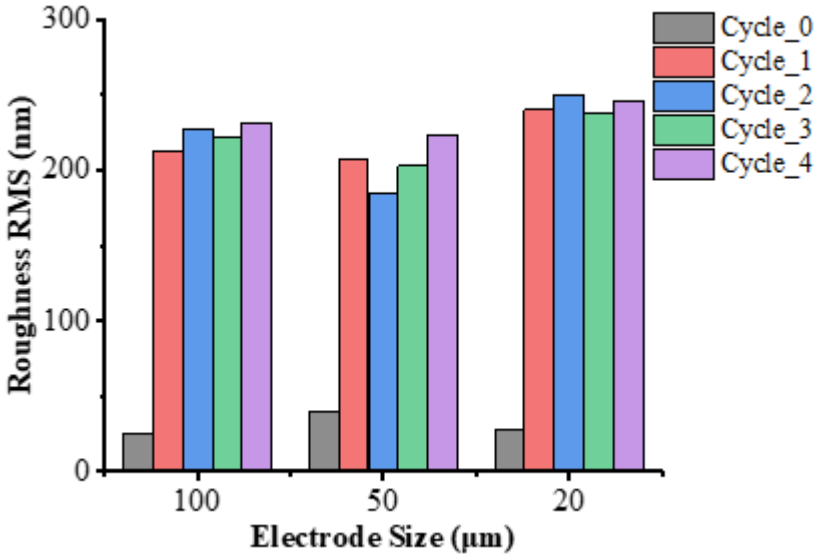

Figure 2.8. Roughness of the electrodes in varying sizes under different coating cycles.

3.1.2. Surface Roughness Characterization

To further quantify the surface roughness of the electrodes after PEDOT deposition, we utilized an optical profiler. Initial results indicated that the first cycle of PEDOT coating significantly increased the surface roughness of all electrodes, as shown in **Fig.** 2.8. However, further CV cycles did not substantially increase the surface roughness. This indicates that under the low voltage range during CV, multiple cycles of PEDOT: PSS deposition will maintain a smooth surface without significantly increasing the surface roughness. This result was consistent across all electrode sizes (10 µm, 20 µm, 50 µm, and 100 µm).

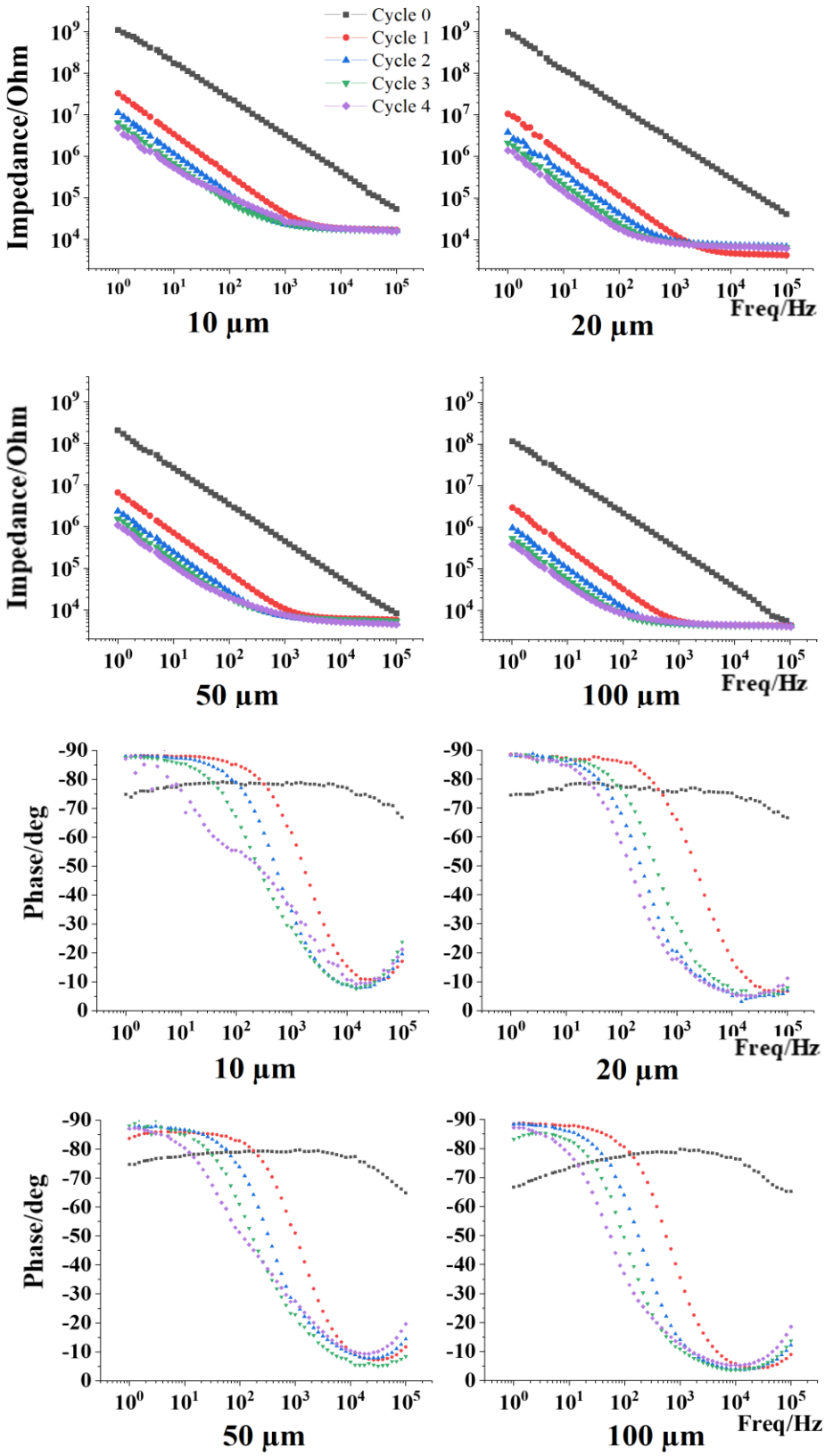

Figure 2.9. EIS results of the electrodes in varying sizes under different coating cycles.

3.1.3. Electrochemical Properties of The Electrodes

As shown in **Fig.** 2.9, After 1 cycle of CV coating with PEDOT: PSS, the electrode's impedance reduced significantly in all size electrodes. The 1 kHz impedance results were shown in **Fig.** 2.10. For the 10 μm and 20 μm electrodes, after one cycle of coating, the impedance at 1 kHz decreased by two orders of magnitude, while for the 50 μm and 100 μm electrodes, the impedance at 1 kHz decreased by one order of magnitude. A second cycle of CV coating further decreased the impedance, with a greater reduction observed for smaller electrode sizes.

However, increasing the number of CV coating cycles to three or four did not lead to a further reduction in impedance. The impedance at 1 kHz for the 20 μm, 50 μm, and 100 μm electrodes converged to a range between 10^3 and 10^4 ohms. This impedance range is suitable for neural recording applications. In other words, with two cycles of CV coating, a 20 μm electrode can achieve similar impedance values as larger electrodes, such as 50 μm or 100 μm electrodes. The 10 μm electrode exhibited slightly higher impedance relative to the 20 μm electrode, ranging from 2×10^2 to 3×10^4 ohms. However, it is worth noting that fabricating flexible electrodes with a 10 μm size is more challenging compared to the 20 μm size.

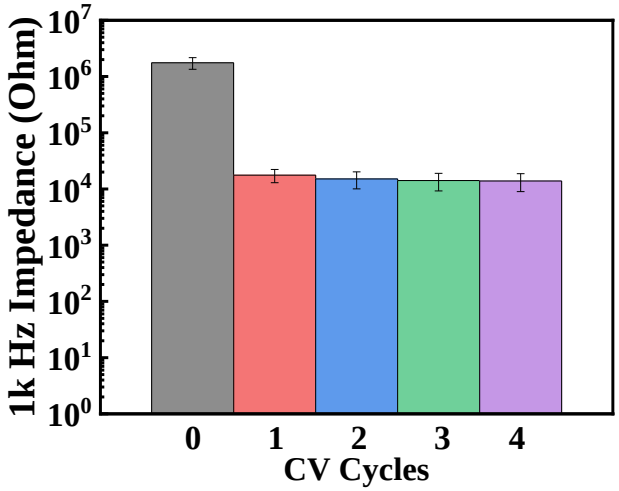

Figure 2.10. 1 kHz impedance of the electrodes in varying sizes under different coating cycles.

3.1.4. Effective Area of the Electrodes

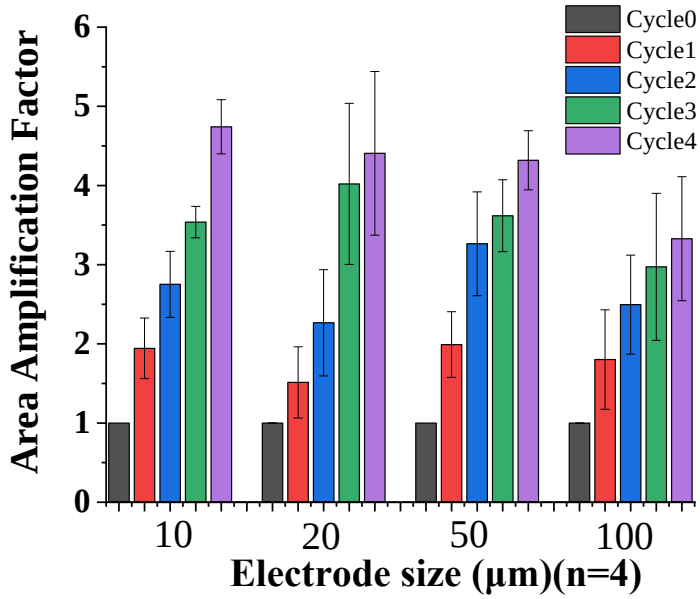

Figure 2.11. Effective area amplification factors of the electrodes in varying sizes under different coating cycles.

We also measured the effective area of the electrodes before and after PEDOT: PSS deposition. The results showed that increasing the number of CV cycles led to a corresponding increase in the effective surface area of the electrodes, regardless of their size, as shown in **Fig. 2.11**. This increase in effective area is critical for improving the electrochemical performance of the electrodes, particularly in terms of reducing impedance and enhancing charge transfer capabilities. Notably, the increase in the effective area continued even when surface roughness remained unchanged.

Here are a brief summary of the results presented in this section. The aim of this section was to optimize the deposition of PEDOT: PSS on gold electrodes of varying sizes (10 μm, 20 μm, 50 μm, and 100 μm) using CV with low peak voltage of 0.9 mV with cycles. By adjusting the number of CV cycles, we investigated how electrochemical performance, surface roughness, and effective area of the electrodes were affected. The main findings include:

(1)**Microscopy and SEM Results** showed that the thickness of the PEDOT: PSS coating increased consistently with more CV cycles, while the deposition remained smooth and uniform across all electrode sizes. Low voltage ranges prevented defects and irregularities in the coating.

(2) **Surface Roughness** analysis revealed that while the first CV cycle significantly increased surface roughness, additional cycles did not contribute further to roughness. This indicates that a smooth surface can be maintained even with multiple cycles, which was consistent across all electrode sizes.

(3) **Effective Area** measurements showed that increasing the number of CV cycles enhanced the effective area of the electrodes. This increased surface area was important for reducing impedance and improving charge transfer capabilities, even when surface roughness remained unchanged.

(4) **Electrochemical Properties** demonstrated a significant reduction in impedance after the first CV cycle across all electrode sizes. Smaller electrodes (10 μm, 20 μm) saw a greater reduction in impedance with the second cycle, but further cycles did not lower impedance further. The 20 μm electrodes achieved similar impedance values to larger electrodes (50 μm, 100 μm) after two CV cycles, making them suitable for neural recordings. However, fabricating flexible electrodes at the 10 μm size presented greater challenges.

Overall, the study identified two CV cycles as optimal for balancing surface modification and electrochemical performance.

3.2. Development of Flexible Dual-Sided Meas

3.2.1 Microfabrication Results of Flexible Dual-Sided Meas

The microscope images in **Fig. 2.12** showcase a prototype of the 8-channel single-sided MEA and its dual-sided counterparts after folding and thermal bonding, respectively. In **Fig. 2.12A,** the two parylene layers did not adhere well to each other after being folded, as evidenced by the presence of a rainbow sign (Newton' ring)[208]. The disappearance of the rainbow sign after thermal annealing and bonding suggests that the bonding process effectively enhanced the adhesion between the two parylene layers. To facilitate interconnects to external recording instruments, the resulting dual-sided MEAs were assembled and bonded onto a customized printed circuit board

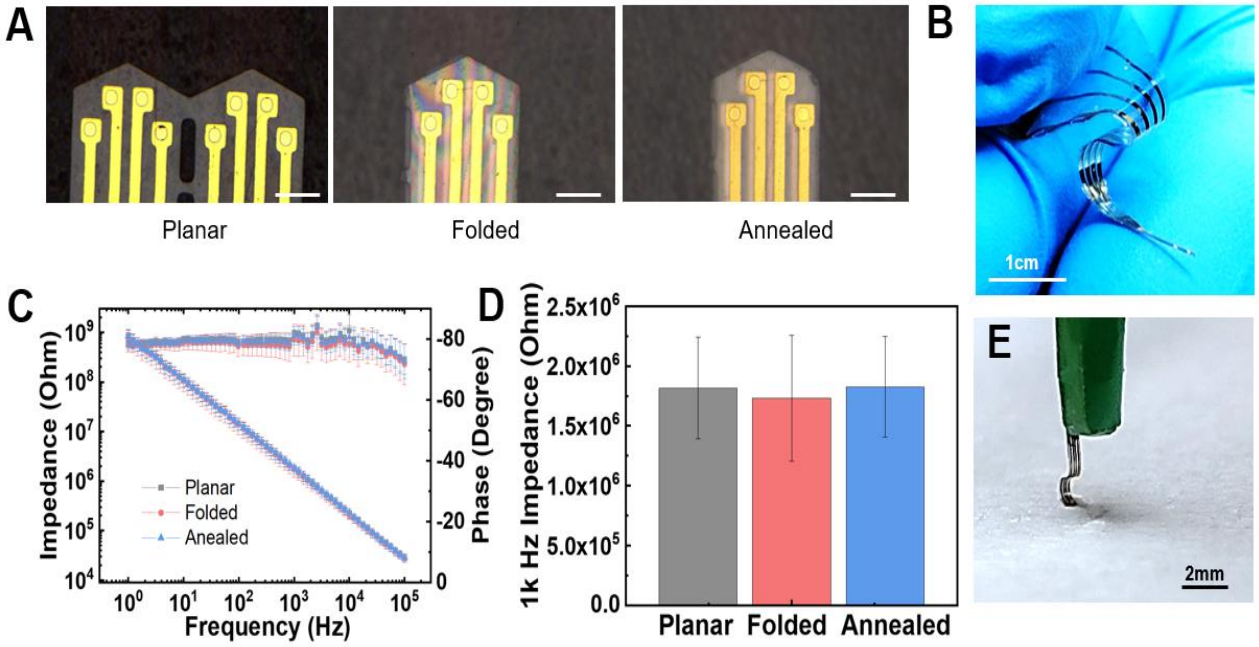

***Figure 2.12. Images of the MEAs**. **A.** Optical images Microscope pictures of the MEAs in planar, folded, and annealed status. Scale bar: 100 μm. **B.** The flexible tip of an assembled MEA. **C.** Electrical impedance spectroscopy of the microelectrodes during the fabrication processes(n=6). **D.** 1k impedance of the electrodes in different status. And microscopic images(**E**) of a bending tip of the MEA.*

(PCB) using conductive silver paste. Contact pads with central holes were uniquely designed to ensure robust electrical contact between silver paste and PCB pads from both sides of the array.

Broadband electrochemical impedances of the microelectrodes were measured after each fabrication process, including releasing, folding, and thermal annealing/bonding (**Fig. 2.12C**). The electrochemical characteristics of the electrodes remain stable throughout various fabrication processes, indicating that these processes did not compromise the electrochemical properties of the microelectrodes. The final assembled device had a flexible tip on the MEA region (**Fig. 2.12E**), while the PCB-enforced backbone provides ease of device handling during insertion and recording experiments.

3.2.2 Effect of PEDOT: PSS Coating on Performance of MEA Electrodes

To enhance the electrochemical conductivity of the electrodes, PEDOT:PSS was deposited on gold electrodes using CV in a three-electrode configuration. We used the parameters that we learned from Section 2.1. ("Explore the optimize surface modification strategy of PEDOT: PSS deposition on gold electrodes in different sizes"). CV was performed with voltage ranging from -0.7 V to 0.9 V vs. the Ag/AgCl RE and a scan rate of 10 mV/s. The results of the electrodeposition of

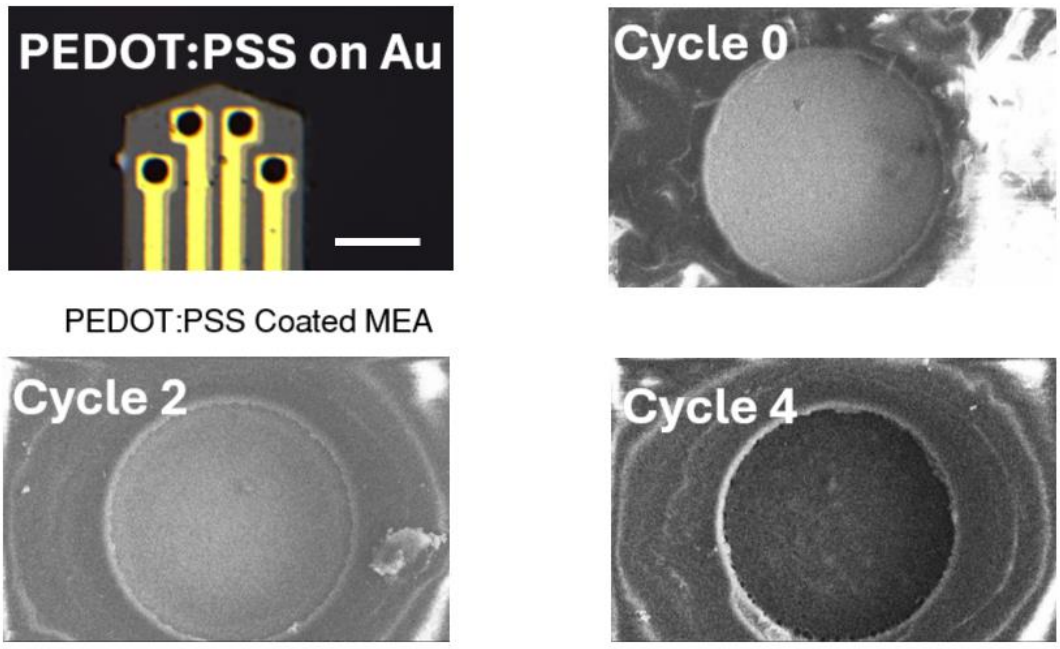

Figure 2.13. SEM images of the electrodes in varying sizes under different coating cycles.

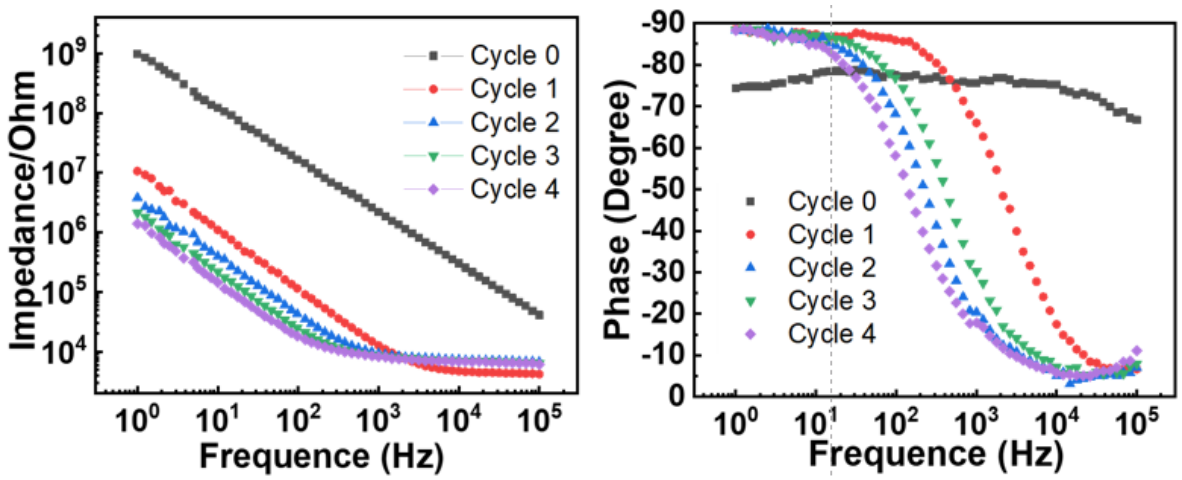

Figure 2.14. EIS results of electrodes with a 20 µm diameter subjected to varying coating.

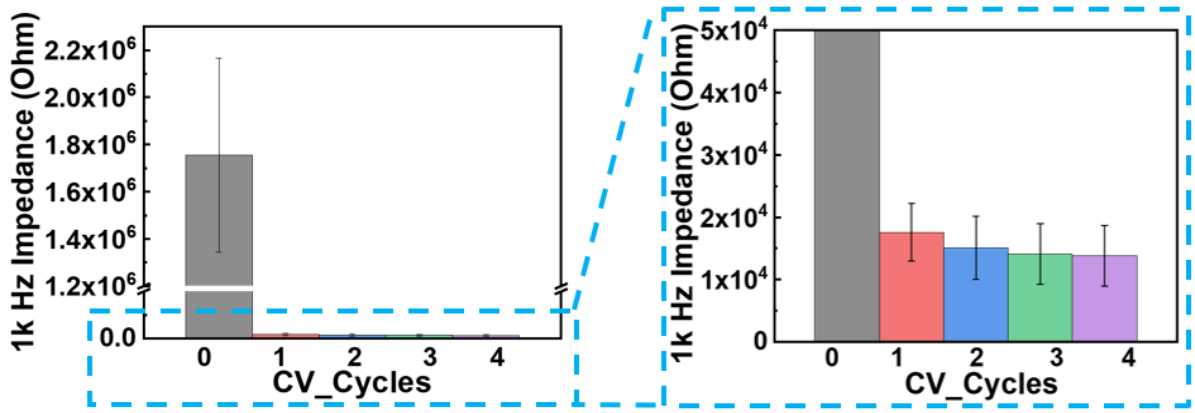

Figure 2.15. 1 kHz impedance of electrodes with a 20 µm diameter subjected to varying.

PEDOT:PSS on the electrodes of MEAs are consistent with previous studies in Section 2.1., as shown in **Fig.** 2.13. The electrodeposition of PEDOT:PSS provides smooth surface on the gold electrodes of the MEAs, as shown in **Fig. 2.14**. After a single cycle of CV coating with PEDOT: PSS, the impedance at 1 kHz decreased significantly by two orders of magnitude. A second cycle of CV coating further decreased the impedance, with a greater reduction observed for smaller electrodes. However, a further increase in the number of CV cycles to three or four did not lead to significant additional reduction in impedance (**As shown in Fig. 2.15**). The impedance at 1 kHz for

the 20 µm electrodes converged to a range between 10^3 and 10^4 ohms, suitable for neurophysiological recording. **Fig. 2. 16** shows the surface roughness of the electrodes with and without the PEDOT:PSS coating. The results indicate that the PEDOT:PSS coating increased the surface roughness of the electrodes; however, two or more cycles of coating didn't further increase the surface roughness.

3.2.3. Mechanical Properties

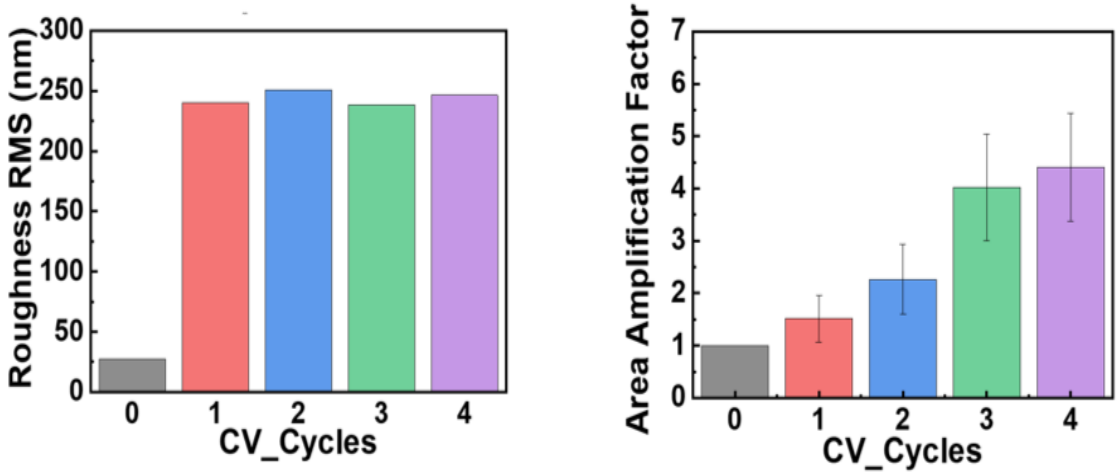

Figure 2.16. Surface roughness and effective area change of electrodes with a 20 µm diameter subjected to varying coating cycles.

To investigate the device's mechanical properties for insertion, the MEAs were inserted into a brain tissue phantom, 0.6%(w/v) agarose, and the electrochemical impedance of the electrodes were evaluated before and after undergoing 15 repeated insertions. The results indicated that the flexible dual-sided MEAs could be directly inserted into the brain tissue phantom without any mechanical reinforcement, as shown in **Fig. 2.17**. The electrodes maintained their electrochemical performance after multiple insertions , demonstrating the device's robustness and stability under repeated insertion conditions. **Fig. 2.18.** demonstrates the successful insertion of an 8-channel dual-sided MEA into the right antennal lobe of a living locust. The electrodes exhibited consistent

electrochemical impedance before and after bending, affirming the mechanical flexibility and stability of the device.

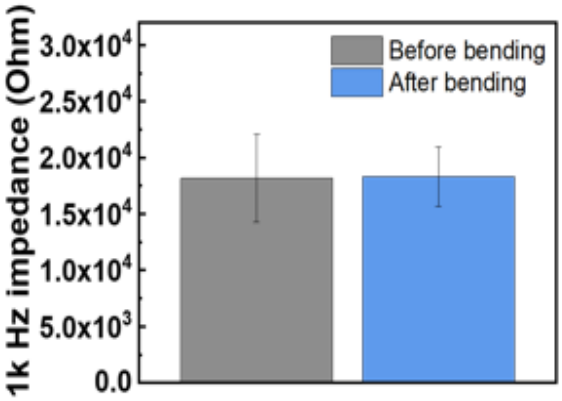

Figure 2.17. 1 kHz impedance of electrodes before and after bending.

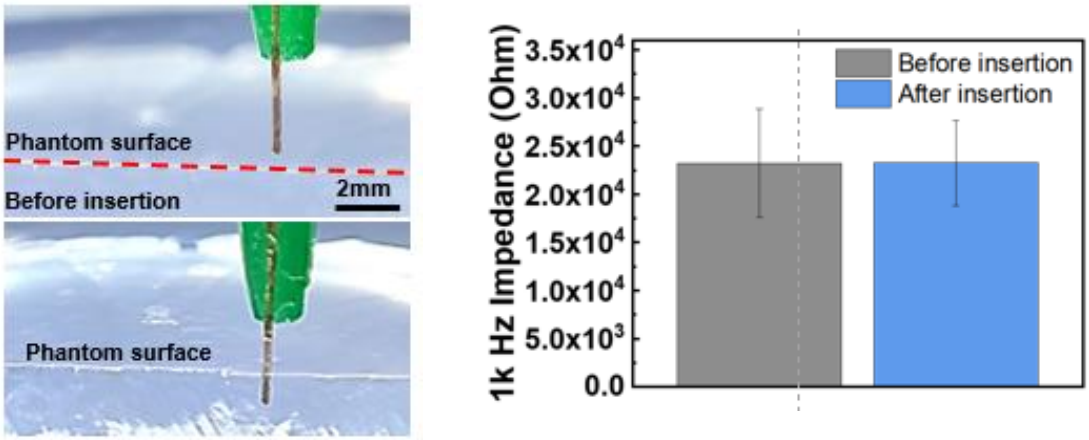

Figure 2.18. SEM images of the electrodes in varying sizes under different coating cycles.

3.2.4. Stability in Soaking Test

As shown in **Fig. 2.19**, the impedance of the electrodes remained relatively stable over the 7-day soaking period in PBS at room temperature, with no significant deviations observed in either the 2-cycle or 4-cycle PEDOT: PSS electrodes. The impedance at 1 kHz for both conditions remained within the range of 1.5 × 10^4 to 2.0 × 10^4 ohms, with slight variations that were within the measurement error. These results indicate that both the 2-cycle and 4-cycle PEDOT: PSS coated

electrodes effectively maintained its integrity and the electrodes continued to perform reliably after prolonged exposure to PBS. This suggests that the MEAs are well-suited for insect *in vivo* applications, where they may be exposed to physiological fluids over extended durations. The robustness of the MEAs in these conditions is critical for ensuring consistent performance in neural recordings and biosensing.

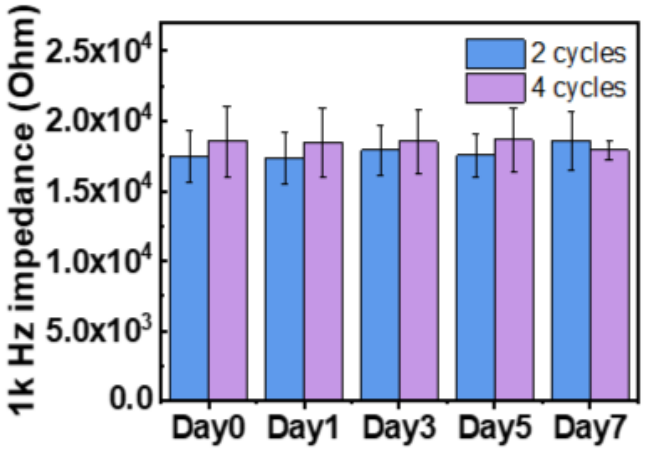

Figure 2.19. SEM images of the electrodes in varying sizes under different coating cycles.

3.2.5. Bench-Top Recording Properties

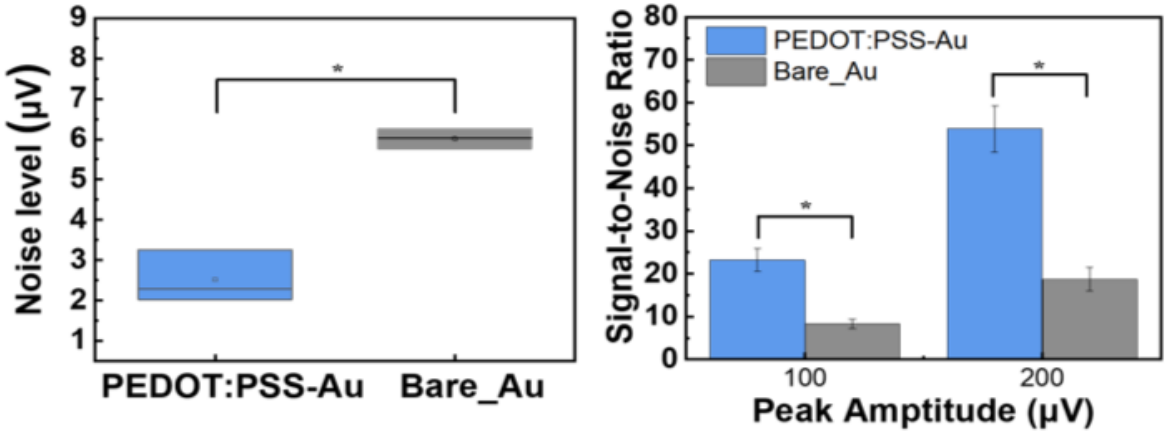

Figure 2.20. SEM images of the electrodes in varying sizes under different coating.

The noise levels of the microelectrodes with or without PEDOT: PSS coating were evaluated and quantified using simulated biosignals generated by a function generator (referred to the setup

in **Fig. 2.6**). The basic noise level was 6.01 ± 0.24 μV for bare gold electrodes, which decreased to 2.52 ± 0.65 μV for 2-cycle PEDOT:PSS coated electrodes (**Fig. 2.20**). The SNR increased from 8.32 ± 0.24 to 23.22 ± 2.66 when the peak voltage of the signal applied was 100 μV, and from 18.77 ± 2.80 to 53.86 ± 5.44 when the peak voltage of the signal applied was 200 μV (**Fig. 2.20**). Compared to pure gold electrodes, the PEDOT: PSS coated electrodes exhibit significantly lower base noise level and higher SNR because of their lower impedance. Maintaining low noise levels during recording is crucial to detect action potentials from background noise, and to further isolate single neuron activities.

4. DISCUSSION

4.1 Optimized PEDOT Coating strategy

In this study, we optimized the strategies on electrodeposition of PEDOT on the gold electrodes of the MEAs using cyclic voltammetry (CV). We systematically investigated the effects of varying the number of CV cycles on the surface morphology, roughness, effective area, and electrochemical properties of the electrodes. The use of a low voltage range during CV deposition (-0.7V to 0.9V) proved essential in avoiding damage to the gold electrodes, which is a common concern when using higher voltage ranges in other electropolymerization studies. Electropolymerized PEDOT: PSS has been extensively utilized in the enhancement of microelectrode performance [86, 209, 210]. Compared to other electropolymerization modes, such as potentiostatic (PS), and galvanostatic (GS), CV deposition yields a more uniform coating [209], which is beneficial for inversive MEAs to minimum the direct damage to the tissue [209, 211]. CV deposition of PEDOT:PSS typically requires multiple cycles to achieve excellent stability and high charge injection capacity of electrodes for chronic neural interfaces [212]. However, the literature seldom reports on the nuanced effects of varying CV cycles on the electropolymerization of PEDOT:PSS on gold

electrodes. Moreover, the peak voltage of CV deposition varies between 0.9 V and 1.2 V across different reported studies, which exceeds the water window potential limits of gold (−0.8 V to 0.8 V)[213]. In this study, we systematically studied the effect of CV cycles on the PEDOT:PSS performance including surface roughness, effective surface area, and electrochemical properties. We strategically employed a CV protocol operating within a low voltage range of -0.7 V to 0.9 V to mitigate potential damage to the gold electrodes that could arise from excessive voltage application.

We observed that the effective area of PEDOT: PSS increased with the increase of CV cycles and the surface roughness increased after PEDOT:PSS deposited on the gold surface, which is similar to previous studies [209]. The increase in surface roughness is a critical factor, as it directly influences the electrochemical properties of the electrodes by expanding their effective surface area. This is confirmed by the magnitude of electrode impedance, which drops dramatically after PEDOT:PSS coating. The first CV cycle significantly increased surface roughness, but additional cycles did not contribute further to roughness. In the first CV cycle, nucleation occurs, where PEDOT:PSS begins to deposit onto the gold electrode surface. During this initial phase, the polymer forms a foundation layer, filling microscopic imperfections and contributing to the overall increase in surface roughness. This process is known as the "nucleation and growth" mechanism[214], where the first layer introduces uneven clusters and aggregates, causing the surface to roughen. With additional CV cycles, the deposition shifts from nucleation to growth and thickening of existing layers[214, 215]. In this study, additional CV cycles continues to cause polymer accumulation, but tends to maintain the roughness introduced during the initial cycle, rather than exacerbating it. Once the initial irregularities are covered, further material deposition tends to conform to the already established layer, filling in the smaller gaps and depressions rather than creating new surface peaks,

which maintains a smoother surface overall. In previous study, PEDOT:PSS has been reported that film cracking appeared after certain time during potentiostatic deposition[215]. Our result indicates that a smooth surface can be maintained even with multiple cycles, which was consistent across all electrode sizes. This is in line with our expectations, as we need a sufficiently smooth surface to reduce direct implantation damage, which is crucial for delicate insect brain tissue.

After two CV cycles, the amount of PEDOT: PSS deposited on the surface of the gold electrode continuously increases, which further increases the effective area of the electrode, but shows no significant reduction in the electrochemical impedance. This indicates that the efficiency of electron transport in the two cyclically deposited PEDOT: PSS-Au electrodes has become saturated. Our findings are consistent with those of the previous study by Mousavi et al.[215], wherein they observe dramatic decrease in the impedance magnitude with small variations between the numbers of cycles. In our series study on electrodes that with diameter <= 100 μm, the reduction in impedance after the first CV cycle, particularly for smaller electrodes (10 μm and 20 μm), was dramatic, with the 1 kHz impedance dropping by two orders of magnitude. This reduction is crucial for neural recordings, as lower impedance translates to better signal quality and improved SNR. The smaller electrodes, such as the 10 μm and 20 μm variants, benefit the most from PEDOT coating, making them suitable for high-resolution neural recordings in compact neural regions like the insect brain. The two-cycle CV process not only reduced the impedance to a suitable range for electrophysiological recordings but also maintained surface smoothness, which is important for minimizing potential tissue damage during long-term implantation. This finding is significant, as it indicates that two cycles of PEDOT deposition provide the optimal balance between surface modification and electrochemical enhancement.

4.2 Folding-Annealing Strategies for Flexible HDMEAs Fabrication

We developed a fold-annealing method that enables the creation of flexible, high-density, dual-sided MEAs in a cost-efficient manner. The dual-sided array allows neural recording from both sides of the MEA, with improved electrode density within a compact footprint. Our microfabrication technique was able to achieve unprecedented electrode densities of 463, 687, and 766 channels/mm², with one side center-to-center space from 50-70 μm (one side), 25-35μm in average within one probe of dual sides. These densities are significantly higher than those reported in existing flexible devices[72, 75, 216, 217], enabling more detailed and accurate neural recordings. The microelectrodes maintain their electrochemical integrity throughout various fabrication processes including folding, annealing, and bonding, ensuring the consistency of device fabrication. Moreover, we validated the mechanical and electrochemical stability of the MEAs through insertion, bending and 7-day soaking tests, demonstrating the promise of the MEAs for short terms stable recording in our target applications. The reliable fabrication and application of these flexible dual-sided MEAs mark a pivotal advancement in neuroscientific research tools. The novel folding-annealing technique introduced in this study not only allowed us to significantly increase the channel density on a flexible substrate without expanding the device footprint, but also enable the sual-sided functioning of the MEAs. It also preserves the MEAs with mechanical flexibility, which is crucial for chronic *in vivo* applications. The manufacturing techniques presented in this study are compatible with conventional semiconductor manufacturing techniques and versatile enough to be scaled for wider applications, paving the way for the creation of robust flexible MEAs with higher spatial resolution and channel counts.

Looking forward, the methodologies and findings presented in this study open new avenues for the application of flexible, high-density MEAs in neuroscience. The successful demonstration of

dual-sided MEAs tailored for insect models can be further expanded to other compact neural systems, offering unprecedented insights into neural circuitry and function. Additionally, the scalability of the folding-annealing technique suggests the potential for wider adoption in various biomedical applications, including human neural interface technologies and bioelectronic sensing platforms.

Future research will focus on exploring the potential applications of these MEAs in the detection of VOCs related to disease diagnostics, such as lung cancer biomarker detection. The ability of these MEAs to interface with insect neural systems, such as the locust antennal lobe, opens up new possibilities for developing biohybrid systems that leverage the natural sensitivity of insect olfactory systems for chemical detection.

5. SUMMARY

This study presents significant advancements in the development of high-density, flexible dual-sided MEAs optimized for compact neural regions like the insect brain. Through the careful optimization of PEDOT: PSS electrodeposition using CV, we demonstrated that a low voltage range (-0.7 V to 0.9 V) and two CV cycles are sufficient to enhance the electrochemical properties of the electrodes while maintaining surface smoothness. This balance between increased surface area and reduced impedance is critical for achieving high-quality neural recordings, particularly in high-resolution applications. Smaller electrodes, such as the 10 μm and 20 μm variants, greatly benefited from this optimized coating strategy, making them highly suitable for detailed neural recordings in small brain regions.

The innovative folding-annealing technique we employed effectively doubles the channel density without increasing the physical footprint of the MEAs, preserving both mechanical flexibility and structural integrity. This method not only ensures robust bonding between parylene

layers but also maintains the electrochemical performance of the electrodes through various fabrication and handling processes. The mechanical stability of the MEAs was validated through rigorous testing, including insertion into brain tissue phantoms, bending, and prolonged soaking in physiological conditions. These tests confirmed the durability and functionality of the MEAs, highlighting their potential for long-term applications in both research and clinical settings.

CHAPTER 3: BIOSENSING PLATFORM AND NEUROPHYSIOLOGICAL RECORDING USING LOCUST SYSTEMS

1. INTRODUCTION

The capacity to identify lung cancer through the analysis of volatile organic compounds (VOCs) found in breath and other biological fluids could significantly enhance the availability of early cancer diagnostics across broad populations, thereby facilitating timely treatments and improving patient prognoses. Currently the most promising approach for lung cancer screening is with low dose computed tomography (LCDT) in high-risk populations which have shown to provide statistically significant mortality reduction in patients[218]. This approach, however, relies on risk modeling methodology to select high-risk populations and to minimize the potential damages to radiation exposure to a broader population [218, 219]. A more accessible diagnostic tool relying on a VOC-based analysis method could circumvent these approaches due to its intrinsic noninvasiveness and lack of harmful exposures. VOCs from the human body are emitted from a variety of sources including breath, sweat, skin, urine, feces, and vaginal secretions as a result of metabolic pathways [220-229]. Disease and pathological processes can affect the body's VOC signature by the production of novel VOCs or by changing the ratio of existing VOCs [220]. These VOCs have been validated for their association with cancer in various *in vitro* and *in vivo* studies including lung, breast, leukemia, gastric, and prostate cancer [221, 222, 230-248]. However, The exist methods have their own difficulties in incorporating VOC analysis in clinical diagnostics (as shown in **Table 3.1**). GC-MS and other mass spectrometry-based techniques (e.g., SIFT-MS, PTR-MS, GC-IMS) which require time and labor-intensive workflows for sample preparation, analysis and require technical expertise [227-229, 239, 240, 243, 249-272]. Electronic noses are simpler to operate and more portable in comparison to GC-MS and have been used to classify multiple types

of cancer including lung, prostate and head and neck [273-276], however e-noses reliability suffers due to senor drift and can be sensitive to environmental conditions such as temperature and humidity [266-270, 272, 277]. The locust olfactory system offers a unique advantage in detecting VOCs associated with lung cancer and has been shown to detect human oral cancer in a previously reported study [165]. By tapping into the locust's acute sense of smell, we are able to take a forward engineering approach utilizing the inherent chemosensory array of the antennae and biological odor coding schemes of the antennal lobe for VOC detection and differentiation. This in combination with flexible dual-sided MEAs and computational techniques presents a new platform for a lung cancer diagnostic tool.

Biological olfaction has shown remarkable sensitivity in detecting low concentrations of VOCs, ranging from parts per billion (ppb) to parts per trillion (ppt) range, and minute changes in the compositions of gas mixtures [174-180]. In particular, the locust olfactory system offers a unique model for lung cancer VOC detection. In the locust olfactory system, VOCs are first detected in the antennae by olfactory receptor neurons (ORNs), which transform the chemical stimuli into electrical signals and transmit the signals downstream to the antennal lobe (AL), where the signal is processed by intricate network of excitatory projection neurons (PNs) and inhibitory local neurons (LNs) [181, 182]. In the AL, the spatiotemporal population response from the PNs gives rise to odor-specific neural codes which are believed to determine odor identity, intensity, and time course [179, 180, 278]. Leveraging insects' natural ability to discern gas mixtures at low concentrations across changing environmental conditions, we proposed to use the locust olfactory system as a biological sensor for chemical detection, particularly for VOCs associated with lung cancer. To effectively implement this scheme, efficient neural activity recording tools and robust analysis methods are essential. Tetrodes are commonly used in insect neural recordings [184, 185],

but are limited by their design with only four widely spaced electrodes, rendering them relatively inefficient for detailed neural signals. MEAs present a more promising alternative [39, 166, 186, 187]. Yet, in insect brain neurology, there is a growing need for flexible, multi-channel, or even high-density MEAs (HDMEAs). However, current research in this area still faces several gaps. First, the majority of existing HDMEAs are tailored for humans, rodents, or large animals, with only a few designed with the unique requirements of insects in mind. However, the brain of a locust is much smaller than a rat's hippocampus, with its antennal lobe having an effective area of about 500 μm in diameter. Even the most advanced HDMEAs available today, such as silicon-based Neuropixel 2.0 [186, 188] that have a distance of 175 μm from electrode to tip, are too large for effective use in such small brain regions. Second, high spatial resolution MEAs are necessary due to the inefficiency of using conventional MEAs with electrode sizes larger than 20 μm and/or distances exceeding 100 μm, given the small size of the locust brain and its limited dimensions. The high-resolution multichannel MEAs provides benefits in neural voltage recordings with high spatial and temporal detail, offering a holistic perspective on the neural dynamics. Finally, there is a necessity for flexible MEAs in the realm of insect biosensing. Although rigid MEAs offer precise measurements and reliable data acquisition [42, 173, 189, 190], flexible MEAs offer a more intimate and sustained interface with tissues, thereby enhancing signal quality and providing precise spatiotemporal scale of neuronal activity [1, 113, 166, 191-195].

In the previous chapter, we presented the development of a flexible dual-sided microelectrode array (MEA) using a unique folding-bonding technique on a parylene C substrate. This approach successfully transformed a polymer-based planar single metal layer into a dual-sided structure[1].In this chapter, we focus on the application of these flexible MEAs for reliable neurophysiological recordings of lung cancer-related activities from the locust antennal lobe. Our

goal is to establish a biosensing platform by integrating flexible MEAs with the locust olfactory system. As a proof-of-concept, we successfully recorded in vivo extracellular neural responses to lung cancer VOC biomarkers from projection neurons (PNs) in the locust antennal lobe using the dual-sided MEAs. We then analyzed population neural responses using dimensionality reduction techniques. Additionally, high-dimensional computational methods were employed to classify unknown lung cancer VOCs, achieving high classification accuracy.

By merging the advanced dual-sided MEAs and computational techniques with the biological sensitivity of insect olfaction, this bioelectronic sensing method shows great potential for robust and efficient identification and classification of lung cancer biomarkers.

2. METHODS

2.1 Insect Surgery and MEA Insertion

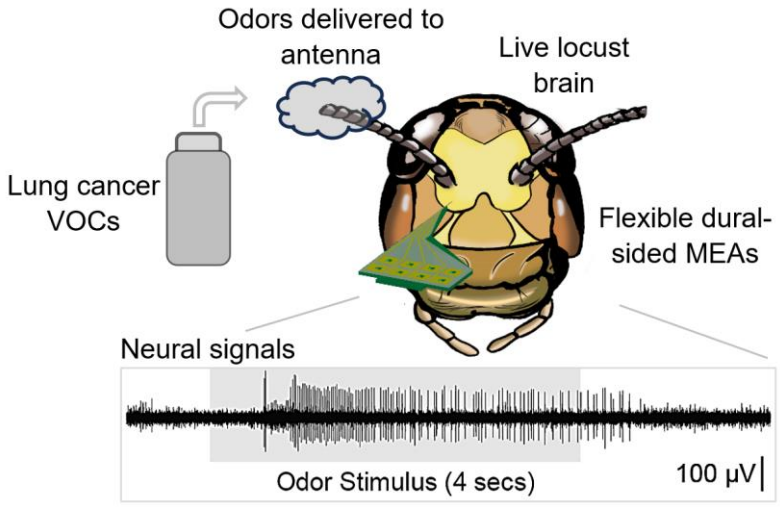

Figure 3.1. Schematic of application setup, *where VOCs are delivered to the chemosensory array (antenna) and neural responses are recorded from the antennal lobe region of the locust brain using a flexible dual-sided MEA. A representative voltage trace is shown displaying a 4 second stimulus and VOC-evoked response.*

All *in vivo* experiments were performed on post-fifth instar locust (*Schistocerca americana*) of either sex raised in a crowded colony, following the surgical procedures and setup for insect brain recordings as described by Farnum et al.[165]. Briefly, the locust's head was isolated in a

batik wax bowl filled with a room-temperature, physiologically balanced saline solution. Then the exoskeleton and glandular tissue were removed to expose the locust brain. After treating the antennal lobes with protease and removing the fine sheath covering the lobes, the MEA was inserted 100 μm deep into the lobes on a Faraday cage-isolated bench for neural recording, with or without odor stimulation. The neural signals were recorded using an Intan preamplifier (C3334 RHD 32 channel headstage, Intan Technologies) and Intan recording board (C3100 RHD USB interface board, Intan Technologies) at a sampling rate of 20 kHz. For odor stimulation, a precision olfactometer (Aurora Scientific, 220A) was employed to deliver a controlled blend of clean air and odor to the locust's antenna for 4 secs, followed by an immediate switch back to clean air, with a vacuum funnel behind the antennae for rapid odorant removal. This procedure was repeated five times at 60-sec intervals for each odor to prevent olfactory fatigue and ensure consistent neuronal response.

2.2. Odor Stimulation

A precision olfactometer (Aurora Scientific, 220A) facilitated controlled odor delivery. Initially, 200 sccm of clean air was channeled through both the fresh air and dilution lines, with the stimulus flow line's end placed 2-3 cm from the locust's antennal tip. Before odor introduction, 40% of the dilution air was rerouted to blend with the odor stream, ensuring thorough mixing before reaching the locust. At stimulus onset, a valve switch directed the odor-air mixture to the antenna, maintaining a constant flow for 4 seconds, followed by a swift return to clean air. A vacuum funnel behind the antennae expedited odorant removal. Stimuli were administered five times in a pseudorandom sequence, with a 1-minute interval to prevent olfactory fatigue and ensure consistent neuronal response.

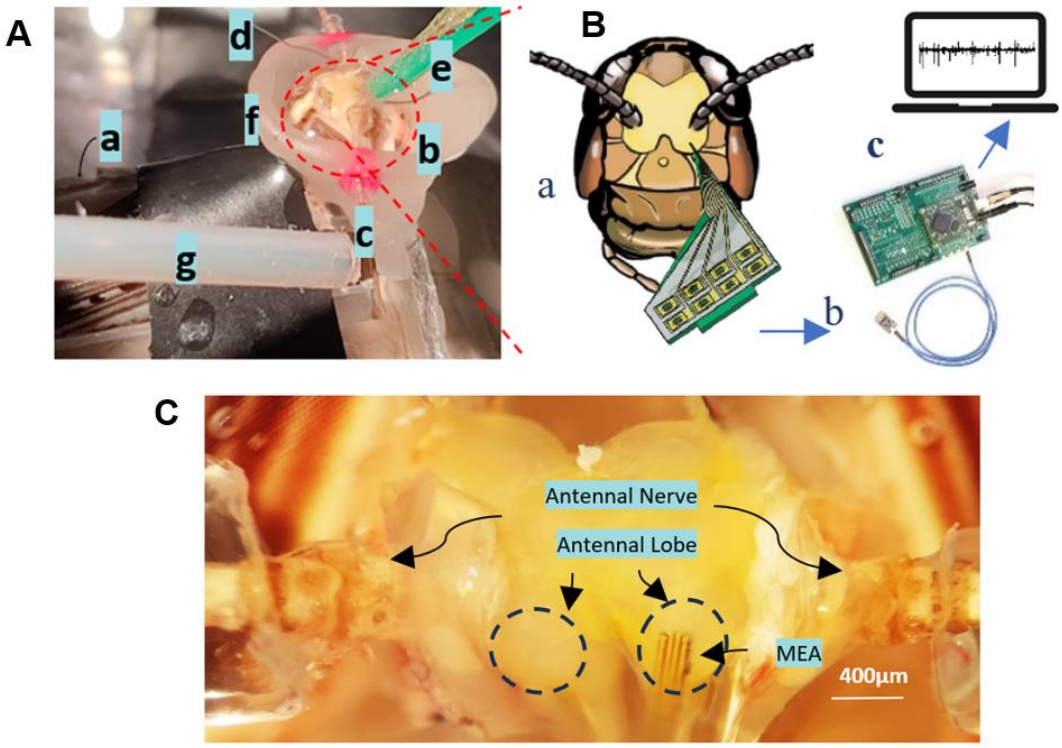

Figure 3.2. Application of dual-sided MEAs for in vivo neural recording and odor response detection. *(**A**) In vivo experiment setup. (a) body of a locust, (b) brain of the locust, (c) antenna, (d) reference wire, (e) MEA, (f) wax bowl, (g) odor deliver tube. (**B**) Schematic of the MEA inserted in the locust brain (a), linked to the Intan headstage and RHD interface board(b) to a computer(c).(**C**) An implanted MEA in the locust olfactory brain, indicating the insertion position (within the olfactory brain, shown in black dash circle).*

2.3 Lung Cancer Biomarkers Preparation

To investigate neural responses to lung cancer biomarkers, we used a set of specific odorants, including nonanal, hexanal, pentanal, and propylbenzene (all from Sigma-Aldrich). Each of these odors were diluted in 10 mL of mineral oil (Millipore Sigma, St. Louis, MO, USA) at 1% vol/vol concentration, and pure mineral oil was used as a control.

2.4 Odor Delivery and Odor Stimulation

Odor stimulation was performed following our pre-established methodology[165]. Briefly, a commercial olfactometer (Aurora Scientific, 220A) was used for controlled odor stimulus delivery. Initially at the beginning of each trial, 200 standard cubic centimeters per minute (sccm) of zero

contaminant air was delivered through a 1/16-inch diameter PTFE flow line to the locust antenna denoted the stimulus flow line. The end of the stimulus flow line was placed approximately 2-3 cm from the most distal antennal segment. An additional 200 sccm of zero contaminant air was passed through a separate flow line to the exhaust denoted the dilution flow line. Five seconds before odor stimulus delivery, 40% (80 sccm) of the dilution flow line was redirected through the odor flow line directly upstream of the odorant vials. The dilution flow line and the odor flow line joined downstream of the odorant vials. This allowed the for the 80 sccm odor flow to mix with the 120 sccm of the dilution flow line's clean air. The air-volatiles mixture primed the line with volatiles up to the final valve, where the combined odor + dilution flow was delivered to the exhaust. Upon stimulus onset, the final valve redirected the clean air flow to the exhaust and the odor + dilution flow to the locust antenna via the stimulus flow line. After 4s constant flow and odor stimulus delivery, the final valve redirected the clean air flow back to the locust antenna via the stimulus flow line and the odor + dilution flow back to the exhaust. One second after odor stimulus offset, the 80 sccm flowing through the odor line was redirected through the dilution flow line, alleviating potential headspace gas depletion during the odor delivery. This protocol was designed to keep a constant flow rate through the stimulus flow line, thereby eliminating any potentially confounding neuronal responses due to changes in air pressure via mechanosensory detection. A 6-inch diameter funnel pulling a slight vacuum was positioned immediately behind the locust during odor stimulus delivery to ensure rapid removal of odorants. Each 4 second-duration odor stimulus was repeated 5 times with an interstimulus interval of 60 seconds. The order of the stimuli was pseudorandomized for each experiment.

2.5. Insect Surgery and Signal Acquisition

Locust surgery was performed according to previously published methods [177, 279]. Briefly, locusts were immobilized onto a surgical platform and antennae were stabilized. A batik wax bowl around the head was constructed to isolate the region and then filled with a room temperature, physiologically balanced locust saline solution. The removal of the exoskeleton between the antennae was performed and glandular tissue was removed until the brain was fully visible. Treatment with protease was done to desheath the antennal lobes. Following surgery, the animals were placed in a Faraday cage isolated bench and a silver-chloride ground wire was placed in the saline bath. Voltage signals from antennal lobe projection neurons were recorded by inserting the multichannel MEA into the antennal lobe (**Fig. 3.2**). Voltage signals were sampled at 20 kHz and then digitized using an Intan pre-amplifier board (C3334 RHD 32-channel headstage). The digitized signals were transmitted to the Intan recording controller (C3100 RHD USB interface board) before being visualized and stored using the Intan graphical user interface and LabView data acquisition system. A total of 12 antennal lobe neural recordings were conducted and 69 projection neurons were spike-sorted. Every antennal lobe projection neuron recording was conducted using the same VOC panel and each VOC delivery to the antenna was repeated 5 times with a 60 s inter-stimulus-interval.

2.6. Data Analysis

2.6.1 Spike Sorting

All neural data was imported into MATLAB after high pass filtering using a 300Hz Butterworth filter to eliminate frequencies below 300 Hz. The data was analyzed by custom-written codes in MATLAB R2023b. All data was processed with Igor Pro for spike sorting analysis using previously described methods [280] or an offline spike sorting software ROSS [281]. Spiking events were

identified using a detection threshold between 2.5 and 3.5 standard deviation (SD) of baseline fluctuations. Individual projection neurons were identified if they passed the following criteria: cluster separation > 5 SD, inter-spike intervals (ISI) ≤ 10%, and spike waveform variance ≤ 10%.

2.6.2 Dimensionality Reduction Analysis

We performed two methods of dimensionality reduction – Principal Component Analysis (PCA) and Linear Discriminant Analysis (LDA). In PCA, we binned baseline subtracted, spike sorted neural signals in 50 ms non-overlapping time bins and averaged across trials (n = 5, each VOC was repeated 5 times with a 60 s inter-stimulus interval). The baseline response was calculated for each neuron by averaging the firing rate over the 2 second time window prior to odor stimulus onset across trials. The spike sorted neurons were pooled across electrophysiological experiments. For example, in **Fig. 3.5a**, spike sorted and binned responses of all recorded neurons (69 total) were combined to generate a neuron number (n =69) x time bins (t = 30, number of 50 ms bins between 0.25 – 1.75 s) matrix, where each element in the matrix corresponds to the spike count of one neuron in one 50 ms time bin. Similar neural population time-series data matrices were generated for each odor stimulus. PCA dimensionality reduction analysis was performed on the time-series data involving all odor resources respectively (**Fig. 3.5a**). The consequent high-dimensional vector in each time bin was projected along the eigenvectors of the covariance matrix. Only the three dimensions with the highest eigenvalues were used for visualization and data points in subsequent time bins were connected to produce low-dimensional neural trajectories. The trajectories were smoothed using a third order IIR Butterworth filter (Half Power Frequency = 0.15). Lastly, all trajectories were shifted to begin at the origin to analyze stimulus-specific response dynamics and trajectory divergence.

For LDA, the same neural population time-series data matrix was used. Here, we maximized the separation between interclass distances while minimizing the within class distances. For visualization purposes, time bins were plotted as unique points in this transformed LDA space and stimulus-specific VOC clusters became easily noticeable (**Fig. 3.5b**). All dimensionality reduction analyses were accomplished using custom written MATLAB (R2023b) codes.

2.6.3 Quantitative Classification Analysis: Leave-One-Trial-Out

To classify the individual lung cancer biomarkers, we performed a leave-one-trial-out analysis. The spike sorted data was binned into 50 ms bins to create a three-dimensional matrix (69 neurons x 5 trials x *n* time bins). For example, **Fig. 3.5c** and **d** uses 30-time bins for the time window between 0.25 – 1.75 s after stimulus onset (**Fig. 3.7**), which corresponds to the phase of the odor-evoked neural activity that is most discriminatory termed the transient phase. For leave-one-trial-out (LOTO) analysis, four trials (out of five) were averaged together to form a training template, while the fifth trial, the left-out trial, was used as the testing template. This was repeated for all odors to create 5 training templates and 5 testing templates and each time bin from these templates were considered as points in high-dimensional space. In a bin-wise matched manner, the Euclidean distance between the testing template time bins and the training template time bins were calculated and the testing template time bins were assigned based on the shortest Euclidean distance. We repeated this for each of the five trials, each time leaving out a different trial for the testing template and using the remaining four trials to create the training template. The results for type of analysis are summarized with a confusion matrix (**Fig. 3.5c**). This type of analysis is termed a bin-wise classification. We did a further analysis by calculating the mode for each testing template across the *n* time bins for the time window of interest. The mode was used to classify the entire trial in a winner-take-all approach and the results are summarized in **Fig. 3.5d** and **6c**. This analysis is termed

a trial-wise classification. A fully diagonal matrix indicates 100% classification accuracy with any cells filled outside of this diagonal indicating misclassifications. All quantitative classification analysis was accomplished using custom written MATLAB (R2023b) codes.

3. RESULT

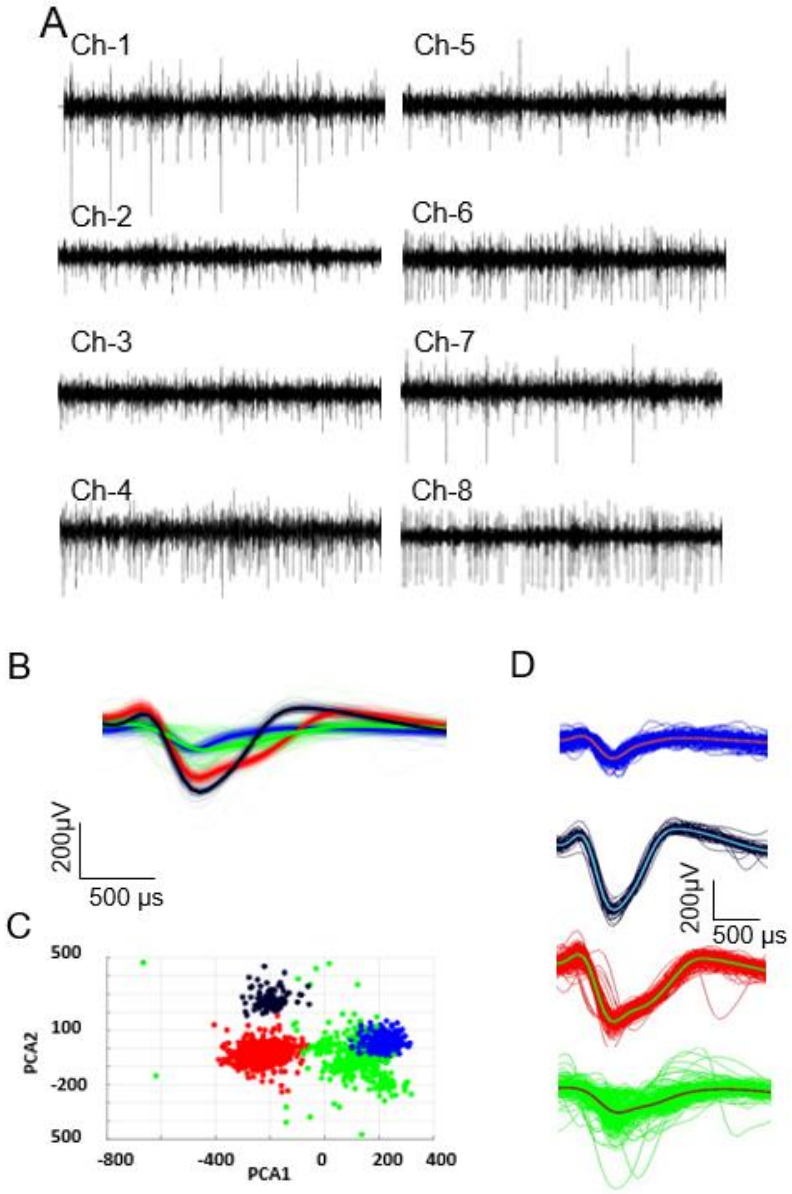

Figure 3.3. Recording performance of the electrodes. *(**A**) the raw neural voltage signals recorded concurrently from all channels using the 8-channel MEA, following a 300 Hz high-pass filter application. The spikes analyzed from each channel's signal(**B**), along with (**C**) example of Principal Component Analysis (PCA) results. (D) The corresponding spike-sorted waveforms (**F**) of the neural signals.*

3.1 In vivo Recording Performance of The Flexible Dual-Sided MEAs from Insect Brain

The in vivo performance of the flexible dual-sided MEAs was validated by recording neural activities from the antennal lobe of the locust brain. Using an 8-channel MEA, we successfully captured extracellular neural signals from all channels concurrently (**Fig. 3.3a**), demonstrating the MEA's ability to record high-quality neural signals across multiple channels. The raw neural voltage signals were recorded following a 300 Hz high-pass filter application to eliminate low-frequency noise, allowing for the clear identification of action potentials.

To further analyze the recorded data, spike sorting was performed, which isolated distinct neural units from the raw signals. The spike-sorted waveforms displayed different patterns across channels, indicating the ability of the MEAs to capture diverse neural activities within the brain (**Fig. 3. 3d**). Principal Component Analysis (PCA) was applied to the spike data, allowing for the classification of individual spikes into separate clusters based on their waveform characteristics (**Fig. 3.3b and c**). This demonstrated the effectiveness of the MEAs in segmenting and characterizing neural responses from different neural populations.

3.2 Lung Cancer Volatile Organic Compounds Evoked Distinct Neural Responses in The Locust Antennal Lobe.

After validating the in vivo recording performance of the flexible dual-sided MEA, the study progressed to evaluate how projection neurons (PNs) in the locust's antennal lobe reacted to four distinct lung cancer biomarkers: nonanal, hexanal, pentanal, and propylbenzene. These compounds have previously been identified in varying concentrations in the exhaled breath of lung cancer patients (Poli et al., 2005;Fuchs et al., 2010). For the experiments, each biomarker

was diluted in mineral oil to a concentration of 1% v/v, with pure mineral oil serving as the control odor. The experimental arrangement, depicted in **Fig. 3.1A**, involved delivering these lung

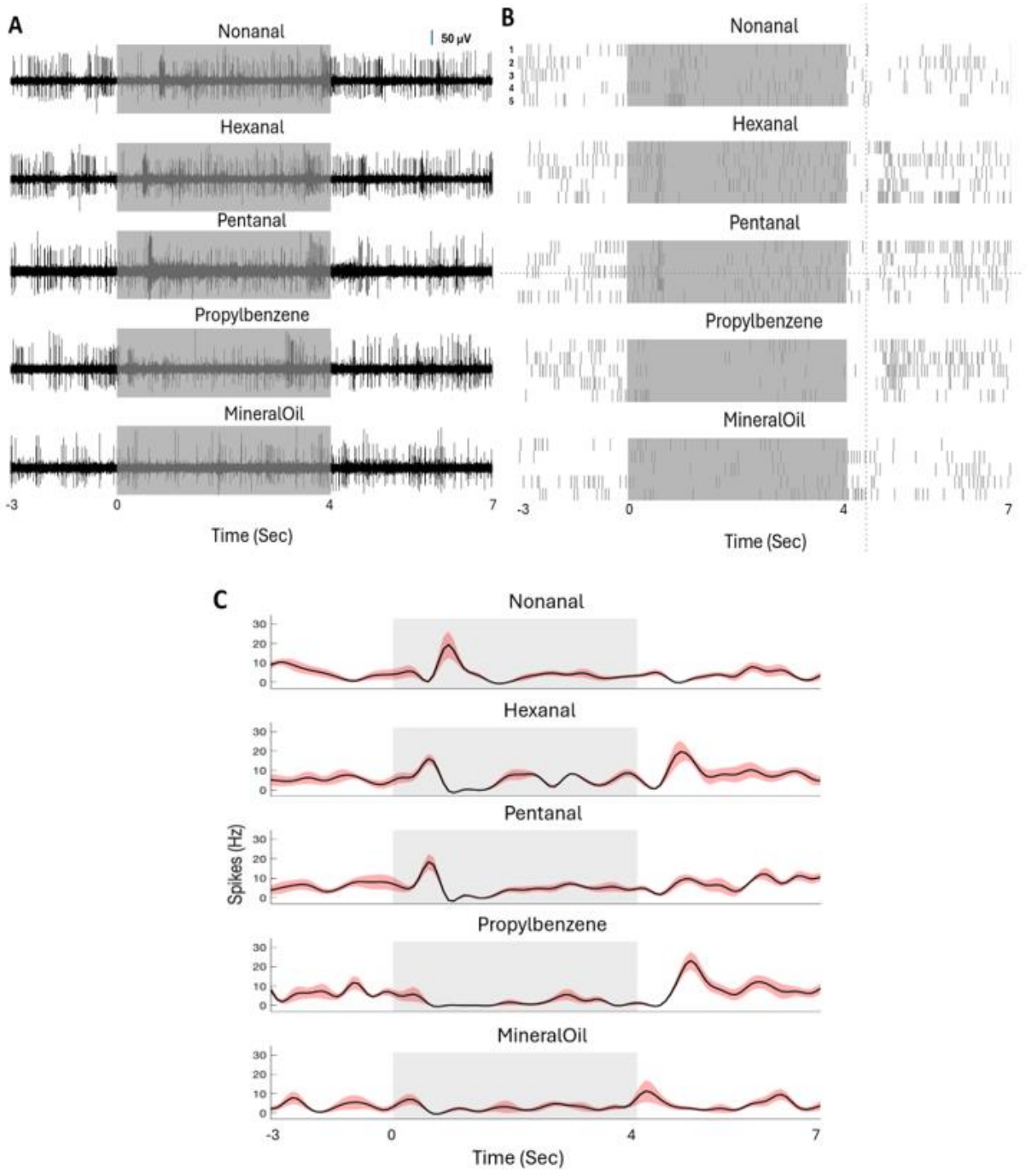

Figure. 3.4. Individual neurons display distinct VOC evoked responses to lung cancer biomarkers. *(A) Representative extracellular voltage traces are shown, recorded from a designated site within the locust's antennal lobe when presented with lung cancer biomarkers*

Figure 3.4 (cont'd)
diluted in mineral oil (1% v/v) and pure mineral oil as a control. The light grey box highlights the 4-second interval during which the VOCs were administered. (B) A representative raster plot is displayed for a single neuron, spike-sorted from the voltage traces shown in panel A. This plot includes 5 trials in which the VOC was delivered to the locust's antennae, with each line indicating a neuron's spiking event or action potential. (C) Peri-stimulus time histograms (PSTHs) derived from the spike data for the same neuron are illustrated. These histograms compute the average changes in spiking rates over the 5 trials depicted in the raster plot. An increase in average firing rate appears as a denser accumulation of lines in the raster plot. The trial-averaged PSTHs are plotted with a shaded region marking the standard error of the mean (S.E.M.), with the light grey box again denoting the 4-second VOC presentation window.

cancer biomarker VOCs to the locust's antennae using an olfactometer, while in vivo extracellular neural recordings were captured from the PNs within the antennal lobe. Each VOC was presented five trials to the locust's antenna.

Fig. 3.4A and B illustrates the evoked neural responses towards each VOC. Distinct neural responses to each biomarker were evident in these voltage traces. Subsequent spike sorting from these voltage traces allowed for the isolation of individual neurons, whose firing rates were analyzed using peri-stimulus time histograms and raster plots[165]. An example of these neural responses is shown in **Fig. 3.4B**, where a single neuron exhibited unique and distinct responses to each lung cancer biomarker. Notably, as demonstrated in **Fig. 3.4C**, nonanal elicited a significant increase in spiking frequency immediately upon exposure, which persisted throughout the 4-second stimulus period compared to baseline activity. Conversely, propylbenzene induced an inhibitory response at the onset of the stimulus. This differential response underscores the capability of individual neurons to distinctly recognize and respond to each VOC, thereby illustrating the potential of this method in differentiating lung cancer biomarkers at the neuronal level.

3.3 Classification of Lung Cancer VOC Biomarkers Via a Population Neural Response Analysis of Antennal Lobe Projection Neurons

It is presumed that in the locust antennal lobe the odor identity is not encoded by single neurons but using spatiotemporal population neural responses[178-181, 278]. Therefore, next, we examined a population of antennal lobe projections neurons (n = 69) and their responses to each of the lung cancer VOC biomarkers over a specific time window showing the evolution of the population response over time. Using dimensionality reduction techniques such as principal component analysis (PCA) and linear discriminant analysis (LDA) we were able to reduce the data from a high dimensional dataset (69 dimensions) to a low dimensional subspace to visualize the population neural responses in a 3-dimensional PCA or LDA space (**Fig. 3.5A** and **B**). Using these techniques, we can qualitatively see unique and separate trajectories in 3-dimensional PCA subspace that represent the population neural responses to each of the lung cancer biomarkers over 1.5 seconds during the odor stimulus (see **Fig. 3.6**). The angles in which these trajectories move in different directions signify that these biomarkers are eliciting unique and distinct responses in the neuronal population (**Fig. 3.5A**). Furthermore, using LDA, we observed distinct clusters of 50 ms time bins (30 total time bins for each biomarker) displaying that the population neural responses were able to differentiate each of the lung cancer biomarker tested (**Fig. 3.5B**). We next sought to predict the classification success of each of the lung cancer biomarkers using a high dimensional, leave-one-trial-out (LOTO) analysis based on 1.5 second trials in high dimensional space (69 dimensions) (**Fig. 3.5C**). To achieve this, we created training templates that consisted of the average spiking events of 50 ms time bins across four trials with the 5^{th} trial being left out to be used as a test template for each odor. This resulted in 5 training templates and 5 testing templates due to the 4 VOCs and mineral oil used in this study. Both the average of the four trials (training template) and

the 5th trial (testing template) consists of 50 ms time bins over a specified duration of stimulus exposure time. PN responses were segregated in 50 ms time bins due to the 20 Hz local field oscillation present in the locust AL [282-284]. The averaged 50 ms time bins from the training template were used to classify the 50 ms time bins from the test template in a time binned-matched manner by considering each time bin as a point in the high dimensional space. The Euclidean distances between each test time bin and all 5 training time bins were calculated with the test time bin being assigned to the biomarker with the associated closest training time bin. This was repeated for the total number of time bins (1.5 seconds = 30 time bins, 50 ms each) and cycled through each of the 5 trials so that each trial (1-5) will have the chance of being the trial that is left out (or test trial). In this way we classified the test template (trials 1-5) for each VOC and mineral oil in a bin-wise manner and summarized the percentages of time bins classified for each biomarker in a confusion matrix (**Fig. 3.5C**). Using this method, we observe that most of the time bins were classified correctly as indicated by the high diagonal values in the confusion matrix as shown in **Fig. 3.5C** with an accuracy of 58.93%. We then classified the entire test trial by taking the mode classification values of the each 50 ms time bins and assigning the whole trial to the biomarker associated with the mode of the time bin classification as shown in **Fig. 3.5D.** Our trial-wise classification results achieved 100% accuracy. To attain this high accuracy, experimental data from several electrophysiological recordings (12 experiments) were combined. In our next step, we wanted to investigate whether the multichannel MEAs fabricated for this study were robust and efficient enough for recording neural responses for lung cancer biomarker classification from a single electrophysiological recording.

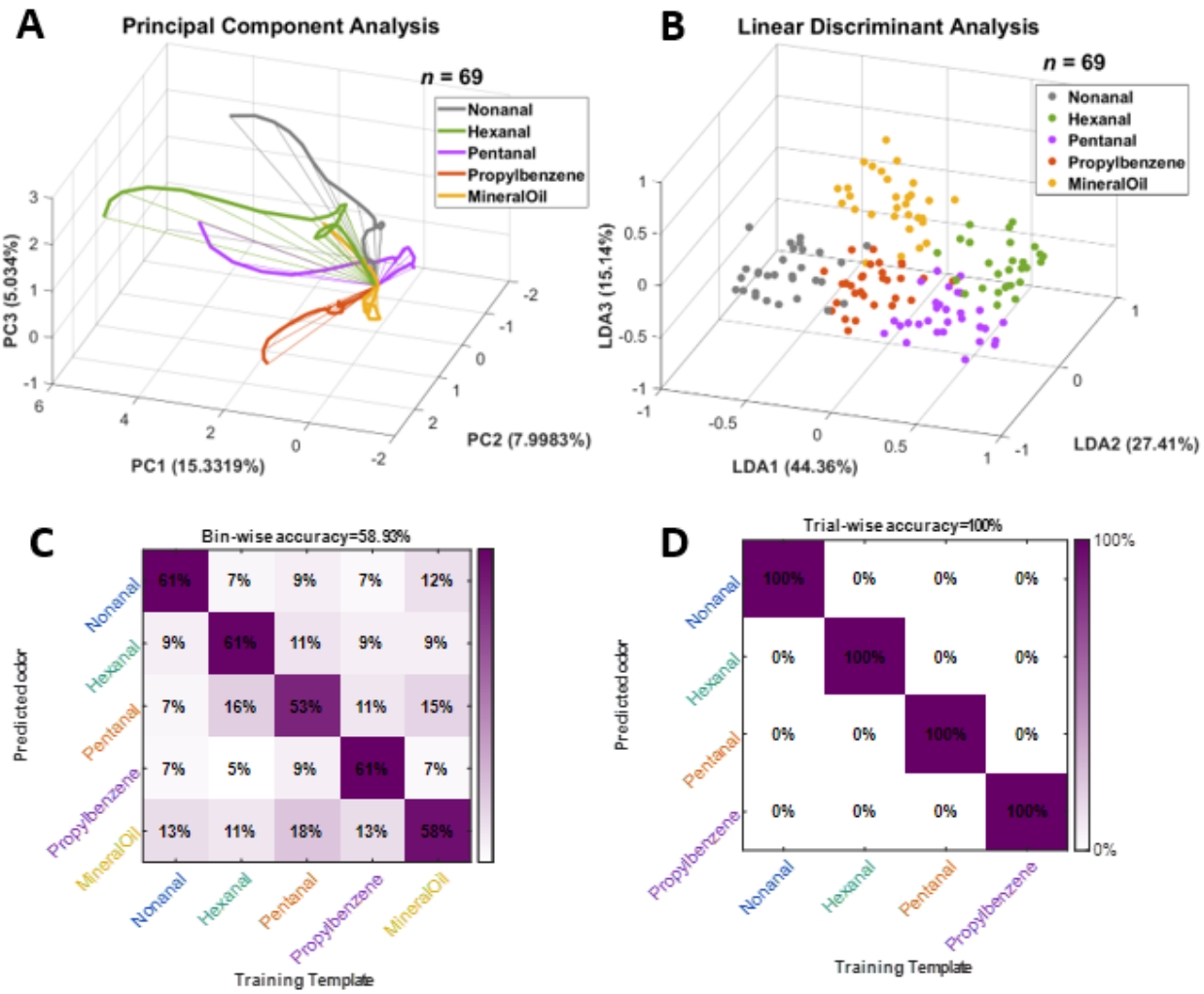

Figure 3.5. Population neural response analysis classifies each lung cancer biomarker. *(**A**) Population neural trajectories of all 69 neurons are shown after dimensionality reduction via principal component analysis (PCA). The trajectories are plotted between 0.25 – 1.75 seconds after stimulus onset which encompasses the most discriminatory segment of the population neural response. Distinct and separate trajectories indicate differentiation of neural responses to lung cancer VOCs at the population neuron level. All trajectories are aligned at 0.25 seconds after odor onset (indicated by a black dot), which roughly corresponds to the time of the odor plume hitting the antennae after the opening of the final valve (at 0.0 seconds). (**B**) Population neural response clusters of all 69 neurons are shown after dimensionality reduction via linear discriminant analysis (LDA).* (**C**) Confusion matrix displaying the performance of a *leave-one-trial-out* analysis for bin-wise classification is shown. Each 50 ms population response time bins are classified for each lung cancer VOC and mineral oil with an average accuracy of 58.93%. Note the dark purple boxes along the diagonal of the confusion matrix indicate that most of the 50-ms time bins were classified correctly. (**D**) Confusion matrix displaying the performance of a *leave-one-trial-out* analysis for trial-wise classification is shown. 1.5 s trials are classified for each lung cancer biomarker with an average accuracy of 100%.

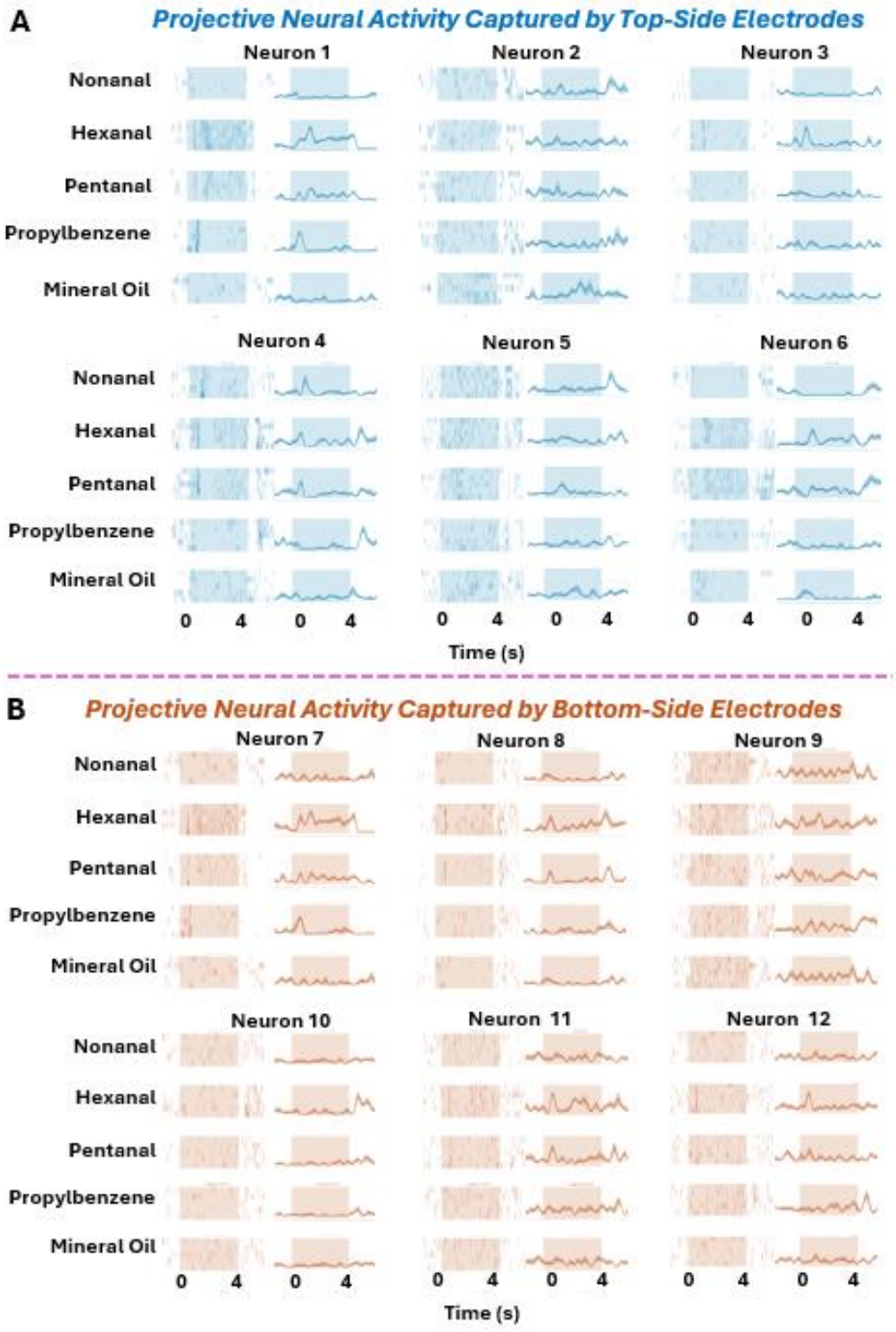

Figure 3.6. Robust and efficient classification of lung cancer biomarkers based on the neural responses from a single electrophysiological recording(To be continued).

Figure 3.6 (cont'd)

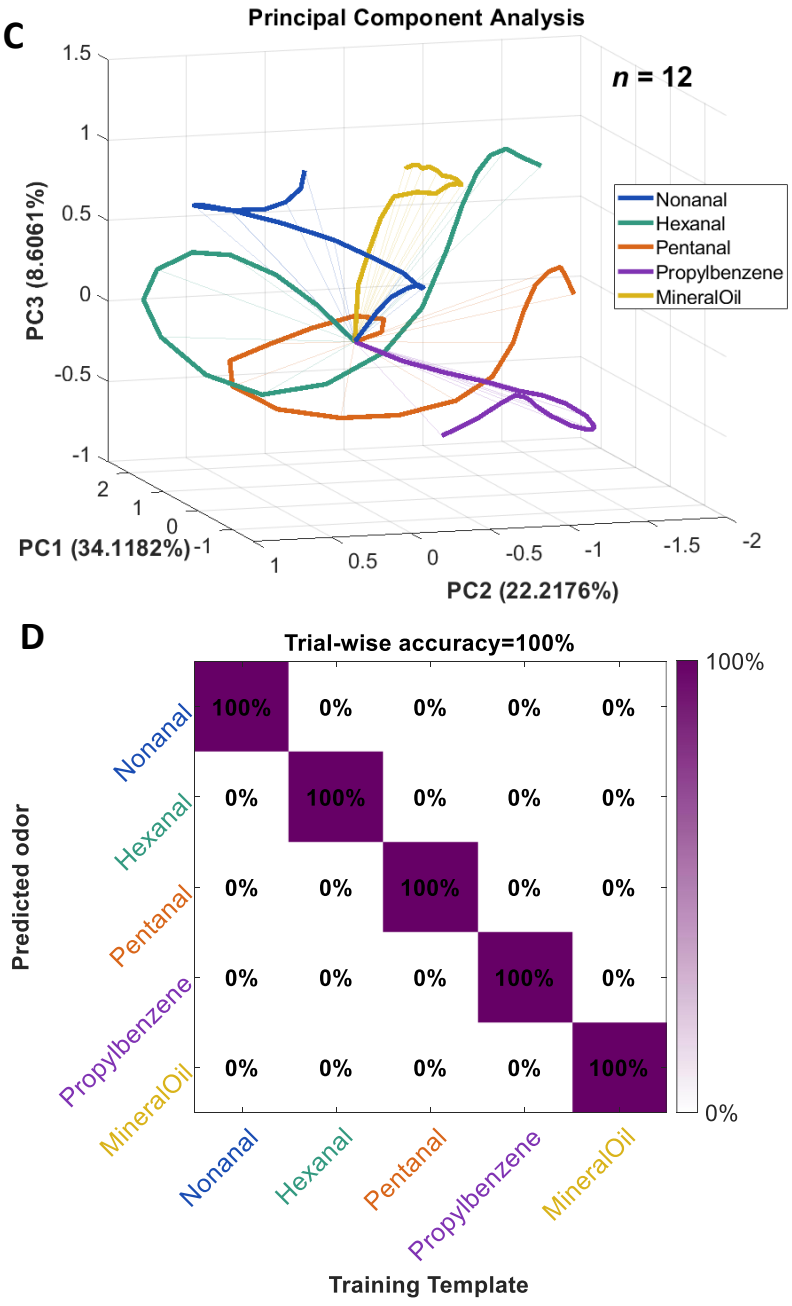

*(**A**) Raster and PSTHs of 6 of the 12 neurons recorded from top-sided electrodes in a single electrophysiological recording are shown(Blue). Raster plots contain 5 trials, in which the VOC was delivered to the locust antennae. Each line in the raster plot indicates a spiking event, or action potential, from the neuron. PSTHs show the average changes in spiking rate for the 5 trials shown in the corresponding raster plot. The grey box indicates the 4 second VOC presentation window.* ***(B)*** *Raster and PSTHs of 6 of the 12 neurons recorded from bottom-sided electrodes in a single electrophysiological recording are shown(Orange).* ***(C)*** *Neural trajectories of the 12 simultaneously recorded neurons are dimensionality reduction via principal component analysis.*

Figure 3.6 (cont'd)
*Distinct and separate trajectories indicate the differentiation of neural responses to lung cancer VOCs. The trajectories are plotted combining the population responses between 0.5 – 1.25 and 4.5 – 5 seconds after stimulus onset which includes the two most discriminatory segments of the population neural response. (**D**) Confusion matrix displaying the performance of a leave-one-trial-out analysis for trial-wise classification. 1.25 s duration trials are classified for each lung cancer biomarker with a mean accuracy of 88%.*

3.5 Efficient Classification of Lung Cancer Biomarkers from A Single MEA Recording

From a single electrophysiological recording, 12 neurons were identified and analyzed, as shown in **Fig. 3.6A**. These neurons exhibited diverse responses to the four VOC biomarkers (Hexanal, Nonanal, Pentanal, and Propylbenzene) and the control (Mineral Oil). The responses included both excitatory and inhibitory activities during VOC stimulation ("On response", 0.5-1.25 second after stimulation) and after stimulus termination ("Off response", 0.5-1.0 second after stimulation). By combining the "On" and "Off" responses across the neuron population and performing principal component analysis (PCA), distinct neural trajectories corresponding to each VOC biomarker and mineral oil were observed in low-dimensional PCA space. These trajectories demonstrated that the responses of just 12 neurons were sufficient to encode the identity of each VOC and the control, enabling high-dimensional classification analysis. Using a leave-one-trial-out (LOTO) classification analysis, 1.25-second trials encompassing both the "On" and "Off" responses were used to classify the biomarkers. This approach achieved an accuracy of 88%(shown in **Fig. 3.6D**), highlighting the sensitivity and robustness of this novel biosensing platform.

4. DISCUSSION

The current technologies that the potential of VOC analysis, such as electronic noses (e-noses), and mass spectrometry-based methods (e.g., GC-MS), have their own weakness in application of early lung cancer detection(as shown in **Table 3.1**). E-noses have been developed to emulate the biological principles of gas sensing using cross-selective sensor arrays and pattern

recognition algorithms [272, 277, 285]. These e-noses have been applied to detect and classify various cancers, including lung [273, 274], prostate [275], and head and neck cancers [276]. Despite their portability, e-noses struggle to match the sensitivity and accuracy of biological olfactory systems[267, 268, 270, 272, 286]. To enhance their performance, previous studies have integrated biological olfactory components, such as insect olfactory receptors, into e-noses[287-298]. The sensitivity and selectivity of these biological elements for VOC detection have been well-documented, along with their ability to extensively probe chemical space. Nevertheless, such sensors still face limitations, including selectivity for a wide range of compounds, sensitivity to humidity and other environmental factors, and reduced long-term reliability due to sensor drift[267, 268, 277, 299-301]. This study circumvents the need to integrate isolated biological components into e-noses by utilizing the entire olfactory system of the locust, combined with a dual-sided MEA. This integration forms a bioelectronic platform capable of detecting lung cancer biomarkers, leveraging the innate capabilities of the locust's olfactory system.

This study demonstrates that lung cancer VOCs can be effectively detected and differentiated using a brain-based bioelectronic sensor that capitalizes on biological olfaction and high-resolution MEAs for neural recording. This forward engineering approach harnesses the complete chemosensory array of the insect antenna and the biological odor processing capabilities of the antennal lobe to capture specific neural data related to lung cancer VOCs. This method eliminates the need for engineered chemical sensors for VOC detection. By *analyzing in vivo* population neural responses across electrophysiological recordings, distinct trajectories in principal component analysis and unique clusters in linear discriminant analysis were observed for each of the lung cancer biomarkers. These results suggest that neuronal signatures or "fingerprints" are encoded at the population level for each VOC biomarker and can serve as templates for label-free

VOC classification. Additionally, the need for time-intensive multiple experimental recordings is reduced by integrating this approach with custom-designed MEAs, enabling effective recording of neural responses from insect brains to achieve accurate VOC biomarker classification from a single neural recording. Thus, this platform is akin to one-shot classification for diseases via VOC biomarker detection. In conclusion, the research provides a novel platform that leverages biological olfaction and dual-sided MEAs for lung cancer detection, demonstrating that through the integration of biological and neural recording technologies, conventional gas sensor readouts for VOC analysis can be transcended, applying biological neural computational schemes for accessible and efficient disease detection.

In the present study, MEAs were utilized to record raw neural voltage signals in response to lung cancer VOC stimuli, thus validating the in vivo recording potential of the platform for analyzing single VOC samples. Future directions for this research involve advancing the capability of the platform to classify VOC mixtures derived from cultured cells, biological fluids or exhaled breath samples. Additionally, the design of MEAs for high-throughput neural recording will be refined to augment the number of projection neurons (PNs) recorded simultaneously, thereby reducing the necessity for numerous experiments required for comprehensive neural population analysis. Applications in point-of-care settings will also be considered, including the pre-concentration of breath samples onto sorbent tubes to facilitate off-line analysis for healthcare monitoring. Although the current biosensing approach has demonstrated the feasibility of detecting individual biomarkers, the specificity for particular diseases remains limited when relying on single biomarkers. It is anticipated that the detection of multiple VOCs will enhance the specificity needed for accurate disease diagnosis.

Table 3.1 Comparison of VOC detection technologies

Technology	Detection Limit	Sensitivity	Advantages	Limitations
Mass spectrometry-based methods, such as **GC-MS**	ppt to ppb	Very High	Extremely accurate and sensitive, gold standard	Expensive, time-consuming, requires extensive sample prep, big size[302].
Electronic Nose (e-nose)	ppm to ppb	Moderate	Portable, fast, cost-effective, real-time monitoring	Less power in selectivity(Individual VOCs not identified), inter-device data comparisons (of results) not usually possible, Sensor drift over time affects reproducibility[303].
Low-Dose Computed Tomography (LDCT)	Detection of lung nodules	High for lung nodules	Proven efficacy in detecting lung cancer in high-risk patients, non-invasive, widely used clinically	Nodules should be in a detectable size, high false positive rate, involves radiation exposure, costly for frequent screenings and office visiting[304].
Our Bioelectronic Platform	1 ppm	High	Non-invasive for humans, high sensitivity and selectivity. portable, no prescription needed for cancer screening. potential for miniaturization	Requires further validation with more VOCs

5. SUMMARY

Here we demonstrate a forward engineering approach utilizing the flexible dual-sided MEAs and odor coding schemes of the insect antennal lobe for label-free lung cancer VOC detection and classification. The flexible dual-sided MEAs were specifically designed for the compact neural olfactory regions of insects. Fabricated by our unique folding-bonding process and PEDOT:PSS surface coating technique, these flexible dual-sided MEAs exhibited excellent mechanical stability and electrochemical integrity through insertion, bending, and soaking tests. By implanting the flexible dual-sided MEAs into the antennal lobe of the locust brain, we recorded high quality neural responses of PNs to four different lung cancer biomarkers (nonanal, hexanal, pentanal, propylbenzene). The PNs displayed unique responses to each lung cancer VOC biomarker, showing individual neurons' ability to have distinct responses to lung cancer VOCs.

By combining PN responses across recordings and employing a high dimensional population response analysis, unknown VOCs could be classified with a 100% accuracy. Meanwhile, we demonstrated the ability of our system to detect concentration-dependent responses in locust antennal lobe neurons in a low of Nonanal and Propylbenzene, highlighting their potential utility in precise and scalable detection of lung cancer biomarkers. Moreover, using only a single electrophysiological recording, we were able to investigate the classification for lung cancer biomarker prediction to obtain an accuracy of 88%, showcasing the efficiency of this novel platform. By providing a method for efficient and robust detection of lung cancer biomarkers, this study contributes a novel diagnostic tool that has potential application in clinical settings. Ultimately, this research paves the way for innovative biological-based diagnostic approaches that could significantly improve early detection rates and, consequently, patient prognoses in lung cancer and beyond.

CHAPTER 4: OUTLOOK, ONGOING WORK AND CONCLUSIONS

1. OUTLOOK AND FUTURE DIRECTION

The methodologies and insights gained from this study herald new avenues for the development and application of flexible, high-density MEAs in biodetection through neural activities. These developments not only aim to enhance the capabilities of MEAs in neuroscience but also to expand their applications into bioelectronics, medical diagnostics, and environmental monitoring.

(1) **Enhancing Channel Count and Density:** The future of MEAs lies in enhancing their channel count and density. This progression will involve meticulous design adjustments to pack more electrodes into these arrays without compromising their individual sensitivity or the overall device flexibility. Increasing the channel count enhances the resolution and the granularity of neural recordings, allowing for more precise mappings of neural activity across complex brain tissues. This enhancement is critical for decoding intricate neural networks and understanding multifaceted brain functions and disorders.

(2) **Developing Array Configurations with Multiple Shanks:** Advancing beyond the basic layouts, the integration of MEAs with multiple shanks configured in array formations could significantly broaden their application scope. Such configurations would enable simultaneous recordings from various brain regions, facilitating comprehensive studies on inter-regional brain communication and neural network dynamics. This multi-pronged approach would be particularly beneficial in studying systemic neurological phenomena or in applications spanning larger or more diverse tissue areas.

(3) **Calibrating and Benchmarking Sensing Performance:**

To ensure the sensor's competitiveness and applicability, its sensing performance will be

systematically calibrated and benchmarked against other state-of-the-art technologies. Key parameters such as the limit of detection, sensitivity, accuracy, selectivity, and response time will be rigorously evaluated. Calibration will involve controlled exposure to known concentrations of target VOCs, enabling precise characterization of detection thresholds and response dynamics. Sensitivity and accuracy will be validated through comparative testing with gold-standard methods like gas chromatography-mass spectrometry (GC-MS), ensuring the sensor's ability to detect trace levels of biomarkers with high precision. Selectivity will be assessed by testing the sensor's responses to potential interfering compounds to confirm its specificity for target VOCs. Additionally, response time will be quantified to establish its suitability for real-time applications. This systematic benchmarking will highlight the sensor's advantages and identify areas for improvement, ensuring it meets or exceeds the performance of existing diagnostic tools.

(4) **Diversifying VOC Detection for Enhanced Diagnostics:** Enhancing the ability of MEAs to detect a wider range of volatile organic compounds emitted by various biological sources, such as different types of cancer cells or infectious agents, could lead to the development of more accurate and non-invasive diagnostic tools. This expansion would be instrumental in identifying multiple conditions and could substantially improve early diagnosis and treatment strategies. Specifically, detecting lung cancer-related odors from various cultured cells or expired gases from human beings could revolutionize how lung cancer is diagnosed and monitored, potentially enabling much earlier detection.

(5) **Expanding Applications in Disease Detection:** Broadening the use of MEAs to include the detection of biomarkers for various diseases—extending beyond the scope of lung cancer—presents a revolutionary potential in early detection and monitoring. Leveraging

the sensitive and selective detection capabilities of MEAs could transform these devices into vital tools for medical diagnostics and herald a new era in personalized medicine. The application of MEAs in detecting VOCs emitted from various pathogens or affected tissues could lead to breakthroughs in non-invasive diagnosis techniques, providing a quicker, more effective way to manage and treat diseases.

(6) **Implementing Environmental Monitoring Capabilities:** Diversifying the detection capabilities of MEAs to encompass a broader spectrum of VOCs from various sources including environmental pollutants enhances their utility in public health. The sensitivity of MEAs to detect low concentrations of various compounds could be pivotal in monitoring air quality and detecting hazardous substances, offering a powerful tool for environmental protection and public health preservation.

(7) **Integrating Wireless Technologies:** Incorporating wireless technology into MEA systems could transform their usability and accessibility[305]. Wireless MEAs could facilitate real-time monitoring of patients and environmental conditions, support remote healthcare provision, and reduce the logistical burdens of wired systems in clinical and research settings. This feature would be particularly advantageous in creating devices that are not only more user-friendly but also capable of providing continuous, uninterrupted data streams.

In conclusion, the path forward for MEAs is marked by vast potential and the promise of significant technological and scientific advancements. By building on the groundwork laid by this dissertation, future research can extend these applications into clinical settings and beyond, potentially transforming the landscape of disease diagnosis, environmental monitoring, and neurological research.

2. ONGOING WORK

Developing Array Configurations with Multiple Shanks:

Current efforts are focused on enhancing the design of MEAs by integrating multiple shanks within a single device. This development is pivotal for facilitating simultaneous recordings from diverse brain regions or various biological tissues. By enabling interactions with multiple networks, this sophisticated architecture will substantially enrich our understanding of neural interconnectivity and the integrated functionality of the brain. The multi-shank arrays aim to capture a more comprehensive depiction of neural activities, offering new insights into neurological conditions and advancing our understanding of cognitive processes and brain disorders.

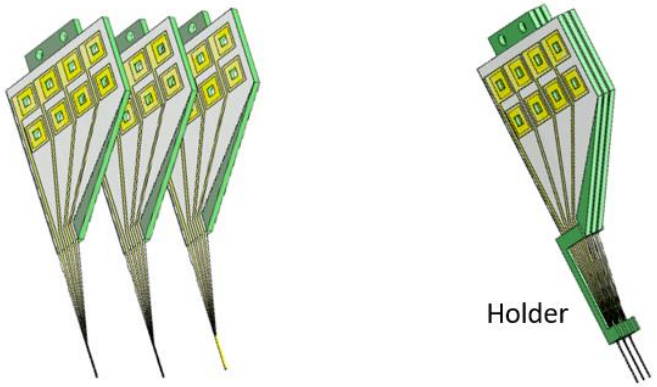

Figure 4.1. Schematic of assembling multiple shanks of MEA to form a 3-D configuration.

Fig. 4.1 illustrates the assembly process of multiple shanks from MEAs to create a three-dimensional configuration. Here, individual MEA shanks are methodically arranged and securely held using a specially designed holder. This holder, critical for maintaining a precise inter-shank spacing, is produced using a Nanoscribe system(Quantum Bio X, Nanoscribe, Germany), which allows for exceptional accuracy and detail in fabricating complex structures. The precise spacing between shanks, essential for effective neural mapping and signal clarity, is set at 150 micrometers. This configuration is depicted in **Fig.** 4.2, which shows a close-up view of the tips

of an assembled dual-shank MEA setup. The strategic placement of shanks enhances the array's ability to capture a comprehensive range of neural signals across different spatial dimensions, thus providing a richer, more detailed understanding of neural activity in the studied biological tissue.

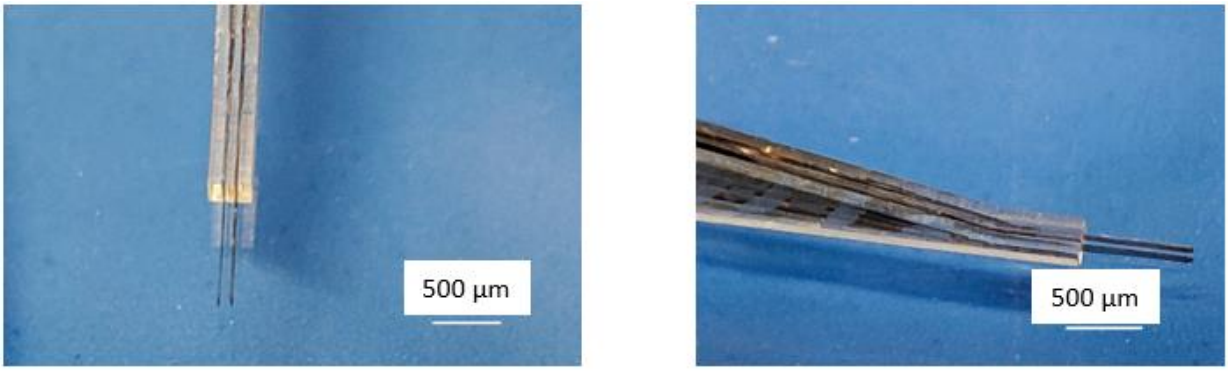

Figure 4.2. Tip of an assembled two-shank MEAs. *The precise spacing between shanks, essential for effective neural mapping and signal clarity, is set at 150 micrometers.*

3. CONCLUSIONS

In this study, we significantly advanced the field of neural interfacing by developing flexible, dual-sided MEAs through an innovative folding-annealing technique, specifically optimized for the compact neural structures of insect models. These MEAs, tailored for the intricacies of locust antennal lobes—the primary olfactory centers—demonstrated substantial effectiveness in vivo. They captured detailed neural responses to lung cancer VOCs, highlighting their potential in medical diagnostics. Our MEAs maintain their integrity and performance through rigorous mechanical and electrochemical testing, including insertion, bending, and extended soaking, underscoring their suitability for chronic applications in both research and clinical settings.

Summary of Key Findings:

(1) **Electrode Coating Strategies**: By meticulously optimizing PEDOT: PSS electrodeposition using CV, we have established that utilizing a low voltage range (-0.7 V

to 0.9 V) and limiting the process to two CV cycles significantly enhances the electrochemical properties of the electrodes. This method strikes an essential balance between increased surface area and reduced impedance, crucial for high-quality, high-resolution neural recordings. The smaller electrodes, particularly the 10 μm and 20 μm variants, have benefited immensely from this coating strategy, rendering them ideal for detailed studies within small brain regions.

(2) **Fabrication Techniques**: The innovative folding-annealing technique employed within this study has effectively doubled the channel density of the MEAs without enlarging their physical footprint, thereby preserving mechanical flexibility and structural integrity. This fabrication method ensures robust bonding between the parylene layers and maintains the electrochemical performance of the electrodes across various manufacturing and handling processes. The mechanical stability of these MEAs has been rigorously tested through insertion into brain tissue phantoms, bending, and prolonged soaking in physiological conditions, all of which confirmed the durability and functionality of the MEAs for long-term applications in both research and clinical settings.

(3) **Biomedical Applications**: Our research has taken a forward engineering approach utilizing the flexible dual-sided MEAs and the intricate odor coding schemes observed in the insect antennal lobe for label-free detection and classification of lung cancer VOCs. Implanting these MEAs into the antennal lobe of the locust brain, we captured high-quality neural responses to various lung cancer biomarkers, revealing distinct patterns for each VOC. This setup not only confirmed the individual neurons' capability to respond uniquely to different lung cancer VOCs but also allowed for the precise classification of unknown VOCs with high accuracy using population response analysis.

BIBLIOGRAPHY

[1] X. Liu *et al.*, "Flexible Dual-Sided Polymer Microelectrode Array for Neurophysiological Recordings from an Insect Brain," in *2024 IEEE 37th International Conference on Micro Electro Mechanical Systems (MEMS)*, 21-25 Jan. 2024 2024, pp. 247-250, doi: 10.1109/MEMS58180.2024.10439398.

[2] X. Liu, Y. Gong, Z. Jiang, T. Stevens, and W. Li, "Flexible high-density microelectrode arrays for closed-loop brain–machine interfaces: a review," *Frontiers in Neuroscience,* vol. 18, p. 1348434, 2024. [Online]. Available: https://pmc.ncbi.nlm.nih.gov/articles/PMC11057246/pdf/fnins-18-1348434.pdf.

[3] C. F. Higgins, "Multiple molecular mechanisms for multidrug resistance transporters," *Nature,* vol. 446, no. 7137, pp. 749-757, 2007.

[4] A. L. Hodgkin and A. F. Huxley, "A quantitative description of membrane current and its application to conduction and excitation in nerve," *J Physiol,* vol. 117, no. 4, pp. 500-44, Aug 1952, doi: 10.1113/jphysiol.1952.sp004764.

[5] M. Zhang, Z. Tang, X. Liu, and J. Van der Spiegel, "Electronic neural interfaces," *Nature Electronics,* vol. 3, no. 4, pp. 191-200, 2020/04/01 2020, doi: 10.1038/s41928-020-0390-3.

[6] J. Rettinger, S. Schwarz, and W. Schwarz, *Electrophysiology*. Springer, 2016.

[7] G. Hong and C. M. Lieber, "Novel electrode technologies for neural recordings," *Nat Rev Neurosci,* vol. 20, no. 6, pp. 330-345, Jun 2019, doi: 10.1038/s41583-019-0140-6.

[8] T. A. M. Janjua, T. G. N. d. S. Nielsen, F. R. Andreis, S. Meijs, and W. Jensen, "The effect of peripheral high-frequency electrical stimulation on the primary somatosensory cortex in pigs," *IBRO NEUROSCIENCE REPORTS,* Article vol. 11, pp. 112-118, 2021 DEC 2021, doi: 10.1016/j.ibneur.2021.08.004.

[9] X. M. Fan *et al.*, "Editorial: Multimodal fusion technologies and applications in the context of neuroscience," *Frontiers in Neuroscience,* vol. 17, May 2023, Art no. 1213207, doi: 10.3389/fnins.2023.1213207.

[10] M. Mohammed *et al.*, "Microelectrode clusters enable therapeutic deep brain stimulation without noticeable side-effects in a rodent model of Parkinson's disease," (in English), *Journal of Neuroscience Methods,* Article vol. 365, p. 11, Jan 2022, Art no. 109399, doi: 10.1016/j.jneumeth.2021.109399.

[11] L. A. Johnson, S. D. Nebeck, A. Muralidharan, M. D. Johnson, K. B. Baker, and J. L. Vitek, "Closed-loop deep brain stimulation effects on parkinsonian motor symptoms in a non-human primate–is beta enough?," *Brain stimulation,* vol. 9, no. 6, pp. 892-896, 2016.

[12] L. K. Olsen *et al.*, "Vagus nerve stimulation-induced cognitive enhancement: Hippocampal neuroplasticity in healthy male rats," *BRAIN STIMULATION*, Article vol. 15, no. 5, pp. 1101-1110, 2022 SEP-OCT 2022, doi: 10.1016/j.brs.2022.08.001.

[13] K. K. Ang *et al.*, "A randomized controlled trial of EEG-based motor imagery brain-computer interface robotic rehabilitation for stroke," *Clinical EEG and neuroscience*, vol. 46, no. 4, pp. 310-320, 2015.

[14] A. R. Donati *et al.*, "Long-term training with a brain-machine interface-based gait protocol induces partial neurological recovery in paraplegic patients," *Scientific reports*, vol. 6, no. 1, p. 30383, 2016.

[15] M. Liu and J. Ushiba, "Brain–machine Interface (BMI)-based Neurorehabilitation for Post-stroke Upper Limb Paralysis," *The Keio Journal of Medicine*, vol. 71, no. 4, pp. 82-92, 2022.

[16] A. B. Ajiboye *et al.*, "Restoration of reaching and grasping movements through brain-controlled muscle stimulation in a person with tetraplegia: a proof-of-concept demonstration," *The Lancet*, vol. 389, no. 10081, pp. 1821-1830, 2017.

[17] W. Ouyang *et al.*, "A wireless and battery-less implant for multimodal closed-loop neuromodulation in small animals," *Nature Biomedical Engineering*, pp. 1-18, 2023.

[18] A. Castrioto and E. Moro, "New targets for deep brain stimulation treatment of Parkinson’s disease," *Expert Review of Neurotherapeutics*, vol. 13, no. 12, pp. 1319-1328, 2013.

[19] K. Scholten, C. E. Larson, H. Xu, D. Song, and E. Meng, "A 512-Channel Multi-Layer Polymer-Based Neural Probe Array," *Journal of Microelectromechanical Systems*, Article vol. 29, no. 5, pp. 1054-1058, Oct 2020, doi: 10.1109/jmems.2020.2999550.

[20] S. Little *et al.*, "Adaptive deep brain stimulation for Parkinson's disease demonstrates reduced speech side effects compared to conventional stimulation in the acute setting," *Journal of Neurology, Neurosurgery & Psychiatry*, vol. 87, no. 12, pp. 1388-1389, 2016.

[21] C. Adams *et al.*, "Development of flexible arrays for in vivo neuronal recording and stimulation," (in English), *Nucl. Instrum. Methods Phys. Res. Sect. A-Accel. Spectrom. Dect. Assoc. Equip.*, Article; Proceedings Paper vol. 546, no. 1-2, pp. 154-159, Jul 2005, doi: 10.1016/j.nima.2005.03.014.

[22] K. L. Chou, S. Grube, and P. G. Patil, *Deep brain stimulation: A new life for people with Parkinson's, dystonia, and essential Tremor*. Demos Medical Publishing, 2011.

[23] H.-S. Lee, K. Eom, M. Park, S.-B. Ku, K. Lee, and H.-M. Lee, "High-density neural recording system design," *Biomedical Engineering Letters*, Review vol. 12, no. 3, pp. 251-261, Aug 2022, doi: 10.1007/s13534-022-00233-z.

[24] Q. Zhang *et al.*, "A prototype closed-loop brain–machine interface for the study and treatment of pain," *Nature Biomedical Engineering*, vol. 7, no. 4, pp. 533-545, 2023/04/01 2023, doi: 10.1038/s41551-021-00736-7.

[25] J. M. A. Tanskanen, A. Ahtiainen, and J. A. K. Hyttinen, "Toward Closed-Loop Electrical Stimulation of Neuronal Systems: A Review," *BIOELECTRICITY*, Review vol. 2, no. 4, pp. 328-347, 2020 DEC 1 2020, doi: 10.1089/bioe.2020.0028.

[26] Y. Nam, "State-of-the-Art Technology on MEAs for Interfacing Live Neurons," in *Handbook of Neuroengineering*, 2021, ch. Chapter 8-2, pp. 1-41.

[27] C. M. Didier, A. Kundu, D. DeRoo, and S. Rajaraman, "Development of in vitro 2D and 3D microelectrode arrays and their role in advancing biomedical research," *Journal of Micromechanics and Microengineering*, vol. 30, no. 10, 2020, doi: 10.1088/1361-6439/ab8e91.

[28] M. E. Spira and A. Hai, "Multi-electrode array technologies for neuroscience and cardiology," *Nat Nanotechnol*, vol. 8, no. 2, pp. 83-94, Feb 2013, doi: 10.1038/nnano.2012.265.

[29] K. D. Wise, J. B. Angell, and A. Starr, "An Integrated-Circuit Approach to Extracellular Microelectrodes," *IEEE Transactions on Biomedical Engineering*, vol. BME-17, no. 3, pp. 238-247, 1970, doi: 10.1109/TBME.1970.4502738.

[30] C. A. Thomas, Jr., P. A. Springer, G. E. Loeb, Y. Berwald-Netter, and L. M. Okun, "A miniature microelectrode array to monitor the bioelectric activity of cultured cells," *Exp Cell Res*, vol. 74, no. 1, pp. 61-6, Sep 1972, doi: 10.1016/0014-4827(72)90481-8.

[31] G. W. Gross, E. Rieske, G. W. Kreutzberg, and A. Meyer, "A new fixed-array multi-microelectrode system designed for long-term monitoring of extracellular single unit neuronal activity in vitro," *Neurosci Lett*, vol. 6, no. 2-3, pp. 101-5, Nov 1977, doi: 10.1016/0304-3940(77)90003-9.

[32] J. Pine, "Recording action potentials from cultured neurons with extracellular microcircuit electrodes," *J Neurosci Methods*, vol. 2, no. 1, pp. 19-31, Feb 1980, doi: 10.1016/0165-0270(80)90042-4.

[33] W. G. Regehr, J. Pine, C. S. Cohan, M. D. Mischke, and D. W. Tank, "Sealing cultured invertebrate neurons to embedded dish electrodes facilitates long-term stimulation and recording," *J Neurosci Methods*, vol. 30, no. 2, pp. 91-106, Nov 1989, doi: 10.1016/0165-0270(89)90055-1.

[34] P. K. Campbell, K. E. Jones, R. J. Huber, K. W. Horch, and R. A. Normann, "A silicon-based, three-dimensional neural interface: manufacturing processes for an intracortical electrode array," *IEEE Trans Biomed Eng*, vol. 38, no. 8, pp. 758-68, Aug 1991, doi: 10.1109/10.83588.

[35] P. Thiebaud, N. F. d. Rooij, M. Koudelka-Hep, and L. Stoppini, "Microelectrode arrays for electrophysiological monitoring of hippocampal organotypic slice cultures," *IEEE Transactions on Biomedical Engineering*, vol. 44, no. 11, pp. 1159-1163, 1997, doi: 10.1109/10.641344.

[36] C. M. Didier, A. Kundu, D. DeRoo, and S. Rajaraman, "Development of in vitro 2D and 3D microelectrode arrays and their role in advancing biomedical research," *Journal of Micromechanics and Microengineering*, vol. 30, no. 10, p. 103001, 2020/07/03 2020, doi: 10.1088/1361-6439/ab8e91.

[37] L. Berdondini, T. Overstolz, N. F. d. Rooij, M. Koudelka-Hep, M. Wany, and P. Seitz, "High-density microelectrode arrays for electrophysiological activity imaging of neuronal networks," in *ICECS 2001. 8th IEEE International Conference on Electronics, Circuits and Systems (Cat. No.01EX483)*, 2-5 Sept. 2001 2001, vol. 3, pp. 1239-1242 vol.3, doi: 10.1109/ICECS.2001.957439.

[38] A. Tanwar, H. A. Gandhi, D. Kushwaha, and J. Bhattacharya, "A review on microelectrode array fabrication techniques and their applications," *Materials Today Chemistry*, Review vol. 26, Dec 2022, Art no. 101153, doi: 10.1016/j.mtchem.2022.101153.

[39] N. A. Steinmetz *et al.*, "Neuropixels 2.0: A miniaturized high-density probe for stable, long-term brain recordings," *Science*, Article vol. 372, no. 6539, pp. 258-+, Apr 16 2021, Art no. eabf4588, doi: 10.1126/science.abf4588.

[40] E. Kolaya and B. L. Firestein, "Deep brain stimulation: Challenges at the tissue-electrode interface and current solutions," *Biotechnology Progress*, vol. 37, no. 5, p. e3179, 2021, doi: https://doi.org/10.1002/btpr.3179.

[41] P. Oldroyd and G. G. Malliaras, "Achieving long-term stability of thin-film electrodes for neurostimulation," *Acta Biomaterialia*, vol. 139, pp. 65-81, 2022/02/01/ 2022, doi: https://doi.org/10.1016/j.actbio.2021.05.004.

[42] T. Araki *et al.*, "Flexible neural interfaces for brain implants-the pursuit of thinness and high density," *Flexible and Printed Electronics*, Review vol. 5, no. 4, Dec 2020, Art no. 043002, doi: 10.1088/2058-8585/abc3ca.

[43] N. Sharafkhani *et al.*, "Neural tissue-microelectrode interaction: Brain micromotion, electrical impedance, and flexible microelectrode insertion," *JOURNAL OF NEUROSCIENCE METHODS*, Article vol. 365, 2022 JAN 1 2022, Art no. 109388, doi: 10.1016/j.jneumeth.2021.109388.

[44] H. Xu *et al.*, "Acute in vivo Recording with a Generic Parylene Microelectrode Array Implanted with Dip-coating Method into the Rat Brain," in *2022 44th Annual International Conference of the IEEE Engineering in Medicine & Biology Society (EMBC)*, 11-15 July 2022 2022, pp. 214-217, doi: 10.1109/EMBC48229.2022.9870987.

[45] Y. Zhou *et al.*, "A mosquito mouthpart-like bionic neural probe," *Microsystems & nanoengineering*, Journal Article vol. 9, pp. 88-88, 2023 2023, doi: 10.1038/s41378-023-00565-5.

[46] G. K. K. Chik *et al.*, "Flexible Multichannel Neural Probe Developed by Electropolymerization for Localized Stimulation and Sensing," *Advanced Materials Technologies*, Article vol. 7, no. 8, Aug 2022, Art no. 2200143, doi: 10.1002/admt.202200143.

[47] A. Esteban-Linares *et al.*, "Graphene-based microfluidic perforated microelectrode arrays for retinal electrophysiological studies," *Lab on a Chip*, 10.1039/D3LC00064H vol. 23, no. 9, pp. 2193-2205, 2023, doi: 10.1039/D3LC00064H.

[48] W. Ling *et al.*, "Flexible Electronics and Materials for Synchronized Stimulation and Monitoring in Multi-Encephalic Regions," *Advanced Functional Materials*, vol. 30, no. 32, p. 2002644, 2020, doi: https://doi.org/10.1002/adfm.202002644.

[49] R. K. Shepherd *et al.*, "Platinum dissolution and tissue response following long-term electrical stimulation at high charge densities," *Journal of neural engineering*, vol. 18, no. 3, p. 036021, 2021.

[50] M. P. Ward, P. Rajdev, C. Ellison, and P. P. Irazoqui, "Toward a comparison of microelectrodes for acute and chronic recordings," *Brain Research*, vol. 1282, pp. 183-200, 2009/07/28/ 2009, doi: https://doi.org/10.1016/j.brainres.2009.05.052.

[51] A. Golabchi, B. Wu, B. Cao, C. J. Bettinger, and X. T. Cui, "Zwitterionic polymer/polydopamine coating reduce acute inflammatory tissue responses to neural implants," *Biomaterials*, vol. 225, p. 119519, 2019.

[52] P. Oldroyd and G. G. Malliaras, "Achieving long-term stability of thin-film electrodes for neurostimulation," *Acta biomaterialia*, vol. 139, pp. 65-81, Feb 2022, doi: 10.1016/j.actbio.2021.05.004.

[53] K. M. Szostak, L. Grand, and T. G. Constandinou, "Neural Interfaces for Intracortical Recording: Requirements, Fabrication Methods, and Characteristics," *Front Neurosci*, vol. 11, p. 665, 2017, doi: 10.3389/fnins.2017.00665.

[54] Y. Qiang *et al.*, "Crosstalk in polymer microelectrode arrays," *Nano Research*, Article vol. 14, no. 9, pp. 3240-3247, Sep 2021, doi: 10.1007/s12274-021-3442-8.

[55] M. H. Behfar *et al.*, "Failure mechanisms in flip‐chip bonding on stretchable printed electronics," *Advanced Engineering Materials*, vol. 23, no. 12, p. 2100264, 2021.

[56] F. Bonafe, "Flexible microelectrode array based on PEDOT:PSS for neural recording and stimulation," *NUOVO CIMENTO C-COLLOQUIA AND COMMUNICATIONS IN*

PHYSICS, Article vol. 45, no. 6, 2022 NOV-DEC 2022, Art no. 199, doi: 10.1393/ncc/i2022-22199-y.

[57] P. Le Floch *et al.*, "Stretchable Mesh Nanoelectronics for 3D Single-Cell Chronic Electrophysiology from Developing Brain Organoids," *ADVANCED MATERIALS*, Article vol. 34, no. 11, 2022 MAR 2022, Art no. 2106829, doi: 10.1002/adma.202106829.

[58] Z. Xiang *et al.*, "High-density stretchable microelectrode array based on multilayer serpentine interconnections," *Journal of Micromechanics and Microengineering*, Article vol. 32, no. 8, Aug 1 2022, Art no. 084002, doi: 10.1088/1361-6439/ac799d.

[59] K. G. Shah *et al.*, "Cylindrical microelectrode array for neural stimulation and recording," Patent US 11357975, 2022. [Online]. Available: <Go to ISI>://BCI:BCI202200618090

[60] R. Yin *et al.*, "Chronic co-implantation of ultraflexible neural electrodes and a cranial window," *NEUROPHOTONICS*, Article vol. 9, no. 3, 2022 JUL 1 2022, Art no. 032204, doi: 10.1117/1.NPh.9.3.032204.

[61] D. X. Yan *et al.*, "Ultraflexible and Stretchable Intrafascicular Peripheral Nerve Recording Device with Axon-Dimension, Cuff-Less Microneedle Electrode Array," (in English), *Small*, Article vol. 18, no. 21, p. 13, May 2022, Art no. 2200311, doi: 10.1002/smll.202200311.

[62] W. Hong *et al.*, "Ultrathin Gold Microelectrode Array using Polyelectrolyte Multilayers for Flexible and Transparent Electro-Optical Neural Interfaces," *Advanced Functional Materials*, vol. 32, no. 9, Feb 2022, Art no. 2106493, doi: 10.1002/adfm.202106493.

[63] K. Eunah, V. Mihály, B. György, and Y. Euisik, "flexLiTE: flexible micro-LED integrated optoelectrodes for minimally-invasive chronic deep-brain study," *bioRxiv*, p. 2022.08.05.503006, 2022, doi: 10.1101/2022.08.05.503006.

[64] B.-J. Choi, J.-H. Kim, W.-J. Yang, D.-J. Han, J. Park, and D.-W. Park, "Parylene-Based Flexible Microelectrode Arrays for the Electrical Recording of Muscles and the Effect of Electrode Size," *Applied Sciences*, vol. 10, no. 20, p. 7364, 2020. [Online]. Available: https://www.mdpi.com/2076-3417/10/20/7364.

[65] L. G. Wiedemann and A. J. McDaid, "On the function and robustness of skin-electrode interfaces for high-density electromyography: Towards ubiquitous integration with robotics devices," in *2017 IEEE Life Sciences Conference (LSC)*, 13-15 Dec. 2017 2017, pp. 137-140, doi: 10.1109/LSC.2017.8268162.

[66] Y. Wang, X. Yang, X. Zhang, Y. Wang, and W. Pei, "Implantable intracortical microelectrodes: reviewing the present with a focus on the future," *Microsystems & Nanoengineering*, Review vol. 9, no. 1, Jan 5 2023, Art no. 7, doi: 10.1038/s41378-022-00451-6.

[67] Q. Zeng, S. Yu, Z. Fan, Y. Huang, B. Song, and T. Zhou, "Nanocone-Array-Based Platinum-Iridium Oxide Neural Microelectrodes: Structure, Electrochemistry, Durability and Biocompatibility Study," *NANOMATERIALS,* Article vol. 12, no. 19, 2022 OCT 2022, Art no. 3445, doi: 10.3390/nano12193445.

[68] B. Ji *et al.*, "Flexible and stretchable opto-electric neural interface for low-noise electrocorticogram recordings and neuromodulation in vivo," *Biosensors and Bioelectronics,* vol. 153, p. 112009, 2020/04/01/ 2020, doi: https://doi.org/10.1016/j.bios.2020.112009.

[69] M. A. Brown *et al.*, "Direct laser writing of 3D electrodes on flexible substrates," *NATURE COMMUNICATIONS,* Article vol. 14, no. 1, 2023 JUN 17 2023, Art no. 3610, doi: 10.1038/s41467-023-39152-7.

[70] M. McDonald *et al.*, "A mesh microelectrode array for non-invasive electrophysiology within neural organoids," *BIOSENSORS & BIOELECTRONICS,* Article vol. 228, 2023 MAY 15 2023, Art no. 115223, doi: 10.1016/j.bios.2023.115223.

[71] N. Zeng *et al.*, "A Wireless, Mechanically Flexible, 25μm-Thick, 65,536-Channel Subdural Surface Recording and Stimulating Microelectrode Array with Integrated Antennas," (in eng), *2023 IEEE Symp VLSI Technol Circuits (2023),* vol. 2023, Jun 2023, doi: 10.23919/vlsitechnologyandcir57934.2023.10185321.

[72] E. Musk, "An Integrated Brain-Machine Interface Platform With Thousands of Channels," (in English), *Journal of Medical Internet Research,* Article vol. 21, no. 10, p. 14, Oct 2019, Art no. e16194, doi: 10.2196/16194.

[73] Y. Zhou *et al.*, "A silk-based self-adaptive flexible opto-electro neural probe," *MICROSYSTEMS & NANOENGINEERING,* Article vol. 8, no. 1, 2022 NOV 8 2022, Art no. 118, doi: 10.1038/s41378-022-00461-4.

[74] S. Park *et al.*, "Adaptive and multifunctional hydrogel hybrid probes for long-term sensing and modulation of neural activity," (in eng), *Nat Commun,* vol. 12, no. 1, p. 3435, Jun 8 2021, doi: 10.1038/s41467-021-23802-9.

[75] I. Uguz and K. L. Shepard, "Spatially controlled, bipolar, cortical stimulation with high-capacitance, mechanically flexible subdural surface microelectrode arrays," (in English), *Science Advances,* Article vol. 8, no. 42, p. 15, Oct 2022, Art no. eabq6354, doi: 10.1126/sciadv.abq6354.

[76] A. Schander, J. M. Gancz, M. Tintelott, and W. Lang, "Towards Long-Term Stable Polyimide-Based Flexible Electrical Insulation for Chronically Implanted Neural Electrodes," *Micromachines (Basel),* vol. 12, no. 11, Oct 20 2021, doi: 10.3390/mi12111279.

[77] H. Steins *et al.*, "A flexible protruding microelectrode array for neural interfacing in bioelectronic medicine," *Microsystems & Nanoengineering,* vol. 8, no. 1, p. 131, 2022/12/22 2022, doi: 10.1038/s41378-022-00466-z.

[78] H. Chong, "DEVELOPMENT OF NOVEL COMPOSITE AND MULTILAYERED MATERIALS FOR PDMS-BASED, MINIMALLY-INVASIVE FLEXIBLE IMPLANTABLE MICROSYSTEMS," Case Western Reserve University, 2022.

[79] G. Schiavone *et al.*, "Soft, implantable bioelectronic interfaces for translational research," *Advanced Materials,* vol. 32, no. 17, p. 1906512, 2020.

[80] M. Golda-Cepa, K. Engvall, M. Hakkarainen, and A. Kotarba, "Recent progress on parylene C polymer for biomedical applications: A review," *Progress in Organic Coatings,* vol. 140, 2020, doi: 10.1016/j.porgcoat.2019.105493.

[81] X. Wang *et al.*, "A Parylene Neural Probe Array for Multi-Region Deep Brain Recordings," *JOURNAL OF MICROELECTROMECHANICAL SYSTEMS,* Article vol. 29, no. 4, pp. 499-513, 2020 AUG 2020, doi: 10.1109/JMEMS.2020.3000235.

[82] C. Cointe *et al.*, "Scalable batch fabrication of ultrathin flexible neural probes using a bioresorbable silk layer," *Microsystems & Nanoengineering,* vol. 8, no. 1, pp. 1-11, 2022.

[83] M. David-Pur, L. Bareket-Keren, G. Beit-Yaakov, D. Raz-Prag, and Y. Hanein, "All-carbon-nanotube flexible multi-electrode array for neuronal recording and stimulation," *Biomedical Microdevices,* vol. 16, no. 1, pp. 43-53, 2014/02/01 2014, doi: 10.1007/s10544-013-9804-6.

[84] Q. Zeng and T. Wu, "Enhanced electrochemical performance of neural electrodes based on PEDOT:PSS hydrogel," *Journal of Applied Polymer Science,* Article vol. 139, no. 13, Apr 5 2022, Art no. e51804, doi: 10.1002/app.51804.

[85] M. Zhu *et al.*, "Flexible Electrodes for In Vivo and In Vitro Electrophysiological Signal Recording," *Adv Healthc Mater,* vol. 10, no. 17, p. e2100646, Sep 2021, doi: 10.1002/adhm.202100646.

[86] T. Niederhoffer, A. Vanhoestenberghe, and H. T. Lancashire, "Methods of poly(3,4)-ethylenedioxithiophene (PEDOT) electrodeposition on metal electrodes for neural stimulation and recording," *Journal of Neural Engineering,* Review vol. 20, no. 1, Feb 1 2023, Art no. 011002, doi: 10.1088/1741-2552/acb084.

[87] S. Seok, "Polymer-Based Biocompatible Packaging for Implantable Devices: Packaging Method, Materials, and Reliability Simulation," *Micromachines (Basel),* vol. 12, no. 9, Aug 27 2021, doi: 10.3390/mi12091020.

[88] S. J. Kim *et al.*, "Evaluation of the biocompatibility of a coating material for an implantable bladder volume sensor," *Kaohsiung J Med Sci,* vol. 28, no. 3, pp. 123-9, Mar 2012, doi: 10.1016/j.kjms.2011.10.016.

[89] K. Shen and M. M. Maharbiz, "Ceramic packaging in neural implants," *J Neural Eng,* vol. 18, no. 2, p. 025002, Feb 24 2021, doi: 10.1088/1741-2552/abd683.

[90] W. Yang, Y. Gong, and W. Li, "A Review: Electrode and Packaging Materials for Neurophysiology Recording Implants," (in English), *Frontiers in Bioengineering and Biotechnology,* Review vol. 8, 2021-January-14 2021, doi: 10.3389/fbioe.2020.622923.

[91] Y. Shi, R. Liu, L. He, H. Feng, Y. Li, and Z. Li, "Recent development of implantable and flexible nerve electrodes," *Smart Materials in Medicine,* vol. 1, pp. 131-147, 2020, doi: 10.1016/j.smaim.2020.08.002.

[92] V. Ramesh *et al.*, "Mechanical Stability of Nano-Coatings on Clinically Applicable Electrodes, Generated by Electrophoretic Deposition," *Advanced Healthcare Materials,* vol. 11, no. 23, p. 2102637, 2022, doi: https://doi.org/10.1002/adhm.202102637.

[93] G. Buzsáki, "Large-scale recording of neuronal ensembles," *Nature neuroscience,* vol. 7, no. 5, pp. 446-451, 2004.

[94] A. Prasad and J. C. Sanchez, "Quantifying long-term microelectrode array functionality using chronic in vivo impedance testing," *Journal of neural engineering,* vol. 9, no. 2, p. 026028, 2012.

[95] D. R. Merrill and P. A. Tresco, "Impedance characterization of microarray recording electrodes in vitro," (in eng), *IEEE Trans Biomed Eng,* vol. 52, no. 11, pp. 1960-5, Nov 2005, doi: 10.1109/tbme.2005.856245.

[96] M. R. Abidian, J. M. Corey, D. R. Kipke, and D. C. Martin, "Conducting‐polymer nanotubes improve electrical properties, mechanical adhesion, neural attachment, and neurite outgrowth of neural electrodes," *small,* vol. 6, no. 3, pp. 421-429, 2010.

[97] J. C. Barrese *et al.*, "Failure mode analysis of silicon-based intracortical microelectrode arrays in non-human primates," *Journal of Neural Engineering,* vol. 10, no. 6, p. 066014, 2013/11/12 2013, doi: 10.1088/1741-2560/10/6/066014.

[98] Y. Qiang *et al.*, "Crosstalk in Polymer Microelectrode Arrays," (in eng), *Nano research,* vol. 14, no. 9, pp. 3240-3247, Sep 2021, doi: 10.1007/s12274-021-3442-8.

[99] M. McNamara, A. Ersoz, and M. Han, "A Diagnostic Circuit for Crosstalk Detection in Microelectrode Arrays," *Int IEEE EMBS Conf Neural Eng,* vol. 2021, pp. 544-547, May 2021, doi: 10.1109/ner49283.2021.9441164.

[100] K. Najafi, J. Ji, and K. Wise, "Scaling limitations of silicon multichannel recording probes," *IEEE transactions on biomedical engineering*, vol. 37, no. 1, pp. 1-11, 1990.

[101] M. F. P. Cruz *et al.*, "Can Crosstalk Compromise the Recording of High-Frequency Neural Signals?," in *9th IEEE/EMBS International Conference on Neural Engineering (NER)*, San Francisco, CA, 2019

Mar 20-23 2019, in International IEEE EMBS Conference on Neural Engineering, 2019, pp. 924-927. [Online]. Available: <Go to ISI>://WOS:000469933200225. [Online]. Available: <Go to ISI>://WOS:000469933200225

[102] V. suresh Vajrala, V. Saunier, L. Nowak, E. Flahaut, C. Bergaud, and A. Maziz, "Carbon Nanofiber/PEDOT Based Macro-Porous Composite for High Performance Multifunctional Neural Microelectrode," *ECS Transactions*, vol. 104, no. 2, p. 3, 2021. [Online]. Available: https://hal.archives-ouvertes.fr/hal-03456618/document.

[103] Y. Luo *et al.*, "Technology roadmap for flexible sensors," *ACS nano*, vol. 17, no. 6, pp. 5211-5295, 2023.

[104] H. RaviPrakash *et al.*, "Deep Learning provides exceptional accuracy to ECoG-based Functional Language Mapping for epilepsy surgery," *Frontiers in Neuroscience*, vol. 14, p. 409, 2020.

[105] E. Boran *et al.*, "High-density ECoG improves the detection of high frequency oscillations that predict seizure outcome," *Clinical Neurophysiology*, vol. 130, no. 10, pp. 1882-1888, 2019.

[106] M. K. Siddiqui, M. Z. Islam, and M. A. Kabir, "A novel quick seizure detection and localization through brain data mining on ECoG dataset," *Neural Computing and Applications*, vol. 31, pp. 5595-5608, 2019.

[107] A. Miyamoto, H. Kawasaki, S. Lee, T. Yokota, M. Amagai, and T. Someya, "Highly Precise, Continuous, Long‐Term Monitoring of Skin Electrical Resistance by Nanomesh Electrodes," *Advanced Healthcare Materials*, vol. 11, no. 10, p. 2102425, 2022.

[108] H. Jang *et al.*, "Graphene e-tattoos for unobstructive ambulatory electrodermal activity sensing on the palm enabled by heterogeneous serpentine ribbons," *Nature Communications*, vol. 13, no. 1, p. 6604, 2022.

[109] Y. Tchoe *et al.*, "Human brain mapping with multithousand-channel PtNRGrids resolves spatiotemporal dynamics," *Science translational medicine*, vol. 14, no. 628, p. eabj1441, 2022.

[110] Y. Ziai *et al.*, "Conducting polymer-based nanostructured materials for brain–machine interfaces," *WIREs Nanomedicine and Nanobiotechnology*, vol. 15, no. 5, p. e1895, 2023, doi: https://doi.org/10.1002/wnan.1895.

[111] Q. Zeng and Z. Huang, "Challenges and Opportunities of Implantable Neural Interfaces: From Material, Electrochemical and Biological Perspectives," *Advanced functional materials,* vol. 33, no. 32, p. 2301223, 2023, doi: https://doi.org/10.1002/adfm.202301223.

[112] E. Otte, A. Vlachos, and M. Asplund, "Engineering strategies towards overcoming bleeding and glial scar formation around neural probes," *Cell Tissue Res,* Jan 14 2022, doi: 10.1007/s00441-021-03567-9.

[113] V. S. Polikov, P. A. Tresco, and W. M. Reichert, "Response of brain tissue to chronically implanted neural electrodes," *Journal of Neuroscience Methods,* vol. 148, no. 1, pp. 1-18, 2005/10/15/ 2005, doi: https://doi.org/10.1016/j.jneumeth.2005.08.015.

[114] N. Wu, S. Wan, S. Su, H. Huang, G. Dou, and L. Sun, "Electrode materials for brain–machine interface: A review," *InfoMat,* vol. 3, no. 11, pp. 1174-1194, 2021, doi: 10.1002/inf2.12234.

[115] M. Polanco, S. Bawab, and H. Yoon, "Computational assessment of neural probe and brain tissue interface under transient motion," *Biosensors,* vol. 6, no. 2, p. 27, 2016.

[116] L. Karumbaiah *et al.*, "The upregulation of specific interleukin (IL) receptor antagonists and paradoxical enhancement of neuronal apoptosis due to electrode induced strain and brain micromotion," *Biomaterials,* vol. 33, no. 26, pp. 5983-5996, 2012.

[117] L. Rao, H. Zhou, T. Li, C. Li, and Y. Y. Duan, "Polyethylene glycol-containing polyurethane hydrogel coatings for improving the biocompatibility of neural electrodes," *Acta biomaterialia,* vol. 8, no. 6, pp. 2233-2242, 2012.

[118] Y. Yang *et al.*, "PPy/SWCNTs-Modified Microelectrode Array for Learning and Memory Model Construction through Electrical Stimulation and Detection of In Vitro Hippocampal Neuronal Network," *ACS Appl Bio Mater,* Article

Early Access vol. 6, no. 9, pp. 3414-3422, Sep 18 2023, doi: 10.1021/acsabm.3c00105.

[119] H. Hwang *et al.*, "Stretchable anisotropic conductive film (S-ACF) for electrical interfacing in high-resolution stretchable circuits," (in eng), *Sci Adv,* vol. 7, no. 32, Aug 2021, doi: 10.1126/sciadv.abh0171.

[120] I. Gablech and E. D. Glowacki, "State-of-the-Art Electronic Materials for Thin Films in Bioelectronics," *Advanced Electronic Materials,* Review; Early Access 2023, doi: 10.1002/aelm.202300258.

[121] C. M. Tringides and D. J. Mooney, "Materials for Implantable Surface Electrode Arrays: Current Status and Future Directions," *Advanced Materials,* Review vol. 34, no. 20, May 2022, Art no. 2107207, doi: 10.1002/adma.202107207.

[122] Y. S. Zhang and A. Khademhosseini, "Advances in engineering hydrogels," (in eng), *Science,* vol. 356, no. 6337, May 5 2017, doi: 10.1126/science.aaf3627.

[123] F. Sun, Z. Xiong, J. Park, and G. Xu, "Close-Packed PEDOT: PSS-Coated Graphene Microelectrodes for High-Resolution Interrogation of Neural Activity," *IEEE Transactions on Electron Devices,* vol. 68, no. 6, pp. 3080-3086, 2021.

[124] E. He *et al.*, "SWCNTs/PEDOT:PSS-Modified Microelectrode Arrays for Dual-Mode Detection of Electrophysiological Signals and Dopamine Concentration in the Striatum under Isoflurane Anesthesia," (in eng), *ACS sensors,* vol. 6, no. 9, pp. 3377-3386, Sep 24 2021, doi: 10.1021/acssensors.1c01241.

[125] M. Shih, C.-T. Kuo, M.-H. Lin, Y.-J. Chuang, H. Chen, and T.-R. Yew, "A 3D-CNT micro-electrode array for zebrafish ECG study including directionality measurement and drug test," *Biocybernetics and Biomedical Engineering,* vol. 40, no. 2, pp. 701-708, 2020/04/01/ 2020, doi: https://doi.org/10.1016/j.bbe.2020.02.008.

[126] P. Kshirsagar *et al.*, "Transparent Graphene/PEDOT: PSS microelectrodes for electro‐and optophysiology," *Advanced Materials Technologies,* vol. 4, no. 1, p. 1800318, 2019.

[127] S.-W. Park *et al.*, "Epidural Electrotherapy for Epilepsy," *Small,* vol. 14, no. 30, p. 1801732, 2018, doi: https://doi.org/10.1002/smll.201801732.

[128] G. Li *et al.*, "Highly Conducting and Stretchable Double-Network Hydrogel for Soft Bioelectronics," *Advanced Materials,* vol. 34, no. 15, p. 2200261, 2022, doi: https://doi.org/10.1002/adma.202200261.

[129] R. Dong *et al.*, "Highly Stretchable Metal–Polymer Conductor Electrode Array for Electrophysiology," *Advanced healthcare materials,* vol. 10, no. 4, p. 2000641, 2021.

[130] M. K. Kim, J. C. Leong, Y. Jo, G. Kook, and H. J. Lee, "Multimodal Neural Probes with Small Form Factor Based on Dual-Side Fabrication," *Advanced Materials Technologies,* Article vol. 8, no. 2, Jan 2023, doi: 10.1002/admt.202200692.

[131] Z. H. Xiang *et al.*, "High-density stretchable microelectrode array based on multilayer serpentine interconnections," (in English), *Journal of Micromechanics and Microengineering,* Article vol. 32, no. 8, p. 9, Aug 2022, Art no. 084002, doi: 10.1088/1361-6439/ac799d.

[132] B. Ji *et al.*, "Stretchable Parylene-C electrodes enabled by serpentine structures on arbitrary elastomers by silicone rubber adhesive," *JOURNAL OF MATERIOMICS,* Article vol. 6, no. 2, pp. 330-338, 2020 JUN 2020, doi: 10.1016/j.jmat.2019.11.006.

[133] F. Hempel *et al.*, "PEDOT:PSS organic electrochemical transistor arrays for extracellular electrophysiological sensing of cardiac cells," *Biosensors & Bioelectronics,* vol. 93, pp. 132-138, Jul 2017, doi: 10.1016/j.bios.2016.09.047.

[134] M. Bianchi *et al.*, "Conductive Polymers for Bidirectional Neural Interfaces: Fundamentals Aspects and in Vivo Applications," TechRxiv, 2021.

[135] H. R. Barai, A. N. Banerjee, F. Bai, and S. W. Joo, "Surface modification of titania nanotube arrays with crystalline manganese-oxide nanostructures and fabrication of hybrid electrochemical electrode for high-performance supercapacitors," *Journal of Industrial and Engineering Chemistry*, Article vol. 62, pp. 409-417, Jun 25 2018, doi: 10.1016/j.jiec.2018.01.023.

[136] P. Fattahi, G. Yang, G. Kim, and M. R. Abidian, "A review of organic and inorganic biomaterials for neural interfaces," *Advanced materials*, vol. 26, no. 12, pp. 1846-1885, 2014.

[137] A. Golabchi, K. M. Woeppel, X. Li, C. F. Lagenaur, and X. T. Cui, "Neuroadhesive protein coating improves the chronic performance of neuroelectronics in mouse brain," *Biosensors & bioelectronics*, vol. 155, p. 112096, May 1 2020, doi: 10.1016/j.bios.2020.112096.

[138] F. Vitale *et al.*, "Biomimetic extracellular matrix coatings improve the chronic biocompatibility of microfabricated subdural microelectrode arrays," (in eng), *PloS one*, vol. 13, no. 11, p. e0206137, 2018, doi: 10.1371/journal.pone.0206137.

[139] W. Yang *et al.*, "A fully transparent, flexible PEDOT:PSS-ITO-Ag-ITO based microelectrode array for ECoG recording," *LAB ON A CHIP*, Article vol. 21, no. 6, pp. 1096-1108, 2021 MAR 21 2021, doi: 10.1039/d0lc01123a.

[140] N. Shmoel, N. Rabieh, S. M. Ojovan, H. Erez, E. Maydan, and M. E. Spira, "Multisite electrophysiological recordings by self-assembled loose-patch-like junctions between cultured hippocampal neurons and mushroom-shaped microelectrodes," *Scientific Reports*, vol. 6, no. 1, p. 27110, 2016/06/03 2016, doi: 10.1038/srep27110.

[141] D. Shi, V. Dhawan, and X. T. Cui, "Bio-integrative design of the neural tissue-device interface," (in eng), *Current opinion in biotechnology*, vol. 72, pp. 54-61, Dec 2021, doi: 10.1016/j.copbio.2021.10.003.

[142] C. Dagdeviren *et al.*, "Conformal piezoelectric energy harvesting and storage from motions of the heart, lung, and diaphragm," *Proceedings of the National Academy of Sciences*, vol. 111, no. 5, pp. 1927-1932, 2014.

[143] M. Kang *et al.*, "Wireless graphene-based thermal patch for obtaining temperature distribution and performing thermography," *Science advances*, vol. 8, no. 15, p. eabm6693, 2022.

[144] E. Song *et al.*, "Flexible electronic/optoelectronic microsystems with scalable designs for chronic biointegration," *Proceedings of the National Academy of Sciences*, vol. 116, no. 31, pp. 15398-15406, 2019.

[145] Y. Zhang *et al.*, "Highly stable flexible pressure sensors with a quasi-homogeneous composition and interlinked interfaces," *Nature communications*, vol. 13, no. 1, p. 1317, 2022.

[146] S. Pimenta *et al.*, "Double-Layer Flexible Neural Probe With Closely Spaced Electrodes for High-Density in vivo Brain Recordings," *Frontiers in neuroscience*, vol. 15, p. 663174, 2021, doi: 10.3389/fnins.2021.663174.

[147] M. K. Kim, J. C. Leong, Y. Jo, G. Kook, and H. J. Lee, "Multimodal Neural Probes with Small Form Factor Based on Dual-Side Fabrication," *Advanced Materials Technologies*, vol. 8, no. 2, p. 2200692, 2023, doi: https://doi.org/10.1002/admt.202200692.

[148] S. Pimenta *et al.*, "Double-Layer Flexible Neural Probe With Closely Spaced Electrodes for High-Density in vivo Brain Recordings," (in English), *Frontiers in Neuroscience*, Original Research vol. 15, 2021-June-15 2021, doi: 10.3389/fnins.2021.663174.

[149] A. Tooker *et al.*, "Polymer neural interface with dual-sided electrodes for neural stimulation and recording," in *2012 Annual International Conference of the IEEE Engineering in Medicine and Biology Society*, 28 Aug.-1 Sept. 2012 2012, pp. 5999-6002, doi: 10.1109/EMBC.2012.6347361.

[150] T. Dotan *et al.*, "Soft and flexible gold microelectrodes by supersonic cluster beam deposition and femtosecond laser processing," *Microelectronic Engineering*, vol. 237, p. 111478, 2021/01/15/ 2021, doi: https://doi.org/10.1016/j.mee.2020.111478.

[151] Y. Kim, S. Alimperti, P. Choi, and M. Noh, "An Inkjet Printed Flexible Electrocorticography (ECoG) Microelectrode Array on a Thin Parylene-C Film," *Sensors*, vol. 22, no. 3, p. 1277, 2022.

[152] J. S. Mandelli, J. Koepp, A. Hama, S. Sanaur, G. A. Rae, and C. R. Rambo, "Cell viability and cytotoxicity of inkjet-printed flexible organic electrodes on parylene C," *Biomedical Microdevices*, vol. 23, pp. 1-12, 2021.

[153] J. Naughton *et al.*, "Suppression of crosstalk in multielectrode arrays with local shielding," *Frontiers in Nanotechnology*, vol. 4, p. 948337, 2022.

[154] M. S. Saleh *et al.*, "CMU Array: A 3D nanoprinted, fully customizable high-density microelectrode array platform," *Science Advances*, vol. 8, no. 40, p. eabj4853, 2022.

[155] H. Shin, S. Jeong, J.-H. Lee, W. Sun, N. Choi, and I.-J. Cho, "3D high-density microelectrode array with optical stimulation and drug delivery for investigating neural circuit dynamics," *Nature communications*, vol. 12, no. 1, pp. 1-18, 2021.

[156] B. Miccoli *et al.*, "High-density electrical recording and impedance imaging with a multi-modal CMOS multi-electrode array chip," *Frontiers in neuroscience*, vol. 13, p. 641, 2019.

[157] S. Sundaram, P. Kellnhofer, Y. Li, J.-Y. Zhu, A. Torralba, and W. Matusik, "Learning the signatures of the human grasp using a scalable tactile glove," *Nature*, vol. 569, no. 7758, pp. 698-702, 2019.

[158] Y. J. Park *et al.*, "All MoS2-based large area, skin-attachable active-matrix tactile sensor," *ACS nano*, vol. 13, no. 3, pp. 3023-3030, 2019.

[159] G. Gwon *et al.*, "An All-Nanofiber-Based Substrate-Less, Extremely Conformal, and Breathable Organic Field Effect Transistor for Biomedical Applications," *Advanced Functional Materials*, vol. 32, no. 35, p. 2204645, 2022.

[160] M. Brofiga *et al.*, "Multiple neuron clusters on Micro-Electrode Arrays as an in vitro model of brain network," *Scientific Reports*, vol. 13, no. 1, p. 15604, 2023/09/20 2023, doi: 10.1038/s41598-023-42168-0.

[161] G. Quadrato *et al.*, "Cell diversity and network dynamics in photosensitive human brain organoids," *Nature*, vol. 545, no. 7652, pp. 48-53, 2017. [Online]. Available: https://www.ncbi.nlm.nih.gov/pmc/articles/PMC5659341/pdf/nihms907542.pdf.

[162] C. A. Trujillo *et al.*, "Complex oscillatory waves emerging from cortical organoids model early human brain network development," *Cell stem cell*, vol. 25, no. 4, pp. 558-569. e7, 2019. [Online]. Available: https://www.cell.com/cell-stem-cell/pdf/S1934-5909(19)30337-6.pdf.

[163] T. Sharf *et al.*, "Intrinsic network activity in human brain organoids," *Available at SSRN 3797268*, 2021.

[164] K. Tasnim and J. Liu, "Emerging Bioelectronics for Brain Organoid Electrophysiology," *J Mol Biol*, vol. 434, no. 3, p. 167165, Feb 15 2022, doi: 10.1016/j.jmb.2021.167165.

[165] A. Farnum *et al.*, "Harnessing insect olfactory neural circuits for detecting and discriminating human cancers," *Biosens Bioelectron*, vol. 219, p. 114814, Oct 15 2022, doi: 10.1016/j.bios.2022.114814.

[166] Y. Gong, X. Liu, Y. Liu, Z. Qiu, A. Weber, and W. Li, "A Flexible Origami Opto-Electro Array For In Vivo Optogenetic Neurostimulation and Neurophysiology Recording," in *2024 IEEE 37th International Conference on Micro Electro Mechanical Systems (MEMS)*, 21-25 Jan. 2024 2024, pp. 240-244, doi: 10.1109/MEMS58180.2024.10439312.

[167] Z. Zhao *et al.*, "Ultraflexible electrode arrays for months-long high-density electrophysiological mapping of thousands of neurons in rodents," *Nature Biomedical Engineering*, vol. 7, no. 4, pp. 520-532, 2023/04/01 2023, doi: 10.1038/s41551-022-00941-y.

[168] Z. Jiang, M. Zhu, and X. Chen, "Interfacing Neuron-Motor Pathways with Stretchable and Biocompatible Electrode Arrays," *Accounts of Chemical Research*, vol. 57, no. 16, pp. 2255-2266, 2024/08/20 2024, doi: 10.1021/acs.accounts.4c00215.

[169] C.-H. Chiang *et al.*, "A modular high-density μECoG system on macaque vlPFC for auditory cognitive decoding," *Journal of neural engineering*, vol. 17, no. 4, p. 046008, 2020. [Online]. Available: https://www.ncbi.nlm.nih.gov/pmc/articles/PMC7906089/pdf/nihms-1666224.pdf.

[170] Y. Tian *et al.*, "An Ultraflexible Electrode Array for Large-Scale Chronic Recording in the Nonhuman Primate Brain," *Advanced Science*, vol. 10, no. 33, p. 2302333, 2023.

[171] A. C. Paulk *et al.*, "Microscale Physiological Events on the Human Cortical Surface," *Cerebral Cortex*, Article vol. 31, no. 8, pp. 3678-3700, Aug 2021, doi: 10.1093/cercor/bhab040.

[172] J. Sun *et al.*, "Intraoperative microseizure detection using a high-density micro-electrocorticography electrode array," *Brain Communications*, Article vol. 4, no. 3, May 2 2022, Art no. fcac122, doi: 10.1093/braincomms/fcac122.

[173] J. C. Yang *et al.*, "Microscale dynamics of electrophysiological markers of epilepsy," *Clin. Neurophysiol.*, Article vol. 132, no. 11, pp. 2916-2931, 2021 NOV 2021, doi: 10.1016/j.clinph.2021.06.024.

[174] E. Moreno, M. José Corriale, and A. Arenas, "Differences in olfactory sensitivity and odor detection correlate with foraging task specialization in honeybees Apis mellifera," *Journal of Insect Physiology*, vol. 141, p. 104416, 2022/08/01/ 2022, doi: https://doi.org/10.1016/j.jinsphys.2022.104416.

[175] J. Reinhard, M. Sinclair, M. V. Srinivasan, and C. Claudianos, "Honeybees Learn Odour Mixtures via a Selection of Key Odorants," *PLOS ONE*, vol. 5, no. 2, p. e9110, 2010, doi: 10.1371/journal.pone.0009110.

[176] J.-C. Sandoz, "Behavioral and Neurophysiological Study of Olfactory Perception and Learning in Honeybees," (in English), *Frontiers in Systems Neuroscience*, Review vol. 5, 2011-December-08 2011, doi: 10.3389/fnsys.2011.00098.

[177] D. Saha, K. Leong, C. Li, S. Peterson, G. Siegel, and B. Raman, "A spatiotemporal coding mechanism for background-invariant odor recognition," *Nat Neurosci*, vol. 16, no. 12, pp. 1830-9, Dec 2013, doi: 10.1038/nn.3570.

[178] D. Saha *et al.*, "Explosive sensing with insect-based biorobots," *Biosensors and Bioelectronics: X*, vol. 6, p. 100050, 2020/12/01/ 2020, doi: https://doi.org/10.1016/j.biosx.2020.100050.

[179] M. Stopfer, V. Jayaraman, and G. Laurent, "Intensity versus identity coding in an olfactory system," *Neuron,* vol. 39, no. 6, pp. 991-1004, 2003.

[180] B. M. Broome, V. Jayaraman, and G. Laurent, "Encoding and Decoding of Overlapping Odor Sequences," *Neuron,* vol. 51, no. 4, pp. 467-482, 2006, doi: 10.1016/j.neuron.2006.07.018.

[181] D. Saha, K. Leong, C. Li, S. Peterson, G. Siegel, and B. Raman, "A spatiotemporal coding mechanism for background-invariant odor recognition," *Nature Neuroscience,* vol. 16, no. 12, pp. 1830-1839, 2013/12/01 2013, doi: 10.1038/nn.3570.

[182] S. Nizampatnam, D. Saha, R. Chandak, and B. Raman, "Dynamic contrast enhancement and flexible odor codes," *Nature Communications,* vol. 9, no. 1, p. 3062, 2018/08/03 2018, doi: 10.1038/s41467-018-05533-6.

[183] M. H. Y. Hu *et al.*, "Spontaneous Epileptic Recordings from hiPSC-Derived Cortical Neurons Cultured with a Human Epileptic Brain Biopsy on a Multi Electrode Array," *Applied Sciences,* vol. 13, no. 3, p. 1432, 2023. [Online]. Available: https://www.mdpi.com/2076-3417/13/3/1432.

[184] H. Tichy, A. Martzok, M. Linhart, L. M. Zopf, and M. Hellwig, "Multielectrode recordings of cockroach antennal lobe neurons in response to temporal dynamics of odor concentrations," *Journal of Comparative Physiology A,* pp. 1-26, 2023.

[185] M. J. Beetz, C. Kraus, and B. El Jundi, "Neural representation of goal direction in the monarch butterfly brain," *Nature Communications,* vol. 14, no. 1, p. 5859, 2023.

[186] J. E. Chung *et al.*, "High-density single-unit human cortical recordings using the Neuropixels probe," (in English), *Neuron,* vol. 110, no. 15, pp. 2409-+, Aug 3 2022, doi: 10.1016/j.neuron.2022.05.007.

[187] X. Liu, Y. Gong, Z. Jiang, T. Stevens, and W. Li, "Flexible high-density microelectrode arrays for closed-loop brain–machine interfaces: a review," (in English), *Frontiers in Neuroscience,* Review vol. 18, 2024-April-15 2024, doi: 10.3389/fnins.2024.1348434.

[188] A. Chari, R. C. Thornton, M. M. Tisdall, and R. C. Scott, "Microelectrode recordings in human epilepsy: a case for clinical translation," *Brain Communications,* Review vol. 2, no. 2, 2020 2020, Art no. 82, doi: 10.1093/braincomms/fcaa082.

[189] Z. J. Sperry *et al.*, "High-density neural recordings from feline sacral dorsal root ganglia with thin-film array," *Journal of Neural Engineering,* Article vol. 18, no. 4, Aug 2021, Art no. 046005, doi: 10.1088/1741-2552/abe398.

[190] X. R. Li *et al.*, "Flexible Electrocorticography Electrode Array for Epileptiform Electrical Activity Recording under Glutamate and GABA Modulation on the Primary

Somatosensory Cortex of Rats," *Micromachines,* vol. 11, no. 8, Aug 2020, Art no. 732, doi: 10.3390/mi11080732.

[191] L. Q. Xu *et al.*, "Trends and recent development of the microelectrode arrays (MEAs)," (in English), *Biosensors & Bioelectronics,* Article vol. 175, p. 15, Mar 2021, Art no. 112854, doi: 10.1016/j.bios.2020.112854.

[192] B. Zhang *et al.*, "Implantable neural electrodes: from preparation optimization to application," *J. Mater. Chem. C,* Review vol. 11, no. 20, pp. 6550-6572, May 25 2023, doi: 10.1039/d2tc05162a.

[193] Q. Zeng and Z. L. Huang, "Challenges and Opportunities of Implantable Neural Interfaces: From Material, Electrochemical and Biological Perspectives," *Advanced Functional Materials,* 2023 Jun 2023, doi: 10.1002/adfm.202301223.

[194] J. P. Harris *et al.*, "Mechanically adaptive intracortical implants improve the proximity of neuronal cell bodies," (in eng), *J Neural Eng,* vol. 8, no. 6, p. 066011, Dec 2011, doi: 10.1088/1741-2560/8/6/066011.

[195] Z. Guo *et al.*, "A flexible neural implant with ultrathin substrate for low-invasive brain-computer interface applications," *Microsystems & Nanoengineering,* Article vol. 8, no. 1, Dec 25 2022, Art no. 133, doi: 10.1038/s41378-022-00464-1.

[196] K. Scholten and E. Meng, "Electron-beam lithography for polymer bioMEMS with submicron features," *Microsystems & nanoengineering,* vol. 2, no. 1, pp. 1-7, 2016.

[197] X. Wei *et al.*, "Nanofabricated Ultraflexible Electrode Arrays for High-Density Intracortical Recording," *Adv Sci (Weinh),* vol. 5, no. 6, p. 1700625, Jun 2018, doi: 10.1002/advs.201700625.

[198] T. Stieglitz, "Flexible biomedical microdevices with double-sided electrode arrangements for neural applications," *SENSORS AND ACTUATORS A-PHYSICAL,* Article vol. 90, no. 3, pp. 203-211, 2001 MAY 20 2001, doi: 10.1016/S0924-4247(01)00520-9.

[199] M. Mueller, C. Boehler, J. Jaeger, M. Asplund, and T. Stieglitz, "A Double-Sided Fabrication Process for Intrafascicular Parylene C Based Electrode Arrays," (in English), *Ieee Eng Med Bio,* pp. 2798-2801, 2016. [Online]. Available: <Go to ISI>://WOS:000399823503040.

[200] W. Poppendieck *et al.*, "Development, manufacturing and application of double-sided flexible implantable microelectrodes," *Biomedical Microdevices,* vol. 16, no. 6, pp. 837-850, 2014/12/01 2014, doi: 10.1007/s10544-014-9887-8.

[201] N. A. A. Shahrim, Z. Ahmad, A. Wong Azman, Y. Fachmi Buys, and N. Sarifuddin, "Mechanisms for doped PEDOT:PSS electrical conductivity improvement," *Materials*

Advances, 10.1039/D1MA00290B vol. 2, no. 22, pp. 7118-7138, 2021, doi: 10.1039/D1MA00290B.

[202] W. Li, Y. Li, Z. Song, Y.-X. Wang, and W. Hu, "PEDOT-based stretchable optoelectronic materials and devices for bioelectronic interfaces," *Chemical Society Reviews*, 10.1039/D4CS00541D vol. 53, no. 21, pp. 10575-10603, 2024, doi: 10.1039/D4CS00541D.

[203] G. Li and C. F. Guo, "PEDOT:PSS-based intrinsically soft and stretchable bioelectronics," *Soft Science*, vol. 2, no. 2, p. 7, 2022. [Online]. Available: https://www.oaepublish.com/articles/ss.2022.07.

[204] G. E. Fenoy, O. Azzaroni, W. Knoll, and W. A. Marmisollé, "Functionalization Strategies of PEDOT and PEDOT:PSS Films for Organic Bioelectronics Applications," *Chemosensors*, vol. 9, no. 8, p. 212, 2021. [Online]. Available: https://www.mdpi.com/2227-9040/9/8/212.

[205] Y. Yang, H. Deng, and Q. Fu, "Recent progress on PEDOT:PSS based polymer blends and composites for flexible electronics and thermoelectric devices," *Materials Chemistry Frontiers*, 10.1039/D0QM00308E vol. 4, no. 11, pp. 3130-3152, 2020, doi: 10.1039/D0QM00308E.

[206] L. T. Tran, H. V. Tran, H. H. Cao, T. H. Tran, and C. D. Huynh, "Electrochemically Effective Surface Area of a Polyaniline Nanowire-Based Platinum Microelectrode and Development of an Electrochemical DNA Sensor," *Journal of Nanotechnology*, vol. 2022, p. 8947080, 2022/05/17 2022, doi: 10.1155/2022/8947080.

[207] R. Trouillon, Y. Lin, L. J. Mellander, J. D. Keighron, and A. G. Ewing, "Evaluating the diffusion coefficient of dopamine at the cell surface during amperometric detection: disk vs ring microelectrodes," (in eng), *Anal Chem*, vol. 85, no. 13, pp. 6421-8, Jul 2 2013, doi: 10.1021/ac400965d.

[208] S. J. Cartamil-Bueno, P. G. Steeneken, A. Centeno, A. Zurutuza, H. S. J. van der Zant, and S. Houri, "Colorimetry Technique for Scalable Characterization of Suspended Graphene," *Nano Letters*, vol. 16, no. 11, pp. 6792-6796, 2016/11/09 2016, doi: 10.1021/acs.nanolett.6b02416.

[209] V. Castagnola, C. Bayon, E. Descamps, and C. Bergaud, "Morphology and conductivity of PEDOT layers produced by different electrochemical routes," *Synth. Met.*, vol. 189, pp. 7-16, 2014/03/01/ 2014, doi: https://doi.org/10.1016/j.synthmet.2013.12.013.

[210] V. Castagnola *et al.*, "Parylene-based flexible neural probes with PEDOT coated surface for brain stimulation and recording," *Biosensors and Bioelectronics*, vol. 67, pp. 450-457, 2015.

[211] A. S. Pranti, A. Schander, A. Bödecker, and W. Lang, "PEDOT: PSS coating on gold microelectrodes with excellent stability and high charge injection capacity for chronic neural interfaces," *Sensors and Actuators B: Chemical*, vol. 275, pp. 382-393, 2018, doi: 10.1016/j.snb.2018.08.007.

[212] A. S. Pranti, A. Schander, A. Bödecker, and W. Lang, "Highly Stable PEDOT:PSS Coating on Gold Microelectrodes with Improved Charge Injection Capacity for Chronic Neural Stimulation," *Proceedings*, vol. 1, no. 4, p. 492, 2017. [Online]. Available: https://www.mdpi.com/2504-3900/1/4/492.

[213] Y. Lu, H. Lyu, A. G. Richardson, T. H. Lucas, and D. Kuzum, "Flexible Neural Electrode Array Based-on Porous Graphene for Cortical Microstimulation and Sensing," *Scientific Reports*, vol. 6, no. 1, p. 33526, 2016/09/19 2016, doi: 10.1038/srep33526.

[214] I. W. Sun and J.-K. Chang, "Electrodeposition of Nanomaterials," in *Springer Handbook of Electrochemical Energy*, C. Breitkopf and K. Swider-Lyons Eds. Berlin, Heidelberg: Springer Berlin Heidelberg, 2017, pp. 835-895.

[215] H. Mousavi, L. M. Ferrari, A. Whiteley, and E. Ismailova, "Kinetics and Physicochemical Characteristics of Electrodeposited PEDOT:PSS Thin Film Growth," *Advanced Electronic Materials*, vol. 9, no. 9, p. 2201282, 2023, doi: https://doi.org/10.1002/aelm.202201282.

[216] D. Khodagholy *et al.*, "NeuroGrid: recording action potentials from the surface of the brain," *Nature Neuroscience*, vol. 18, no. 2, pp. 310-315, 2015/02/01 2015, doi: 10.1038/nn.3905.

[217] G. Mulberry, K. A. White, M. A. Crocker, and B. N. Kim, "A 512-Ch Dual-Mode Microchip for Simultaneous Measurements of Electrophysiological and Neurochemical Activities," *BIOSENSORS-BASEL*, Article vol. 13, no. 5, 2023 APR 26 2023, Art no. 502, doi: 10.3390/bios13050502.

[218] M. Oudkerk, S. Liu, M. A. Heuvelmans, J. E. Walter, and J. K. Field, "Lung cancer LDCT screening and mortality reduction — evidence, pitfalls and future perspectives," *Nature Reviews Clinical Oncology*, vol. 18, no. 3, pp. 135-151, 2021/03/01 2021, doi: 10.1038/s41571-020-00432-6.

[219] D. R. Baldwin and M. E. J. Callister, "What is the Optimum Screening Strategy for the Early Detection of Lung Cancer," *Clinical Oncology*, vol. 28, no. 11, pp. 672-681, 2016/11/01/ 2016, doi: https://doi.org/10.1016/j.clon.2016.08.001.

[220] M. Shirasu and K. Touhara, "The scent of disease: volatile organic compounds of the human body related to disease and disorder," (in eng), *J Biochem*, vol. 150, no. 3, pp. 257-66, Sep 2011, doi: 10.1093/jb/mvr090.

[221] C. G. Waltman, T. A. T. Marcelissen, and J. G. H. van Roermund, "Exhaled-breath Testing for Prostate Cancer Based on Volatile Organic Compound Profiling Using an

Electronic Nose Device (Aeonose™): A Preliminary Report," (in eng), *Eur Urol Focus,* vol. 6, no. 6, pp. 1220-1225, Nov 15 2020, doi: 10.1016/j.euf.2018.11.006.

[222] H. Haick, Y. Y. Broza, P. Mochalski, V. Ruzsanyi, and A. Amann, "Assessment, origin, and implementation of breath volatile cancer markers," (in eng), *Chem Soc Rev,* vol. 43, no. 5, pp. 1423-49, Mar 7 2014, doi: 10.1039/c3cs60329f.

[223] W. Filipiak *et al.*, "Comparative analyses of volatile organic compounds (VOCs) from patients, tumors and transformed cell lines for the validation of lung cancer-derived breath markers," (in eng), *J Breath Res,* vol. 8, no. 2, p. 027111, Jun 2014, doi: 10.1088/1752-7155/8/2/027111.

[224] N. Queralto, A. N. Berliner, B. Goldsmith, R. Martino, P. Rhodes, and S. H. Lim, "Detecting cancer by breath volatile organic compound analysis: a review of array-based sensors," (in eng), *J Breath Res,* vol. 8, no. 2, p. 027112, Jun 2014, doi: 10.1088/1752-7155/8/2/027112.

[225] B. R. B. da Costa and B. S. De Martinis, "Analysis of urinary VOCs using mass spectrometric methods to diagnose cancer: A review," (in eng), *Clin Mass Spectrom,* vol. 18, pp. 27-37, Nov 2020, doi: 10.1016/j.clinms.2020.10.004.

[226] S. Sethi, R. Nanda, and T. Chakraborty, "Clinical application of volatile organic compound analysis for detecting infectious diseases," (in eng), *Clin Microbiol Rev,* vol. 26, no. 3, pp. 462-75, Jul 2013, doi: 10.1128/cmr.00020-13.

[227] R. P. Arasaradnam *et al.*, "Detection of Colorectal Cancer (CRC) by Urinary Volatile Organic Compound Analysis," *PLOS ONE,* vol. 9, no. 9, p. e108750, 2014, doi: 10.1371/journal.pone.0108750.

[228] R. P. Arasaradnam, A. Wicaksono, H. O'Brien, H. M. Kocher, J. A. Covington, and T. Crnogorac-Jurcevic, "Noninvasive Diagnosis of Pancreatic Cancer Through Detection of Volatile Organic Compounds in Urine," *Gastroenterology,* vol. 154, no. 3, pp. 485-487.e1, 2018, doi: 10.1053/j.gastro.2017.09.054.

[229] R. J. Niemi, A. N. Roine, E. Eräviita, P. S. Kumpulainen, J. U. Mäenpää, and N. Oksala, "FAIMS analysis of urine gaseous headspace is capable of differentiating ovarian cancer," *Gynecologic Oncology,* vol. 151, no. 3, pp. 519-524, 2018/12/01/ 2018, doi: https://doi.org/10.1016/j.ygyno.2018.09.016.

[230] N. Peled *et al.*, "Volatile fingerprints of cancer specific genetic mutations," *Nanomedicine: Nanotechnology, Biology and Medicine,* vol. 9, no. 6, pp. 758-766, 2013, doi: 10.1016/j.nano.2013.01.008.

[231] M. P. Davies *et al.*, "Unique volatolomic signatures of TP53 and KRAS in lung cells," (in eng), *Br J Cancer,* vol. 111, no. 6, pp. 1213-21, Sep 9 2014, doi: 10.1038/bjc.2014.411.

[232] Z. Jia *et al.*, "Detection of Lung Cancer: Concomitant Volatile Organic Compounds and Metabolomic Profiling of Six Cancer Cell Lines of Different Histological Origins," *ACS Omega,* vol. 3, no. 5, pp. 5131-5140, May 31 2018, doi: 10.1021/acsomega.7b02035.

[233] M. Serasanambati, Y. Y. Broza, A. Marmur, and H. Haick, "Profiling Single Cancer Cells with Volatolomics Approach," *iScience,* vol. 11, pp. 178-188, 2019, doi: 10.1016/j.isci.2018.12.008.

[234] R. Thriumani *et al.*, "A study on volatile organic compounds emitted by in-vitro lung cancer cultured cells using gas sensor array and SPME-GCMS," *BMC Cancer,* vol. 18, no. 1, p. 362, Apr 2 2018, doi: 10.1186/s12885-018-4235-7.

[235] E. Janssens *et al.*, "Headspace Volatile Organic Compound Profiling of Pleural Mesothelioma and Lung Cancer Cell Lines as Translational Bridge for Breath Research," (in English), *Frontiers in Oncology,* Original Research vol. 12, 2022-May-06 2022, doi: 10.3389/fonc.2022.851785.

[236] L. Lavra *et al.*, "Investigation of VOCs associated with different characteristics of breast cancer cells," *Scientific Reports,* vol. 5, no. 1, p. 13246, 2015/08/25 2015, doi: 10.1038/srep13246.

[237] H. Tang, Y. Lu, L. Zhang, Z. Wu, X. Hou, and H. Xia, "Determination of volatile organic compounds exhaled by cell lines derived from hematological malignancies," (in eng), *Biosci Rep,* vol. 37, no. 3, Jun 30 2017, doi: 10.1042/bsr20170106.

[238] A. R. Lima *et al.*, "Discrimination between the human prostate normal and cancer cell exometabolome by GC-MS," *Scientific Reports,* vol. 8, no. 1, 2018, doi: 10.1038/s41598-018-23847-9.

[239] T. Saidi *et al.*, "Non-invasive prediction of lung cancer histological types through exhaled breath analysis by UV-irradiated electronic nose and GC/QTOF/MS," *Sensors and Actuators B: Chemical,* vol. 311, p. 127932, 2020/05/15/ 2020, doi: https://doi.org/10.1016/j.snb.2020.127932.

[240] F. Gouzerh, J.-M. Bessière, B. Ujvari, F. Thomas, A. M. Dujon, and L. Dormont, "Odors and cancer: Current status and future directions," *Biochimica et Biophysica Acta (BBA) - Reviews on Cancer,* vol. 1877, no. 1, p. 188644, 2022/01/01/ 2022, doi: https://doi.org/10.1016/j.bbcan.2021.188644.

[241] P. Fuchs, C. Loeseken, J. K. Schubert, and W. Miekisch, "Breath gas aldehydes as biomarkers of lung cancer," *International Journal of Cancer,* vol. 126, no. 11, pp. 2663-2670, 2010, doi: https://doi.org/10.1002/ijc.24970.

[242] M. Hakim *et al.*, "Diagnosis of head-and-neck cancer from exhaled breath," *Br J Cancer,* vol. 104, no. 10, pp. 1649-55, May 10 2011, doi: 10.1038/bjc.2011.128.

[243] I. Nardi-Agmon and N. Peled, "Exhaled breath analysis for the early detection of lung cancer: recent developments and future prospects," *Lung Cancer: Targets and Therapy*, vol. 8, no. null, pp. 31-38, 2017/05/17 2017, doi: 10.2147/LCTT.S104205.

[244] G. Peng *et al.*, "Detection of lung, breast, colorectal, and prostate cancers from exhaled breath using a single array of nanosensors," *British Journal of Cancer*, vol. 103, no. 4, pp. 542-551, 2010/08/01 2010, doi: 10.1038/sj.bjc.6605810.

[245] M. Phillips *et al.*, "Volatile markers of breast cancer in the breath," *Breast J*, vol. 9, no. 3, pp. 184-91, May-Jun 2003, doi: 10.1046/j.1524-4741.2003.09309.x.

[246] M. Phillips *et al.*, "Prediction of breast cancer using volatile biomarkers in the breath," *Breast Cancer Res Treat*, vol. 99, no. 1, pp. 19-21, Sep 2006, doi: 10.1007/s10549-006-9176-1.

[247] F. Raspagliesi, G. Bogani, S. Benedetti, S. Grassi, S. Ferla, and S. Buratti, "Detection of Ovarian Cancer through Exhaled Breath by Electronic Nose: A Prospective Study," *Cancers*, vol. 12, no. 9, p. 2408, 2020, doi: 10.3390/cancers12092408.

[248] A. Roine *et al.*, "Detection of prostate cancer by an electronic nose: a proof of principle study," *J Urol*, vol. 192, no. 1, pp. 230-4, Jul 2014, doi: 10.1016/j.juro.2014.01.113.

[249] J. Pereira *et al.*, "Breath Analysis as a Potential and Non-Invasive Frontier in Disease Diagnosis: An Overview," *Metabolites*, vol. 5, no. 1, pp. 3-55, 2015, doi: 10.3390/metabo5010003.

[250] J. Li *et al.*, "Investigation of potential breath biomarkers for the early diagnosis of breast cancer using gas chromatography-mass spectrometry," *Clin Chim Acta*, vol. 436, pp. 59-67, Sep 25 2014, doi: 10.1016/j.cca.2014.04.030.

[251] M. Kaloumenou, E. Skotadis, N. Lagopati, E. Efstathopoulos, and D. Tsoukalas, "Breath Analysis: A Promising Tool for Disease Diagnosis—The Role of Sensors," *Sensors*, vol. 22, no. 3, p. 1238, 2022. [Online]. Available: https://www.mdpi.com/1424-8220/22/3/1238.

[252] C. Brunner *et al.*, "Discrimination of cancerous and non-cancerous cell lines by headspace-analysis with PTR-MS," *Analytical and Bioanalytical Chemistry*, vol. 397, no. 6, pp. 2315-2324, 2010, doi: 10.1007/s00216-010-3838-x.

[253] D. F. Altomare *et al.*, "Exhaled volatile organic compounds identify patients with colorectal cancer," *British Journal of Surgery*, vol. 100, no. 1, pp. 144-150, 2012, doi: 10.1002/bjs.8942.

[254] D. F. Altomare *et al.*, "Chemical signature of colorectal cancer: case–control study for profiling the breath print," *BJS Open*, vol. 4, no. 6, pp. 1189-1199, 2020, doi: 10.1002/bjs5.50354.

[255] H. Amal *et al.*, "Detection of precancerous gastric lesions and gastric cancer through exhaled breath," (in eng), *Gut,* vol. 65, no. 3, pp. 400-7, Mar 2016, doi: 10.1136/gutjnl-2014-308536.

[256] M. Gruber *et al.*, "Analysis of exhaled breath for diagnosing head and neck squamous cell carcinoma: a feasibility study," *British Journal of Cancer,* vol. 111, no. 4, pp. 790-798, 2014, doi: 10.1038/bjc.2014.361.

[257] L. Guo *et al.*, "Exhaled breath volatile biomarker analysis for thyroid cancer," *Transl Res,* vol. 166, no. 2, pp. 188-95, Aug 2015, doi: 10.1016/j.trsl.2015.01.005.

[258] P. Mochalski *et al.*, "Ex vivoemission of volatile organic compounds from gastric cancer and non-cancerous tissue," *Journal of Breath Research,* vol. 12, no. 4, p. 046005, 2018, doi: 10.1088/1752-7163/aacbfb.

[259] M. Phillips, T. B. Bevers, L. H. Larsen, N. Pappas, and S. Pathak, "Rapid Point-Of-Care Breath Test Predicts Breast Cancer And Abnormal Mammograms in Symptomatic Women," Cold Spring Harbor Laboratory, 2020.

[260] K. Schallschmidt *et al.*, "Comparison of volatile organic compounds from lung cancer patients and healthy controls-challenges and limitations of an observational study," (in eng), *J Breath Res,* vol. 10, no. 4, p. 046007, Oct 12 2016, doi: 10.1088/1752-7155/10/4/046007.

[261] C. Wang *et al.*, "Volatile Organic Metabolites Identify Patients with Breast Cancer, Cyclomastopathy and Mammary Gland Fibroma," *Scientific Reports,* vol. 4, no. 1, p. 5383, 2014/06/20 2014, doi: 10.1038/srep05383.

[262] P. Španěl and D. Smith, "Quantification of volatile metabolites in exhaled breath by selected ion flow tube mass spectrometry, SIFT-MS," *Clinical Mass Spectrometry,* vol. 16, pp. 18-24, 2020/04/01/ 2020, doi: https://doi.org/10.1016/j.clinms.2020.02.001.

[263] M. Koureas, P. Kirgou, G. Amoutzias, C. Hadjichristodoulou, K. Gourgoulianis, and A. Tsakalof, "Target Analysis of Volatile Organic Compounds in Exhaled Breath for Lung Cancer Discrimination from Other Pulmonary Diseases and Healthy Persons," *Metabolites,* vol. 10, no. 8, p. 317, 2020. [Online]. Available: https://www.mdpi.com/2218-1989/10/8/317.

[264] H. Chen *et al.*, "COVID-19 screening using breath-borne volatile organic compounds," *Journal of Breath Research,* 2021, doi: 10.1088/1752-7163/ac2e57.

[265] A. Tiele *et al.*, "Breath-based non-invasive diagnosis of Alzheimer's disease: a pilot study," *Journal of Breath Research,* vol. 14, no. 2, p. 026003, 2020, doi: 10.1088/1752-7163/ab6016.

[266] A. Tiele, A. Wicaksono, J. Kansara, R. P. Arasaradnam, and J. A. Covington, "Breath Analysis Using eNose and Ion Mobility Technology to Diagnose Inflammatory Bowel Disease—A Pilot Study," *Biosensors,* vol. 9, no. 2, p. 55, 2019. [Online]. Available: https://www.mdpi.com/2079-6374/9/2/55.

[267] D. Karakaya, O. Ulucan, and M. Turkan, "Electronic Nose and Its Applications: A Survey," *International Journal of Automation and Computing,* vol. 17, no. 2, pp. 179-209, 2020, doi: 10.1007/s11633-019-1212-9.

[268] C. Hurot, N. Scaramozzino, A. Buhot, and Y. Hou, "Bio-Inspired Strategies for Improving the Selectivity and Sensitivity of Artificial Noses: A Review," *Sensors,* vol. 20, no. 6, p. 1803, 2020, doi: 10.3390/s20061803.

[269] S. W. Brooks, D. R. Moore, E. B. Marzouk, F. R. Glenn, and R. M. Hallock, "Canine Olfaction and Electronic Nose Detection of Volatile Organic Compounds in the Detection of Cancer: A Review," *Cancer Investigation,* vol. 33, no. 9, pp. 411-419, 2015, doi: 10.3109/07357907.2015.1047510.

[270] M. H. M. C. Scheepers, Z. Al-Difaie, L. Brandts, A. Peeters, B. Van Grinsven, and N. D. Bouvy, "Diagnostic Performance of Electronic Noses in Cancer Diagnoses Using Exhaled Breath," *JAMA Network Open,* vol. 5, no. 6, p. e2219372, 2022, doi: 10.1001/jamanetworkopen.2022.19372.

[271] H. Amal *et al.*, "Assessment of ovarian cancer conditions from exhaled breath," *International Journal of Cancer,* vol. 136, no. 6, pp. E614-E622, 2015, doi: 10.1002/ijc.29166.

[272] C. Baldini, L. Billeci, F. Sansone, R. Conte, C. Domenici, and A. Tonacci, "Electronic Nose as a Novel Method for Diagnosing Cancer: A Systematic Review," *Biosensors,* vol. 10, no. 8, p. 84, 2020, doi: 10.3390/bios10080084.

[273] A. B. V, M. Subramoniam, and L. Mathew, "Noninvasive detection of COPD and Lung Cancer through breath analysis using MOS Sensor array based e-nose," (in eng), *Expert Rev Mol Diagn,* vol. 21, no. 11, pp. 1223-1233, Nov 2021, doi: 10.1080/14737159.2021.1971079.

[274] W. H. van Geffen *et al.*, "The electronic nose: emerging biomarkers in lung cancer diagnostics," (in eng), *Breathe (Sheff),* vol. 15, no. 4, pp. e135-e141, Dec 2019, doi: 10.1183/20734735.0309-2019.

[275] A. Filianoti *et al.*, "Volatilome Analysis in Prostate Cancer by Electronic Nose: A Pilot Monocentric Study," (in eng), *Cancers (Basel),* vol. 14, no. 12, Jun 14 2022, doi: 10.3390/cancers14122927.

[276] R. Anzivino *et al.*, "The Role of a Polymer-Based E-Nose in the Detection of Head and Neck Cancer from Exhaled Breath," *Sensors*, vol. 22, no. 17, p. 6485, 2022. [Online]. Available: https://www.mdpi.com/1424-8220/22/17/6485.

[277] F. Rock, N. Barsan, and U. Weimar, "Electronic nose: current status and future trends," *Chem Rev*, vol. 108, no. 2, pp. 705-25, Feb 2008, doi: 10.1021/cr068121q.

[278] O. Mazor and G. Laurent, "Transient Dynamics versus Fixed Points in Odor Representations by Locust Antennal Lobe Projection Neurons," *Neuron*, vol. 48, no. 4, pp. 661-673, 2005, doi: 10.1016/j.neuron.2005.09.032.

[279] D. Saha, K. Leong, N. Katta, and B. Raman, "Multi-unit recording methods to characterize neural activity in the locust (Schistocerca americana) olfactory circuits," (in eng), *J Vis Exp*, no. 71, Jan 25 2013, doi: 10.3791/50139.

[280] C. Pouzat, O. Mazor, and G. Laurent, "Using noise signature to optimize spike-sorting and to assess neuronal classification quality," (in eng), *J Neurosci Methods*, vol. 122, no. 1, pp. 43-57, Dec 31 2002, doi: 10.1016/s0165-0270(02)00276-5.

[281] R. Toosi, M. A. Akhaee, and M.-R. A. Dehaqani, "An automatic spike sorting algorithm based on adaptive spike detection and a mixture of skew-t distributions," *Scientific Reports*, vol. 11, no. 1, p. 13925, 2021/07/06 2021, doi: 10.1038/s41598-021-93088-w.

[282] M. Stopfer, S. Bhagavan, B. H. Smith, and G. Laurent, "Impaired odour discrimination on desynchronization of odour-encoding neural assemblies," *Nature*, vol. 390, no. 6655, pp. 70-74, 1997/11/01 1997, doi: 10.1038/36335.

[283] M. Stopfer and G. Laurent, "Short-term memory in olfactory network dynamics," *Nature*, vol. 402, no. 6762, pp. 664-668, 1999/12/01 1999, doi: 10.1038/45244.

[284] J. Perez-Orive, O. Mazor, G. C. Turner, S. Cassenaer, R. I. Wilson, and G. Laurent, "Oscillations and sparsening of odor representations in the mushroom body," (in eng), *Science*, vol. 297, no. 5580, pp. 359-65, Jul 19 2002, doi: 10.1126/science.1070502.

[285] H. J. Ko and T. H. Park, "Bioelectronic nose and its application to smell visualization," *Journal of Biological Engineering*, vol. 10, no. 1, 2016, doi: 10.1186/s13036-016-0041-4.

[286] P. Pelosi, J. Zhu, and W. Knoll, "From Gas Sensors to Biomimetic Artificial Noses," *Chemosensors*, vol. 6, no. 3, p. 32, 2018, doi: 10.3390/chemosensors6030032.

[287] J. W. Cave, J. K. Wickiser, and A. N. Mitropoulos, "Progress in the development of olfactory-based bioelectronic chemosensors," *Biosens Bioelectron*, vol. 123, pp. 211-222, Jan 1 2019, doi: 10.1016/j.bios.2018.08.063.

[288] Y. Lu *et al.*, "Olfactory biosensor using odorant-binding proteins from honeybee: Ligands of floral odors and pheromones detection by electrochemical impedance," *Sensors and*

Actuators B: Chemical, vol. 193, pp. 420-427, 2014/03/31/ 2014, doi: https://doi.org/10.1016/j.snb.2013.11.045.

[289] T.-Z. Wu, "A piezoelectric biosensor as an olfactory receptor for odour detection: electronic nose," *Biosensors and Bioelectronics*, vol. 14, no. 1, pp. 9-18, 1999/01/01/ 1999, doi: https://doi.org/10.1016/S0956-5663(98)00086-4.

[290] H. Yang *et al.*, "Nanodisc-Based Bioelectronic Nose Using Olfactory Receptor Produced in Escherichia coli for the Assessment of the Death-Associated Odor Cadaverine," *ACS Nano*, vol. 11, no. 12, pp. 11847-11855, 2017/12/26 2017, doi: 10.1021/acsnano.7b04992.

[291] H. J. Jin *et al.*, "Nanovesicle-based bioelectronic nose platform mimicking human olfactory signal transduction," *Biosensors and Bioelectronics*, vol. 35, no. 1, pp. 335-341, 2012/05/15/ 2012, doi: https://doi.org/10.1016/j.bios.2012.03.012.

[292] J. H. Lim, J. Park, E. H. Oh, H. J. Ko, S. Hong, and T. H. Park, "Nanovesicle-Based Bioelectronic Nose for the Diagnosis of Lung Cancer from Human Blood," *Advanced Healthcare Materials*, vol. 3, no. 3, pp. 360-366, 2014, doi: https://doi.org/10.1002/adhm.201300174.

[293] J. Vidic *et al.*, "Gold Surface Functionalization and Patterning for Specific Immobilization of Olfactory Receptors Carried by Nanosomes," *Analytical Chemistry*, vol. 79, no. 9, pp. 3280-3290, 2007/05/01 2007, doi: 10.1021/ac061774m.

[294] J. H. Ahn *et al.*, "Screening of target-specific olfactory receptor and development of olfactory biosensor for the assessment of fungal contamination in grain," *Sensors and Actuators B: Chemical*, vol. 210, pp. 9-16, 2015/04/01/ 2015, doi: https://doi.org/10.1016/j.snb.2014.12.060.

[295] S. Sankaran, S. Panigrahi, and S. Mallik, "Odorant binding protein based biomimetic sensors for detection of alcohols associated with Salmonella contamination in packaged beef," *Biosensors and Bioelectronics*, vol. 26, no. 7, pp. 3103-3109, 2011/03/15/ 2011, doi: https://doi.org/10.1016/j.bios.2010.07.122.

[296] M. Larisika *et al.*, "Electronic Olfactory Sensor Based on A. mellifera Odorant-Binding Protein 14 on a Reduced Graphene Oxide Field-Effect Transistor," *Angewandte Chemie International Edition*, vol. 54, no. 45, pp. 13245-13248, 2015, doi: https://doi.org/10.1002/anie.201505712.

[297] N. Misawa *et al.*, "Construction of a Biohybrid Odorant Sensor Using Biological Olfactory Receptors Embedded into Bilayer Lipid Membrane on a Chip," *ACS Sens*, vol. 4, no. 3, pp. 711-716, Mar 22 2019, doi: 10.1021/acssensors.8b01615.

[298] A. Calabrese *et al.*, "An Impedimetric Biosensor for Detection of Volatile Organic Compounds in Food," *Biosensors*, vol. 13, no. 3, p. 341, 2023. [Online]. Available: https://www.mdpi.com/2079-6374/13/3/341.

[299] A. McWilliams, P. Beigi, A. Srinidhi, S. Lam, and C. E. MacAulay, "Sex and Smoking Status Effects on the Early Detection of Early Lung Cancer in High-Risk Smokers Using an Electronic Nose," (in eng), *IEEE Trans Biomed Eng*, vol. 62, no. 8, pp. 2044-54, Aug 2015, doi: 10.1109/tbme.2015.2409092.

[300] Y. Li, X. Wei, Y. Zhou, J. Wang, and R. You, "Research progress of electronic nose technology in exhaled breath disease analysis," *Microsystems & Nanoengineering*, vol. 9, no. 1, p. 129, 2023/10/11 2023, doi: 10.1038/s41378-023-00594-0.

[301] J. A. Cheema, C. Carraher, N. O. V. Plank, J. Travas-Sejdic, and A. Kralicek, "Insect odorant receptor-based biosensors: Current status and prospects," *Biotechnol Adv*, vol. 53, p. 107840, Dec 2021, doi: 10.1016/j.biotechadv.2021.107840.

[302] N. S. Aghili, M. Rasekh, H. Karami, O. Edriss, A. D. Wilson, and J. Ramos, "Aromatic Fingerprints: VOC Analysis with E-Nose and GC-MS for Rapid Detection of Adulteration in Sesame Oil," *Sensors*, vol. 23, no. 14, p. 6294, 2023. [Online]. Available: https://www.mdpi.com/1424-8220/23/14/6294.

[303] A. D. Wilson, "Application of Electronic-Nose Technologies and VOC-Biomarkers for the Noninvasive Early Diagnosis of Gastrointestinal Diseases," *Sensors*, vol. 18, no. 8, p. 2613, 2018. [Online]. Available: https://www.mdpi.com/1424-8220/18/8/2613.

[304] C. Korkmaz and A. Zamani, "Screening for Lung Cancer," in *Airway Diseases*, C. Cingi, A. Yorgancıoğlu, N. Bayar Muluk, and A. A. Cruz Eds. Cham: Springer International Publishing, 2023, pp. 1451-1476.

[305] L. Zhao, W. Shi, Y. Gong, X. Liu, W. Li, and Y. Jia, "33.9 A Miniature Neural Interface Implant with a 95% Charging Efficiency Optical Stimulator and an 81.9 dB SNDR ΔΣM-Based Recording Frontend," in *2024 IEEE International Solid-State Circuits Conference (ISSCC)*, 2024, vol. 67: IEEE, pp. 558-560.